Robust Quantum Metrology

Paul Alexander Knott

Department of Physics and Astronomy

University of Leeds

Submitted in accordance with the requirements for the degree of

Doctor of Philosophy

March 2015

I confirm that the work submitted in this thesis is my own, except where work which has formed part of jointly authored publications has been included. The contribution of myself and the other authors to this work has been explicitly indicated below. I confirm that appropriate credit has been given within the thesis where reference has been made to the work of others.

Publications

1. *Detecting measurement-induced relative-position localization*, P A Knott, J Sindt, J A Dunningham, Journal of Physics B 46 (9), 095501 (2013).

Chapter 2 is based on results from this paper. This work was completed in collaboration with Julien Sindt and Dr Jacob Dunningham. The simulations in this section used a Matlab code which was originally developed by Julien Sindt, but was subsequently improved upon and altered by myself in order to produce the results as shown here.

2. *Precise Phase Measurements using an Entangled Coherent State*, P A Knott, J A Dunningham, arXiv:1401.3969, Conference proceedings for Photopics 2014.

Section 3.4 and chapter 4 are based on results from this paper. This work was completed with Dr Jacob Dunningham. I was the main contributor to this chapter.

3. *Attaining subclassical metrology in lossy systems with entangled coherent states*, P A Knott, W J Munro, J A Dunningham, Physical Review A 89 (5), 053812 (2014).

Chapter 4 is based on results from this paper. This work was completed in collaboration with Dr William Munro and Dr Jacob Dunningham. I was the main contributor to this chapter.

4. *Effect of multimode entanglement on lossy optical quantum metrology*, P A Knott, T J Proctor, K Nemoto, J A Dunningham, W J Munro, Physical Review A 90 (3), 033846 (2014).

Chapter 5 is based on results from this paper. This work was completed in collaboration with Tim Proctor, Dr William Munro and Dr Jacob Dunningham. The quantum Fisher information analytical calculations in this section were completed by myself and Tim Proctor. I was the main contributor for the simulations.

5. *Robust entanglement-based magnetic field sensor beyond the standard quantum limit*, T Tanaka*, P A Knott*, Y Matsuzaki*, S Dooley, H Yamaguchi, W J Munro, S Saito, submitted to Physical Review Letters, arXiv preprint arXiv:1412.3887. *These authors equally contributed to this paper.

Chapter 6 is based on results from this paper. This work was completed in collaboration with Dr Yuichiro Matsuzaki, Dr Shane Dooley and Dr William Munro. I was the main contributor to the work in this chapter.

This thesis is dedicated to my family.

Acknowledgements

My thanks go first and foremost to my supervisor Jacob Dunningham. He has always been a great source of inspiration and knowledge, and has provided help, support and many fantastic ideas throughout my PhD. I am also extremely thankful to Bill Munro, my PhD internship supervisor, who provided me with a great experience in NTT BRL, and has likewise been of huge help, inspiration, and guidance.

I would also like to thank Yuichiro Matsuzaki for all his help and advice whilst at NTT, and all the quantum information PhD students and Postdocs at Leeds. These include, but are certainly not limited to: Tim Proctor, Adam Stokes, Shane Dooley, Veiko Palge, Robert Bennett, James de Lisle, Konstantinos Meichanetzidis and Suva De. They have been a tremendous source of help, advice, knowledge, entertainment and annoyance, particularly in our many board sessions and debates. I am also greatly indebted to the academics in our group who have provided invaluable support: thanks to Almut Beige, Viv Kendon, Tim Spiller, and Jiannis Pachos. Last but not least I would like to acknowledge the two things that without which my PhD would have been impossible: tea and Beethoven.

Abstract

In optical interferometry path-entangled states such as NOON states have shown to give quantum-enhanced precision measurements, but these states are notoriously fragile to particle losses, which typically collapse the quantum state and destroy the phase information. A class of inherently robust states that show the potential for great improvements over the alternatives are the entangled coherent states (ECSs). We show that these states allow substantial improvements over unentangled 'classical' states and highly-entangled NOON states for a wide range of loss values. We then describe a measurement scheme that can be used to measure these states with a precision close to the theoretical bound given by the quantum Fisher information.

We then look at the quantum mechanisms that lead to precise measurements. In optical interferometry multi-mode entanglement is often assumed to be the driving force behind quantum enhanced measurements. Recent work has shown this assumption to be false, and here we show that when photon losses occur multi-mode entanglement is actually detrimental to obtaining quantum enhanced measurements. We specifically apply this idea to a superposition of coherent states, demonstrating that these states show a robustness to loss that allows them to significantly outperform their competitors in realistic systems. A practically viable measurement scheme is then presented that allows measurements close to the theoretical bound, even with loss.

In this thesis we also consider superpositions of spin coherent states and their application to quantum metrology. Compared to optical states, spin systems have a distinctly different process of decoherence

known as non-Markovian dephasing, which has shown to give greatly improved robustness to loss. We see that spin cat states give an enhanced *scaling* over the shot noise limit, even with dephasing, whilst being realisable with current technology.

Abbreviations

SNL	Shot Noise Limit
GW	Gravitational Wave
QBS	Quantum Beam Splitter
ECS	Entangled Coherent State
CS	Coherent State
QFI	Quantum Fisher Information
FI	Fisher Information
CRB	Cramér-Rao bound
QCRB	Quantum Cramér-Rao bound
POVM	Positive Operator-Valued Measurement
SP	Single Particle
BS	Beam Splitter
EECS	Even Entangled Coherent State
UCS	Unbalanced Cat State
PNRD	Photon-Number Resolving Detector
JCH	Jaynes-Cummings Hamiltonian
NV	Nitrogen-vacancy

Contents

List of Figures

Chapter 1

Introduction

1.1 Metrology: the science of measurement

"To measure is to know" - Lord Kelvin

At the heart of scientific endeavor is the act of measurement, as is clear from the world's great scientific discoveries: from the refutation of the ether by Michelson & Morley (1887), to the surprise discovery of the cosmic microwave background radiation by Penzias & Wilson (1965) and the recent Higgs-like particle discovery at CERN (Aad *et al.*, 2012; Chatrchyan *et al.*, 2012). The attribution of major scientific breakthroughs to measurements is clear in these experimental cases, but even the great theoretical achievements - from Einstein's special relativity (Einstein *et al.*, 1905) to the prediction of the Higgs boson (Englert & Brout, 1964) - are nothing without having been motivated, or confirmed, by experiments, which rely on measurements for their results. For these reasons, the progression of science, and in particular physics, is intricately linked with the progression of the measurements that we can make. Furthermore, the precision with which we can measure determines the depths to which we can delve, and so the measurement devices we use have to become increasingly precise to facilitate new discoveries.

If precision is so important, then what are its bounds? If we take the simple

example of counting the number of raindrops that fall on a tin roof per second[1], then the precision with which this can be measured scales with the number of raindrops N as $1/\sqrt{N}$. This probabilistic uncertainty is due to the Gaussian distribution of the falling raindrops: the number of drops per second fluctuates about the average, with the precision given by the standard deviation of these fluctuations. Whilst counting raindrops might be fun, knowing the precision of this measurement isn't often particularly important. If we take the Michelson-Morley experiment however (Michelson & Morley, 1887), then knowing the precision is paramount, but due to the Gaussian distribution of the light used in their interferometry experiment (which will be described in due course), the precision takes the same form: we can measure our movement through the ether (or not) to a precision of $1/\sqrt{N}$, where N is the number of photons used. This bound is known as the shot noise limit (SNL), and will be discussed in detail in this thesis.

The SNL suggests that to increase the precision of our measurements we simply have to increase the number of resources, e.g. photons, that we use. This may be possible in many examples, but there are a number of cases where this strategy is not possible. For example, imagine that you wish to probe a living cell, or more specifically you wish to track the path of a lipid granule as it diffuses through the cytoplasm of a yeast cell (Taylor *et al.*, 2013). In this case if you increase the power of your probe, you damage the sample, and so, somewhat ironically, that which you wish to measure has been destroyed by your measurement. It is sometimes possible to keep the power constant but run the experiment over a longer time period. But in this case this is useless, as the lipid granule will pass by before you can track it.

Another example is in the huge international efforts to directly measure gravitational waves (GWs) (Aasi *et al.*, 2013). This example again uses light, which in this case is used to measure the stretching and squeezing of spacetime as a GW passes by. The problem here is not destroying the phenomenon you wish to measure (a photon cannot bend spacetime, at least not at terrestrial energy scales); the problem is the absurdly small length changes that the GW produces, which are in the order of 10^{-22}m. The laser power needed here is in the 100W

[1]This example of rain drops was found in Wolfgramm (2011).

range, and this is enough to distort the measuring apparatus itself. Is there another option, other than increasing the power of the lasers? The solution to this problem lies in the hidden powers of quantum mechanics.

1.2 The power of quantum mechanics

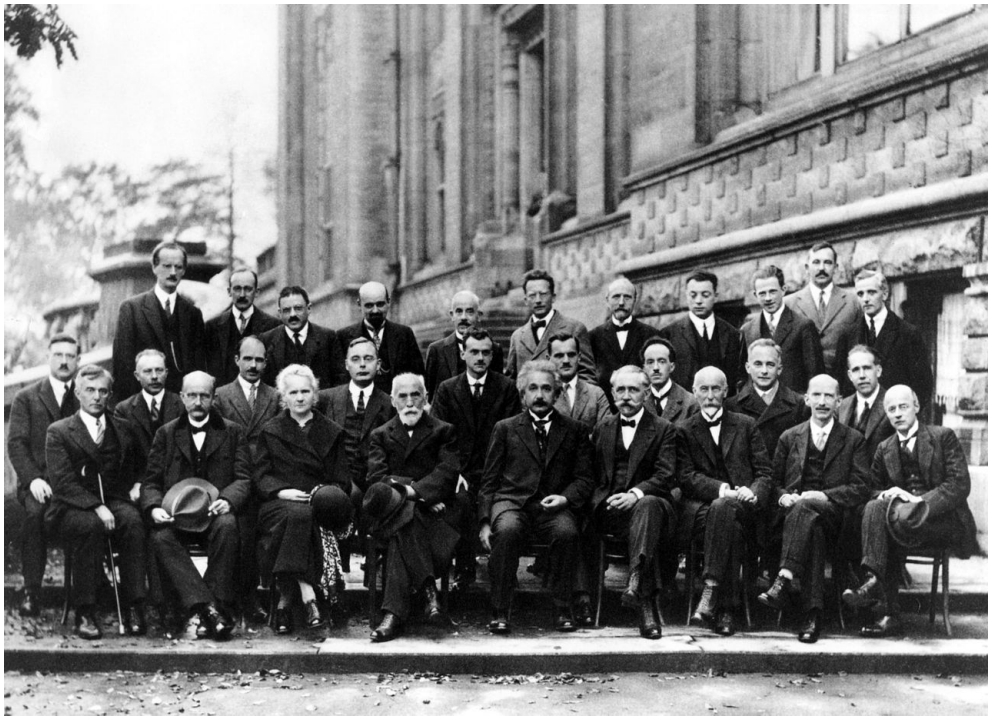

Figure 1.1: The Solvay conference in 1927, which was attended by most of the founders of quantum mechanics (public domain image).

The spectacularly confusing and remarkably well proven theory of quantum mechanics was developed in the first half of the 20th century by a host of great thinkers (many of whom attended the Solvay conference in 1927 as shown in Fig. 1.1). By describing the world in terms of discrete 'quanta', this remarkable theory was able to solve deep problems in physics, such as the photoelectric effect (Einstein, 1905). But quantum mechanics proved to be far more obscure than anyone had expected, which justifies Richard Feynman famously saying "I think I can safely say that nobody understands quantum mechanics" (Feynman,

1967). The said obscurities are plentiful, including wave-particle duality, quantum superposition, the collapse of the wavefunction, and most importantly for our purposes, quantum entanglement.

Quantum entanglement is one of the cornerstones of quantum mechanics, and can lead to a multitude of effects unfathomable to a pre-quantum era physicist. It is at the heart of the some of the most controversial and exciting physics of the 20th century, such as the EPR paradox (Bell, 1964; Einstein *et al.*, 1935) which investigates the strange nonlocality within quantum mechanics, and Schrödinger's famous alive and dead cat (Schrödinger, 1980).

Entanglement is a property of correlations between two or more quantum subsystems. So what does it mean for a number of subsystems to be entangled with one another? This is a surprisingly difficult question to answer: a far easier question is what it means for subsystems to not be entangled (Barnett, 2009). For simplicity we will deal with just a pair of quantum states, $|\lambda\rangle_a$ and $|\gamma_b\rangle$, where the subscripts denote subsystems a and b. An unentangled composite state of these two can be written as the tensor product

$$|\Psi\rangle = |\lambda\rangle_a \otimes |\gamma\rangle_b \tag{1.1}$$

If the state of the composite system **cannot** be written as a tensor product in this way then it is entangled[1]! For a simple example, we can look at the Bell state

$$|\Phi^+\rangle = \frac{1}{\sqrt{2}} \left(|0\rangle_a \otimes |0\rangle_b + |1\rangle_a \otimes |1\rangle_b\right) \tag{1.2}$$

It is easy to see that this state cannot be written as a tensor product of states a and b and therefore this is an entangled state. This state can be thought of as a pair of qubits (two level quantum systems), with qubit a belonging to Alice and qubit b to Bob. Alice and Bob can take their states as far apart as they like, to either end of the galaxy if they wish, and the state will still be given by equation 1.2. What would happen if Alice measured her state? A measurement would cause

[1]We can extend this to mixed states: a state ρ is separable (i.e. not entangled) if it can be written as $\rho = \sum_i p_i \rho_i^A \rho_i^B$, where ρ_i^A and ρ_i^B are states on subsystems A and B, and p_i are positive valued probabilities (Laloë, 2012).

the state to collapse into $|0\rangle_a \otimes |0\rangle_b$ **or** $|1\rangle_a \otimes |1\rangle_b$, and so if Alice's measurement recorded 0, then any subsequent measurement by Bob will necessarily give the value 0. This is the case even if Alice and Bob have space-like separation and this spooky action at a distance has caused much controversy and intrigue over the years (Einstein *et al.*, 1935) [1].

The remarkable properties of entangled states can be exploited in a range of ways, many of which are being scrupulously investigated in the field of quantum information science in such topics as quantum key distribution, quantum teleportation, and quantum computation. But our main use of entanglement will be in solving the problem explained above, namely in beating the SNL in metrology to achieve high precision measurements that are unattainable using classical physics alone. The field of quantum metrology uses entanglement to obtain a precision that scales with the number of particles as the Heisenberg limit, $1/N$, a $\sqrt{N}$ improvement on the SNL. We can thus increase our precision without increasing the number of particles we use, and this does indeed solve the above problem and allow us to probe GWs (Aasi *et al.*, 2013), biological samples (Taylor *et al.*, 2013), and a whole range of other systems (Carlton *et al.*, 2010; Eckert *et al.*, 2008; Pototschnig *et al.*, 2011; Tey *et al.*, 2008; Wolfgramm *et al.*, 2013), without disastrous effects being inflicted upon the sample or equipment.

Despite the recent uses of quantum metrology to enhance measurements in Aasi *et al.* (2013) and Taylor *et al.* (2013), attaining sub-classical measurements is still an extremely difficult task. This is due to the fragile nature of quantum systems, which decohere upon interacting with their surroundings, suppressing the quantum effects which we wish to exploit. In this thesis we will explore a number of states that show the potential for greater robustness to decoherence, and we show how the classical limits can be breached and improved upon in a range of realistic scenarios. We will explore the classical and quantum limits to precision measurements, and even present a new class of states that allow the previously held quantum 'limits' to be improved upon in optical, as well as atomic, systems.

[1] Strictly speaking, it can only be determined that the correlations are quantum mechanical by measuring the subsystems in different bases. If the measurement results violate Bell's inequality (Bell, 1964), then the correlations are quantum mechanical.

1.3 Thesis overview

This thesis is structured as follows. We begin in Chapter 2 with an aside from quantum metrology in which we describe a mechanism where photon scattering causes the relative localisation of particles. We show how this mechanism can be tested experimentally, and then extend the formalism to three dimensions.

Chapter 3 then introduces the main topic of this thesis: optical quantum metrology. The basic Mach-Zehnder interferometer is introduced, and we show how quantum states can be used to surpass the classical limit in precision phase measurements. We then introduce an intrinsically robust class of states: the entangled coherent states.

In chapter 4 we study the effects of loss on entangled coherent states, and show how they have the potential for robust sub-classical measurements. We then describe a measurement scheme that can be used to measure a phase shift using an entangled coherent state with a precision close to the theoretical bound given by the quantum Fisher information.

Chapter 5 begins by asking the question of whether multi-mode entanglement in an interferometer is necessary to make quantum-enhanced measurements. We introduce previous work showing that multi-mode entanglement is not necessary, then we elaborate on this by demonstrating that, when loss is included, in a number of well known examples multi-mode entanglement leads to more fragile states. We introduce a number of single-mode superposition states that surpass their multi-mode-entangled alternatives.

In chapter 6 we move away from optical quantum metrology to look at magnetic field sensing with spin systems. We show that, unlike in optical systems, the decoherence mechanism in spin systems still allows precision measurements that beat the classical limits *in scaling*. We present a practical scheme of creating superpositions of spin coherent states that can measure a magnetic field to a quantum-enhanced precision, and we describe a measurement scheme that can be used to read out the phase information that utilises present day or near future technology.

Chapter 2

Relative position localisation caused by entanglement

We begin this thesis with a digression into a subject quite removed from the technology driven area of quantum metrology. However, this will not be a fruitless digression, as both quantum metrology and the relative position localisation scheme we describe here share a number of features and jointly utilise a number of research techniques. Therefore, this section, as well as being interesting in itself, will be used as a pedagogical chapter to help introduce the ideas of quantum superposition, state collapse, decoherence, and Bayes' theorem.

Section 2.2 of this chapter uses the work of Rau *et al.* (2003), and the rest of the chapter is work done by the author in collaboration with Julien Sindt. This work has been published in the paper Knott *et al.* (2013).

2.1 The quantum to classical transition

The apparent inconsistencies between the quantum and classical worlds have long been a stumbling point in the construction of quantum mechanics as a complete theory. Bohr's view of drawing a strict line between the two introduces unsolvable problems of where exactly the border should be, while the many worlds interpretation only postpones the key questions (Zurek, 2002). The theory of decoherence (Mazzola *et al.*, 2010; Zurek, 1991, 2002), described as "environment-induced, dynamical destruction of quantum coherence" (Breuer & Petruccione, 2002), has

come a long way in explaining why macroscopic objects do not in general have quantum properties. The basic idea of decoherence begins with a quantum system which interacts with its surroundings ('the environment'), allowing us to treat the system and environment with quantum physics. We then trace over the environmental modes (this will be described later), which results in information being lost to the environment and the loss of quantum correlations. However, decoherence is notoriously difficult to apply because of the complex nature of the coupling between system and environment, and furthermore it has this undesirable feature of requiring some quantum correlations to be discarded (Knott *et al.*, 2013; Rau *et al.*, 2003).

An additional interpretation to decoherence was put forward in Rau *et al.* (2003) which involves a very simple mechanism that does not require the abandonment of all quantum effects. Indeed, in this scheme the classical property of localisation can be explained in terms of entanglement. This effectively destroys the quantum-classical boundary itself as it proposes that even classical objects are entangled, be it with a special type of robust entanglement sometimes called 'fluffy-bunny' entanglement (Dunningham *et al.*, 2005; Wiseman *et al.*, 2004). The interpretation also emphasises the importance of *relative* position, as in the measurement-induced localisation that we explain below, no *absolute* localisation takes place.

2.2 Review of one dimensional localisation

We will now review the scheme in Rau *et al.* (2003) for measurement-induced relative-position localisation in one dimension through entanglement, shown schematically in Fig. 2.1. Two distinguishable massive non-interacting particles are delocalised over some region d in the x-direction, and are tightly confined in the y and z directions. The particles are illuminated with plane-wave light of wavelength λ, incident along the y-axis. The scattered light is detected at an angle θ on a screen located at a distance L from the particles (where $L \gg d$).

For consistency with the 3D case discussed below, we will use wavefunction formalism in our analysis rather than the Dirac notation used in Rau *et al.* (2003).

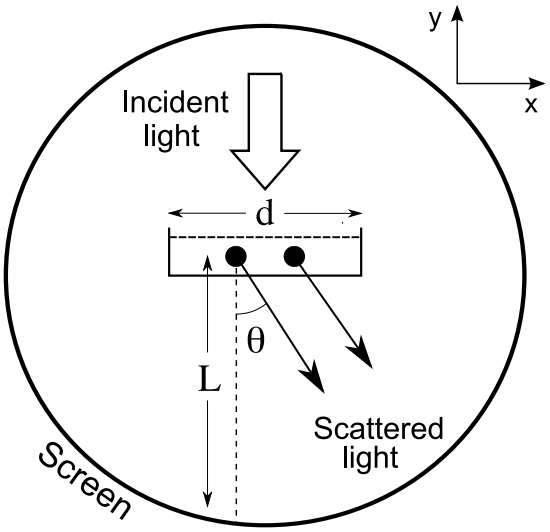

Figure 2.1: A schematic showing the proposed experiment in which two massive particles are delocalised over some region d and are illuminated by plane wave incident light. The scattered light is detected at an angle θ on a screen located at a distance L away from the particles. For clarity, the diagram is not to scale: we consider the case where $L \gg d$.

The initial wave function of the particles is $c(x)$ where x represents the *relative* position of the two particles. The centre-of-mass coordinate of the particles can be neglected as it remains unentangled from the relative position coordinate throughout the scattering process. When a photon of wavelength λ scatters off a particle into angle θ, the particle receives a momentum kick in the x-direction of $\Delta p = h \sin\theta/\lambda$, where h is Planck's constant. In relative momentum space the particles therefore receive a kick of $\pm h \sin\theta/\lambda$ depending on which particle the photon scatters from and, since we do not know (because $L \gg d$), we get a superposition of both possibilities. This allows us to write the overall wavefunction of the system after a photon has scattered as a superposition of plane waves

$$\begin{aligned} \Psi(x,\theta) &\propto e^{\frac{2\pi i \Delta p x}{h}} + e^{\frac{-2\pi i \Delta p x}{h}} \\ &\propto \cos(\frac{2\pi x}{\lambda}\sin\theta). \end{aligned} \tag{2.1}$$

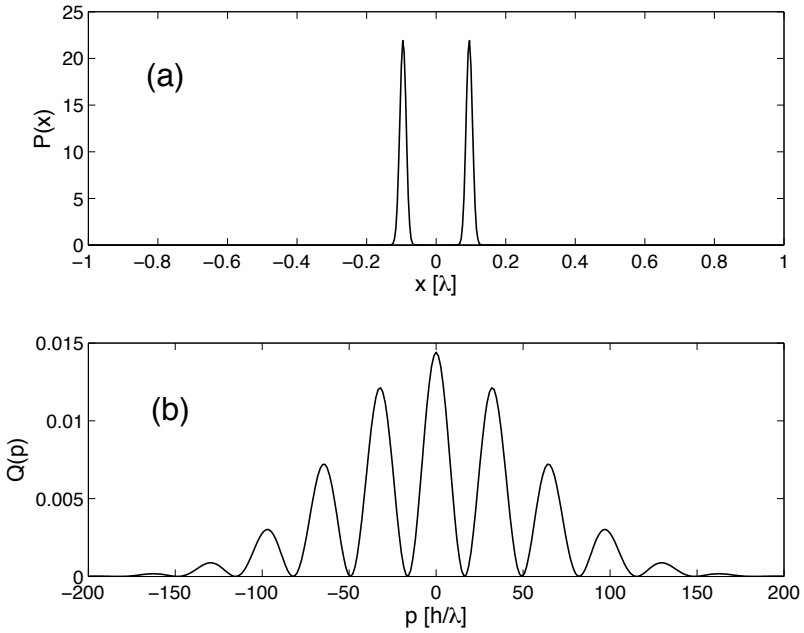

Figure 2.2: The case of light scattering causing relative localisation. (a) Probability density, $P(x)$, for the relative position of the particles after the scattering and detection of 150 photons. The position is given in units of the wavelength, λ, of the scattered light. (b) Probability density, $Q(p)$ for the corresponding relative momentum of the particles.

The complete normalised state is given by

$$\Psi(x,\theta) = \begin{cases} \frac{1}{\sqrt{2\pi}} c(x) \cos\left(\frac{2\pi x}{\lambda}\sin\theta\right) & \text{if } \theta \neq 0 \\ \\ c(x)A(x) & \text{if } \theta = 0 \end{cases} \tag{2.2}$$

The term defined as

$$A(x) = \left[\frac{1}{2\pi}\int_0^{2\pi} \sin^2\left(\frac{2\pi x}{\lambda}\sin\theta'\right)\, d\theta'\right]^{1/2}, \tag{2.3}$$

represents a nonscattering event that leaves the photon in the undeflected state (it is easier to see how A is found by considering the probabilities below).

The probability density for detecting a scattered photon at angle $\theta \neq 0$, and

the probability density of detecting a nonscattered photon, P_{NS}, are given by

$$P_S(\theta) = \int_{-d}^{d} |\Psi(x, \theta \neq 0)|^2 dx = \frac{1}{2\pi} \int_{-d}^{d} |c(x)|^2 \cos^2 \left(\frac{2\pi x}{\lambda} \sin\theta \right) dx \qquad (2.4)$$

$$P_{NS} = \int_{-d}^{d} |c(x)|^2 A^2 \, dx = 1 - \int_{0}^{2\pi} P_s(\theta) \, d\theta.$$

To model a scattering event we generate a random number to see whether the photon is scattered and, if so, at what angle. If it is not scattered the (unnormalised) new state is $c(x)A(x)$ and if it is scattered at an angle θ_1, the (unnormalised) new state is given by

$$\psi(x, \theta_1) = c(x) \cos \left(\frac{2\pi x}{\lambda} \sin\theta_1 \right).$$

We then normalise the state and repeat for the next photon.

We would now like to simulate the localisation procedure proposed in Rau *et al.* (2003). We choose to start our simulations with a flat distribution, $c(x) = 1/\sqrt{2d}$, i.e. a completely delocalised state over region d. Fig. 2.2 shows the probability distribution, $P(x)$, for the relative position of the two particles for a typical run after 150 photons have been detected. We can see that the initially completely flat distribution has evolved into twin peaks that are symmetric about the origin, showing relative position localisation of the two particles.

We have found that the rate at which the particles localise can be illustrated by looking at the variance of each probability density peak, given by

$$\sigma^2(x) = \int_{-d}^{d} |c(x)|^2 x^2 \, dx - \left(\int_{-d}^{d} |c(x)|^2 x \, dx \right)^2.$$

Fig. 2.3 shows how the variance is related to the number of photons fired at the particles by $variance \propto (number\,of\,particles)^{-1}$.

2.3 The proposed experiment to test the localisation

We have reviewed a scheme (Rau *et al.*, 2003) in which photon scattering causes localisation of particles in one dimension. We will now propose a method to experimentally confirm that the scattering process has caused the localisation.

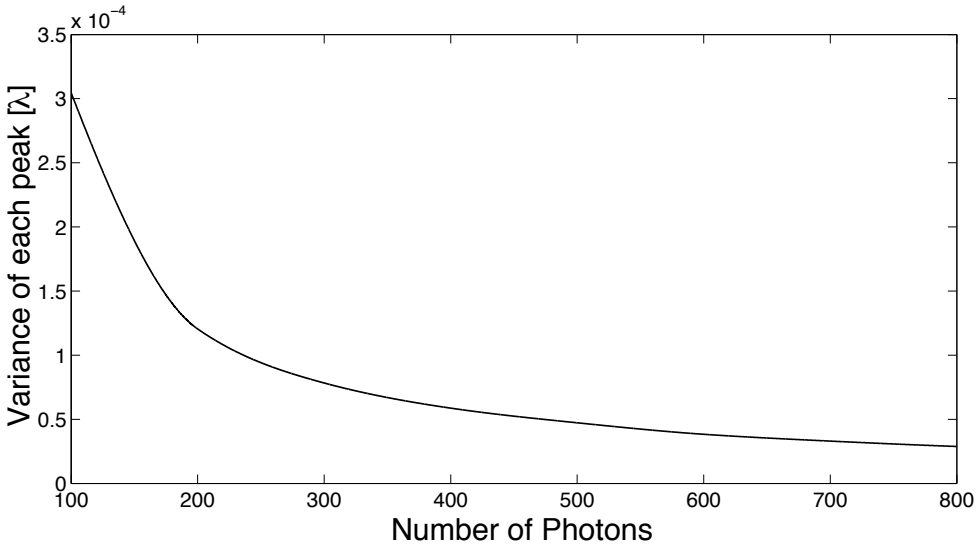

Figure 2.3: This figure shows how the variance of each probability density peak decreases as the number of photons fired at the particles increases. The general shape of the graph is $variance \propto (number\,of\,particles)^{-1}$.

Our wish is to confirm that the final state shown in Fig. 2.2 was indeed caused by the scattering process. If the state was already localised to begin with, instead of seeing two peaks in the probability distribution we would only see one (Fig. 2.4(a)). While it is easy for us to distinguish between the two cases shown in Fig. 2.2 and Fig. 2.4(a), it is not straightforward for an experimentalist to distinguish between them as measuring the angles at which the photons scatter cannot tell the two distributions apart.

To distinguish between them, we must look at the momentum of the particles. The relative momentum distributions corresponding to the relative position distributions in Figs 2.2(a) and 2.4(a) are shown as the solid lines in Figs 2.2(b) and 2.4(b) respectively. For ease of comparison, the result from Fig. 2.2(b) is superimposed on Fig. 2.4(b) as a dashed line. We see that the two distributions have the same envelope, but the case where localisation is induced has interference fringes. For particles that are *a priori* perfectly localised, the distribution in Fig. 2.4(a) would be a delta function and the momentum distribution would be completely flat. We have chosen the relative position distribution shown because

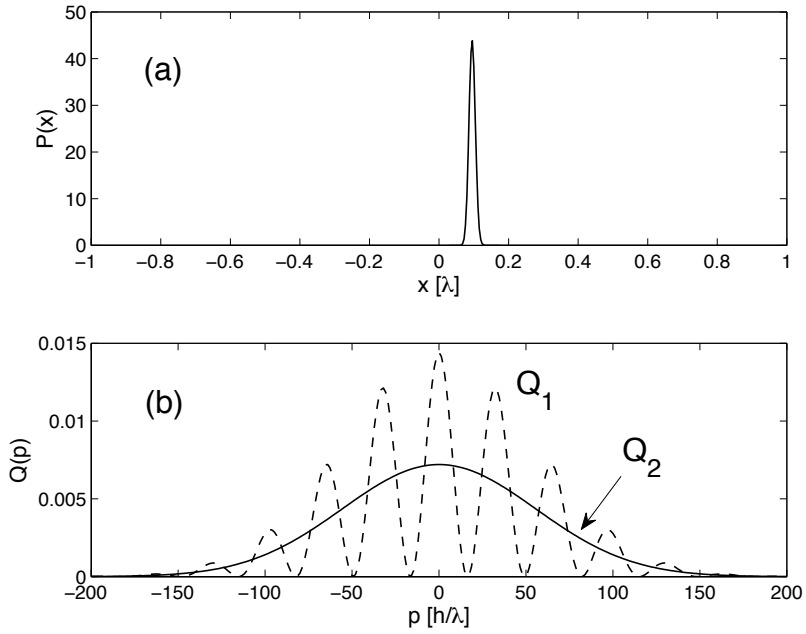

Figure 2.4: (a) The same as in Figure 2.2 but with the particles initially localised before the photons are scattered: there is now only one peak in the relative position probability density. (b) The solid line (labeled Q_2) shows the corresponding relative momentum probability density for the initially *localised* particles in (a). This is compared with the relative momentum probability density for the initially *delocalised* particles in Figure 2.2, which is shown as a dashed line (labeled Q_1).

it is an upper limit to the width possible based on the photons detected. In other words, it is the 'hardest' case to distinguish from that shown in Fig. 2.2(a). We want to demonstrate that our technique works even in this worst-case scenario.

The measurement scheme is then quite straightforward. After scattering the photons from the particles, we want to distinguish the two relative momentum distributions shown in Fig. 2.4(b). To do this, we switch off any trapping potential and allow the particles to move freely. By detecting their positions in the x-direction after some time of flight, we can infer the x-components of their momenta and hence the relative momentum of the particles in that direction. By repeating the whole process from the beginning many times, we should be able to build up a probability distribution and so distinguish the two cases. However, the stochastic nature of the process means that the particles localise to a different relative position on each run and so the relative momentum fringes are different each time. If we were to just naïvely add the results from each run, the fringes would wash out. Instead we can use Bayesian analysis, which stems from Bayes' theorem, to distinguish the two scenarios[1]. The theorem is stated as

$$P(A|B) = \frac{P(B|A)P(A)}{P(B)}, \tag{2.5}$$

where $P(A|B)$ is the conditional probability of event A occurring *given* that B has occurred, and $P(A)$ ($P(B)$) is the probability of A (B) occurring. This formula therefore allows you to update your knowledge about the chances of an event A occurring, given that you know that event B has occurred - this is known as Bayesian analysis.

We will now describe how Bayes' theorem can be used in our experiment in order to distinguish the two relative momentum distributions shown in Fig. 2.4(b). Suppose on a particular run we detected scattered photons on the screen that lead us to conclude that the relative momentum distribution was either $Q_1(p)$ or $Q_2(p)$

[1]Bayes' theorem was discovered by the 18th century English Presbyterian minister Thomas Bayes (McGrayne, 2011; Routledge, 2013), but lay hidden to the scientific community before being re-discovered and published by another Presbyterian minister, Richard Price, in 1763 (Bayes & Price, 1763). Despite its simplicity, Bayes theorem is now used in fields as diverse as artificial intelligence, insurance calculations, code breaking, gambling, and of course in quantum information (Knott *et al.*, 2013; McGrayne, 2011; Pezze & Smerzi, 2008).

depending on whether or not the scattering process induced relative localisation (see Fig. 2.4(b)). To begin with, we do not know whether the particles are localised or not so we take our prior probability of them initially being localised, P_l, to be the same as the prior probability of them not initially being localised, P_{nl}, i.e. $P_l = P_{nl} = 0.5$. Now suppose, upon releasing the particles, we measure their relative momentum to be p_1. This gives us some information about which scenario is more likely. In particular, Bayes' theorem tells us that the updated probabilities are $P_{nl} \propto Q_1(p_1) \times 0.5$ and $P_l \propto Q_2(p_1) \times 0.5$. Normalising, we get

$$P_{nl} = \frac{Q_1(p_1)}{Q_1(p_1) + Q_2(p_1)} \tag{2.6}$$

and $P_l = 1 - P_{nl}$. We can then iterate this process by using these updated probabilities as the prior probabilities in the next step. By repeating many times we increasingly refine our knowledge of which process is occurring.

A sample simulation is shown in Fig. 2.5 for the case that the particles do not initially have a well-defined relative position. We see that initially $P_{nl} = P_l = 0.5$ and that as more and more runs are performed our knowledge of what process is occurring is refined. The probabilities initially jump around for a while before settling down after about 25 runs. The information in this figure is what would be directly accessible to experimentalists and so, in this case, they would be quite certain after about 25 runs that they had observed measurement-induced relative-position localisation.

Of course, every experiment would be different due to the stochastic nature of the photon scattering events and the momentum measurements of the particles. So it would be useful to know how many runs on average are likely to be required to achieve a certain degree of confidence. In Fig. 2.6 we have averaged the results over 300 simulated experiments. We see that the curves are now quite smooth and that after 20 runs we would expect, on average, to be about 95% confident that measurement-induced relative-position localisation is occurring.

It is instructive to investigate the precision requirements of the experiment we are proposing. Specifically we look at the smallest momenta that can be resolved by the apparatus, δp, and compare this with actual experiment simulations. Fig. 2.7 shows us that in order to be 90% sure that the state was initially

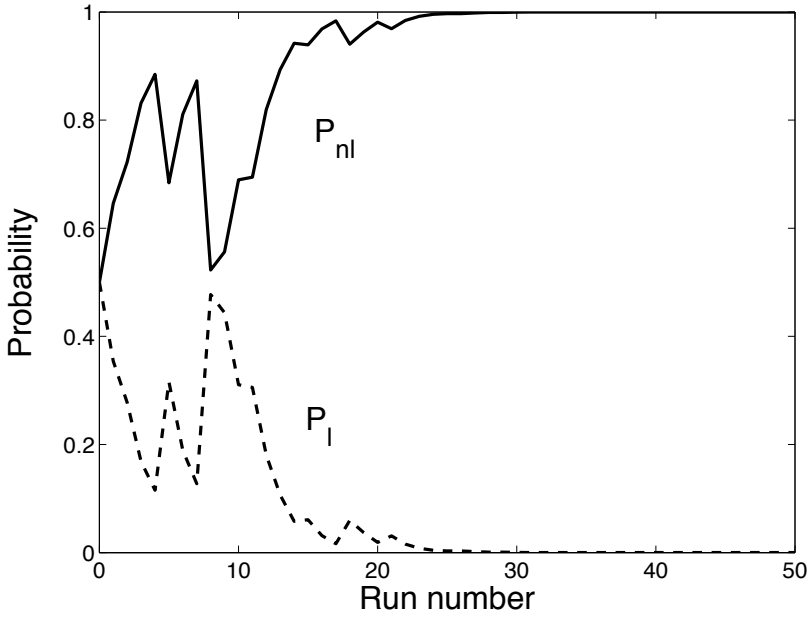

Figure 2.5: A simulated experiment showing the Bayesian analysis of the probability P_{nl}, that the photon scattering caused relative localisation of the particles (solid line) and the probability, P_l, that they were localised to begin with (dashed line). In our simulation, we have taken the particles to start off with no well-defined relative position.

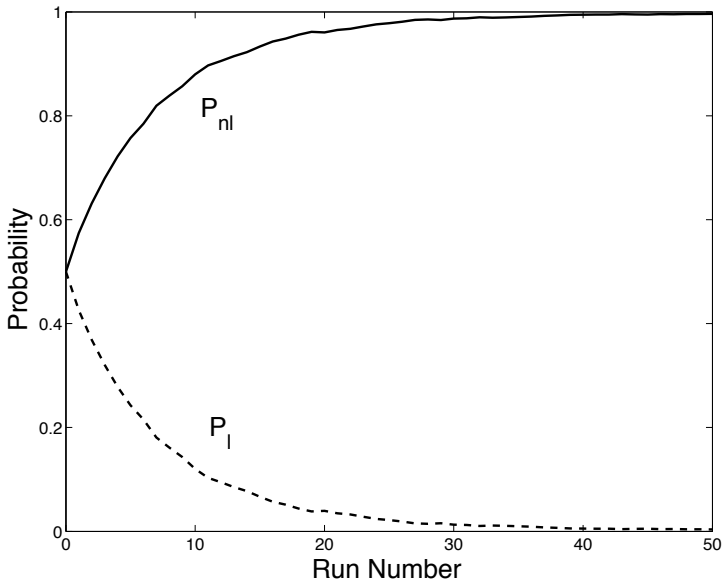

Figure 2.6: As in Figure 2.5 but averaged over 300 'experiments' to indicate the average number of runs that would be required to achieve a desired degree of confidence.

delocalised after 20 runs, we need to be able to measure the momentum of the particles with a resolution of $\delta p = 0.5[h/\lambda]$ or less. If we assume our proposed experiment to use Rb-87 atoms and a time of flight detector (Bücker *et al.*, 2009; Fuhrmanek *et al.*, 2010) of length 10mm, then the required momentum resolution of $\delta p = 0.5[h/\lambda]$ translates to a spatial resolution requirement of approximately $25\mu m$. Using time-of-flight fluorescence imaging (Bücker *et al.*, 2009; Fuhrmanek *et al.*, 2010) it is possible to spatially resolve the position of a single atom with resolution close to $1\mu m$ (Fuhrmanek *et al.*, 2010), and furthermore, Bücker *et. al.* achieve single atom detection with efficiency close to unity (Bücker *et al.*, 2009), so our required momentum measurement is achievable with current techniques.

2.4 Extension to three dimensions

In section 2.2 we recapped a scheme in which two particles, confined to a 1D line, can be localised by bombardment by photons. We now extend this scheme to a more 'real world' scenario where the particles are allowed to move in three

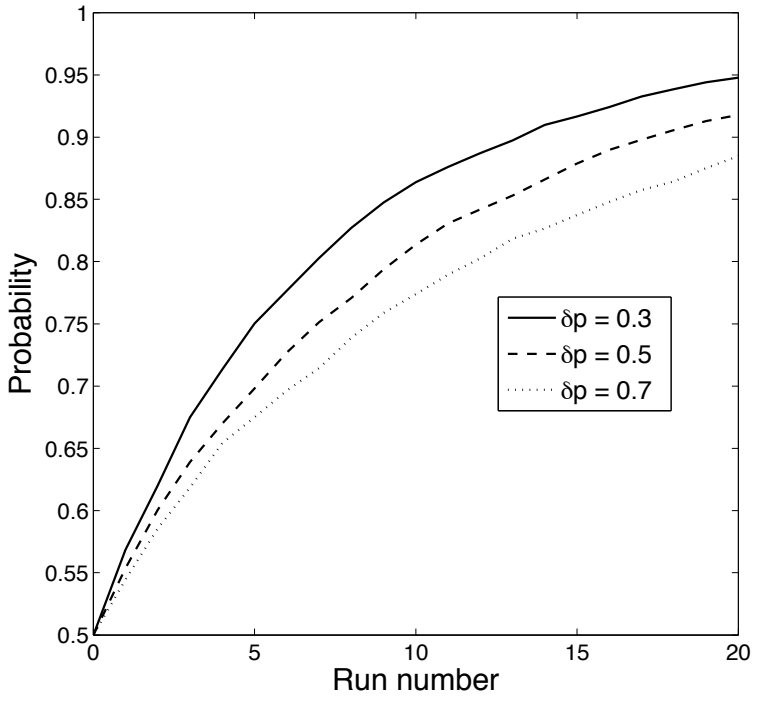

Figure 2.7: The plot shows the number of experimental runs used to build up our knowledge of the system on the x axis, and the probability that the atoms in our experiment were initially delocalised on the y axis. The three different curves show different values of the precision of momentum measurement: the values of δp here are in units of $[h/\lambda]$. We can see that a resolution of $\delta p = 0.5[h/\lambda]$ is needed for us to be 90% sure that the two particles were initially delocalised after 20 runs have been completed.

dimensions. Two distinguishable massive non-interacting particles are initially delocalised within a 3D cube of length $d = \lambda$, in the sense that their de Broglie wavelengths are comparable to d in this dimension. The particles are illuminated with plane-wave light of wavelength λ incident along the z-axis, which scatters from them and is detected at an angle (θ,ϕ) on a spherical screen located at a distance L from the particles, as shown in Fig. 2.8. The initial wave function of the particles is $c(x, y, z)$, where x,y and z represent the *relative* position of the two particles in Cartesian coordinates. The wavefunction $c(x, y, z)$ is normalised so that $\int\int\int_D |c(x, y, z)|^2 dxdydz = 1$, where D represents the box dimensions in which the particles are confined. As in the 1D case, we can neglect the centre-of-mass coordinate of the particles.

We now look at the scattering process: a photon of wavelength λ scatters off a particle into angle (θ, ϕ) in spherical coordinates where θ and ϕ are the polar and azimuthal angles, respectively. A deflected photon will impart the following momentum kick on one of the particles:

$$\begin{aligned}\Delta p_x &= \frac{h}{\lambda}\sin\theta\cos\phi \\ \Delta p_y &= \frac{h}{\lambda}\sin\theta\sin\phi \\ \Delta p_z &= \frac{h}{\lambda}(\cos\theta - 1)\end{aligned}$$

where h is Planck's constant. In relative momentum space the particles therefore receive a kick of $\pm\Delta p$ where $\Delta p = (\Delta p_x, \Delta p_y, \Delta p_z)$. Whether they receive a $+\Delta p$ or $-\Delta p$ kick depends on which particle the photon scatters from, but since this cannot be determined we obtain a superposition of both possibilities.

After one scattering event the state of the system is

$$\Psi(x, y, z, \theta, \phi) = \begin{cases} \frac{1}{4\sqrt{\pi}} c(x, y, z) \left(e^{\frac{i2\pi}{\lambda}\Gamma_{x,y,z}(\theta,\phi)} + e^{\frac{-i2\pi}{\lambda}\Gamma_{x,y,z}(\theta,\phi)} \right) & \text{if } (\theta, \phi) \neq (0, 0) \\ c(x, y, z)A(x, y, z) & \text{if } (\theta, \phi) = (0, 0) \end{cases}$$

where

$$\Gamma_{x,y,z}(\theta, \phi) = [x\sin\theta\cos\phi + y\sin\theta\sin\phi + z(\cos\theta - 1)]\,. \tag{2.7}$$

The nonscattering coefficient is given by

$$A^2(x,y,z) = \frac{1}{4\pi}\int_0^{2\pi}\int_0^{\pi} \sin\theta \sin^2\left(\frac{2\pi}{\lambda}\Gamma_{x,y,z}(\theta',\phi')\right) d\theta' d\phi'. \tag{2.8}$$

We now describe the localisation process, which works in the same way as the 1D case. The probability density for detecting a scattered photon at angle $(\theta,\phi) \neq (0,0)$ is $P_S(\theta,\phi)$, whereas for a nonscattered photon the probability density is $P_{NS}(0,0)$

$$\begin{aligned} P_S(\theta,\phi) &= \iiint_D |\Psi_{(\theta,\phi)\neq 0}|^2 dxdydz \\ P_{NS} &= \iiint_D |c(x,y,z)|^2 A^2\, dxdydz \end{aligned} \tag{2.9}$$

Counterintuitively, this means that detecting a nonscattered photon can actually give us information about the separation of the particles (Knott *et al.*, 2013).

A random number is then generated to see whether the photon is scattered and, if so, at what angle (θ_1,ϕ_1). The (unnormalised) states after the scattering process are as follows, for photons scattered at angle (θ_1,ϕ_1), and non scattered photons, respectively

$$\begin{aligned} \Psi_{\theta_1\phi_1} &= c(x,y,z)\cos\left(\frac{2\pi}{\lambda}\Gamma_{x,y,z}(\theta_1,\phi_1)\right) \\ \Psi_{00} &= c(x,y,z)A(x,y,z). \end{aligned} \tag{2.10}$$

We then normalise the state and repeat for the next photon.

We have chosen the initial probability density of the relative positions of the particles to be a flat distribution. We find that after successive photons are scattered off the particles, their relative positions localise, as shown by the probability distribution of the two particles in Fig. 2.9 after 150 photons have been scattered. We assume that the 150 photons are all incident on the particles in a sufficiently short time period that we do not need to consider the dynamics of the particles between detection events. The symmetry of the high probability density regions about the origin in Fig. 2.9 reflects the fact that the two particles are interchangeable, and that the localisation is a result of successive superpositions of $+ve$ and $-ve$ relative momentum kicks. This is the desired result: it shows

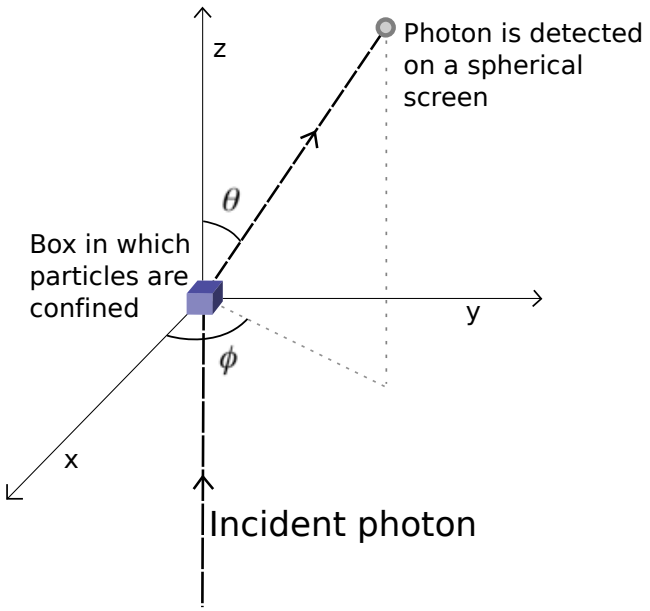

Figure 2.8: This diagram illustrates the experiment in which two massive particles are delocalised over the volume of a cube with side length d. Plane-wave light with wavelength λ incident along the z-axis scatters from the particles and is detected at an angle (θ,ϕ) on a spherical screen located at a distance L from the particles. For clarity, the diagram is not to scale: we consider the case where $L \gg d$.

that scattering induced localisation can be extended to the more realistic case of particles that are allowed to move in three dimension. As in the one dimensional case, it is important to note that the localisation is strictly in *relative* position space: no *absolute* position localisation has occurred.

2.5 Chapter conclusion

In this chapter we have described an experiment that could be used to confirm that localisation of particles can be caused by photon scattering. The technology needed to implement this scheme has already been developed (Bücker *et al.*, 2009; Fuhrmanek *et al.*, 2010) and furthermore the required momentum measurement precision is currently achievable. We expect that the proposed experiment

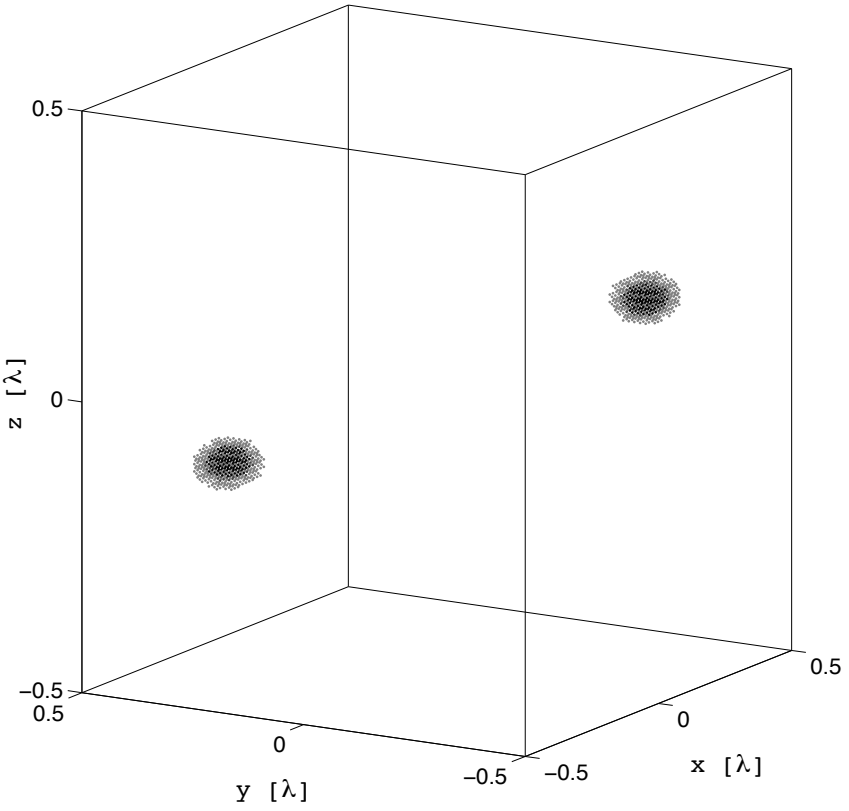

Figure 2.9: This plot shows the probability density $P(x)$, represented by the density and shading of points, for the relative position of the particles after the scattering and detection of 150 photons. The two high density dark clouds show that as in the 1D case, light scattering has caused relative position localisation. The position is given in units of the wavelength, λ, of the scattered light.

will provide evidence that particles confined to one dimension can undergo a process whereby quantum entanglement causes classical localisation in *relative* position space. We have also extended the scheme from a one dimensional proof of principle to the more real world scenario of three dimensional relative position localisation, giving further weight to an exciting new explanation of how the uneasy gap between the classical and quantum worlds can be bridged.

Chapter 3

Beating the classical limit with quantum metrology

In this chapter we turn back to the main topic of this thesis: quantum metrology. We will begin by describing how the classical limit can be obtained in optical quantum metrology. We then show how quantum entanglement can be used to beat this bound and obtain the 'Heisenberg limit', which is the ultimate precision with which a quantum system can measure a linear phase shift. The problems with using entangled states are then discussed, which will provide motivation for later chapters of this thesis in which we seek nonclassical states that overcome these difficulties.

This chapter serves as an introduction to the various states we will utilise for quantum metrology, and therefore, with the exception of section 3.4, is not our original work.

3.1 The Mach-Zehnder interferometer

We will begin by explaining the archetypal quantum metrology device for optical systems: the Mach-Zehnder interferometer, as shown in Fig. 3.1. The first step in this device is to produce a beam of photons from a light source and then split the beam into two paths with a beam splitter (beam splitters will be described shortly). Next, one of the paths undergoes a linear phase shift ϕ, which we wish to measure, and then the two paths are recombined at a second beam splitter.

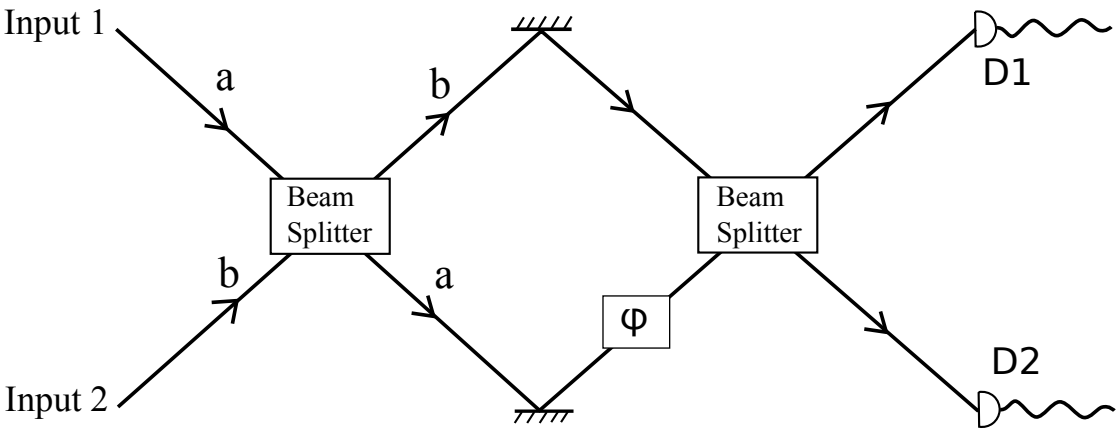

Figure 3.1: A Mach-Zehnder interferometer which can be used to measure a phase ϕ. Photons are sent through the beam splitters and the linear phase shift, and are then measured at the photon number counting detectors $D1$ and $D2$.

The resulting output can be measured by detectors $D1$ and $D2$, which are used to extract the phase information. The phase can correspond to a large range of physical phenomena, from a length change in the interferometer arms caused by a gravitational wave (Abadie *et al.*, 2012), to a time delay picked up from measuring a material sample: this formalism is very general. A famous use of interferometry came in 1887, when Michelson and Morley used a folded Mach-Zehnder interferometer, as shown in Fig. 3.2, to show that the speed of light is a constant regardless of the speed and direction that you are traveling (Michelson & Morley, 1887). This remarkable experiment paved the way for Einstein's special relativity and subsequently general relativity.

To analyse the precision attainable in optical interferometry we begin by sending a single photon through the Mach-Zehnder interferometer in Fig. 3.1. A single photon is described in Fock notation as $|1\rangle$, which can also be seen as the creation operator, $\hat{a}^\dagger$, acting on the vacuum:

$$|1\rangle = \hat{a}^\dagger|0\rangle. \tag{3.1}$$

We describe an input of one photon in each port by

$$|1,1\rangle = \hat{a}^\dagger\hat{b}^\dagger|0,0\rangle_{a,b}, \tag{3.2}$$

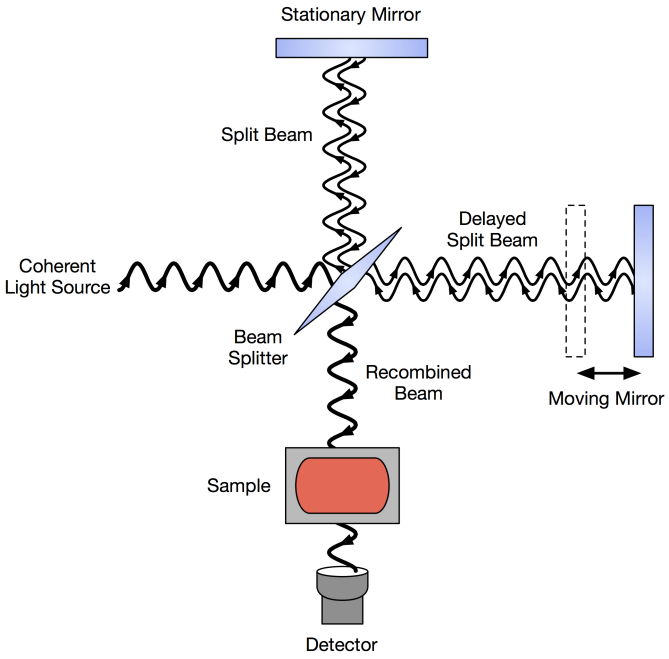

Figure 3.2: The Michelson interferometer, which is mathematically equivalent to a Mach-Zehnder interferometer, was used to show that the speed of light is a constant regardless of the speed and direction that you are traveling (Michelson & Morley, 1887) (public domain image).

where the subscript refers to paths a and b, and therefore our desired input of a single photon entering the upper port of the interferometer is $|\Psi_0\rangle = |1,0\rangle$. The beam splitter is described by the unitary operator $\hat{U}_B = e^{-i\theta(e^{i\phi_b}\hat{a}^\dagger\hat{b}+e^{-i\phi_b}\hat{b}^\dagger\hat{a})}$, where for a 50:50 beam splitter[1] we take $\theta = \pi/4$, and are able to choose the arbitrary phase to be $\phi_b = -\pi/2$, giving: $\hat{U}_B = e^{-\frac{\pi}{4}(\hat{a}^\dagger\hat{b}-\hat{b}^\dagger\hat{a})}$. The effect of the 50:50 BS on the creation operators can be found to be

$$\begin{aligned} \hat{a}^\dagger &\to \hat{U}_B\hat{a}^\dagger\hat{U}_B^\dagger = \frac{1}{\sqrt{2}}(\hat{a}^\dagger + \hat{b}^\dagger) \\ \hat{b}^\dagger &\to \hat{U}_B\hat{b}^\dagger\hat{U}_B^\dagger = \frac{1}{\sqrt{2}}(b^\dagger - \hat{a}^\dagger). \end{aligned} \tag{3.3}$$

This means that the beam splitter $\hat{U}_B$ acts on the input state $|\Psi_0\rangle = |1,0\rangle$ as follows:

$$\begin{aligned} |\Psi_1\rangle &= \hat{U}_B|1,0\rangle = \hat{U}_B\hat{a}^\dagger|0,0\rangle = \hat{U}_B\hat{a}^\dagger\hat{U}_B^\dagger\hat{U}_B|0,0\rangle \\ &= \hat{U}_B\hat{a}^\dagger\hat{U}_B^\dagger|0,0\rangle = \frac{1}{\sqrt{2}}(\hat{a}^\dagger + \hat{b}^\dagger)|0,0\rangle \\ &= \frac{1}{\sqrt{2}}(|1,0\rangle + |0,1\rangle). \end{aligned} \tag{3.4}$$

Thus the effect of the beam splitter on a single photon is to create a superposition of the photon over the two paths. Next we apply the linear phase shift, $\hat{U}_\phi = e^{i\hat{n}_a\phi}$, where $\hat{n}_a = \hat{a}^\dagger\hat{a}$ count the number of photons on path a. This gives

$$|\Psi_2\rangle = U_\phi|\Psi_1\rangle = \frac{1}{\sqrt{2}}(e^{i\phi}|1,0\rangle + |0,1\rangle). \tag{3.5}$$

After passing through the rest of the interferometer our final state is $|\Psi_3\rangle = \hat{U}_B|\Psi_2\rangle$. We can then find the probability to detect a photon at detector $D1$ to be

$$P_{D1} = |\langle 1,0|\Psi_3\rangle|^2 = \sin^2(\phi/2) \tag{3.6}$$

and similarly $P_{D2} = \cos^2(\phi/2)$. Soon we will show how these probabilities can be used to find the phase ϕ, but first we would like to consider the precision with which the phase can be measured. If we send a stream of N particles

[1] More generally we can take $\eta = \cos^2\theta$ as the transmissivity of the beam splitter.

through the interferometer, then the average number at the output $D1$ will be $\langle \hat{n}_a \rangle = N\langle \Psi_3 | \hat{n}_a | \Psi_3 \rangle = N \sin^2(\phi/2)$. It can then be shown that the propagation of errors formula can be used to find the precision with which we can measure the phase, $\delta\phi$, when we count the photons at the output $D1$. This is given by (Dunningham & Kim, 2006)

$$\delta\phi = \frac{\delta\hat{n}_a}{|\frac{\partial\langle\hat{n}_a\rangle}{\partial\phi}|}. \tag{3.7}$$

If we apply this formula to our example of sending a stream of single photons through a Mach-Zehnder interferometer, it has been shown in (Dunningham & Kim, 2006) that

$$\delta\phi = \frac{1}{\sqrt{N}}, \tag{3.8}$$

the shot noise limit (SNL).

We will now explain how an experimentalist can determine the value of the phase ϕ by counting the number of photons at detector $D1$. To do this we have to make use of Bayesian analysis, which was introduced in section 2.3. We begin by writing the probability of detecting a particle at $D1$ *given* that the phase is ϕ:

$$P(D1|\phi) = \sin^2(\phi/2). \tag{3.9}$$

We would now like to simulate an experiment that will determine the phase. The actual phase to be measured is some given constant ϕ_0. The conditional probability of detecting a photon at $D1$, *given* that the phase is ϕ_0 is $P(D1|\phi_0)$. In each run of the simulation, the result of the measurement at $D1$ is a random outcome sampled from the probability distribution $P(D1|\phi_0)$. Let $D1 = 1$ ($D1 = 0$) describe the result when a photon was measured (not measured) at $D1$. Then, for example, the first run of our simulation might result in a measurement $D1 = 1$. To determine the phase from this outcome, we invoke Bayes' theorem (described in section 2.3):

$$P(A|B) \propto P(B|A). \tag{3.10}$$

We can therefore calculate

$$P(\phi|D1 = 1) \propto P(D1 = 1|\phi). \tag{3.11}$$

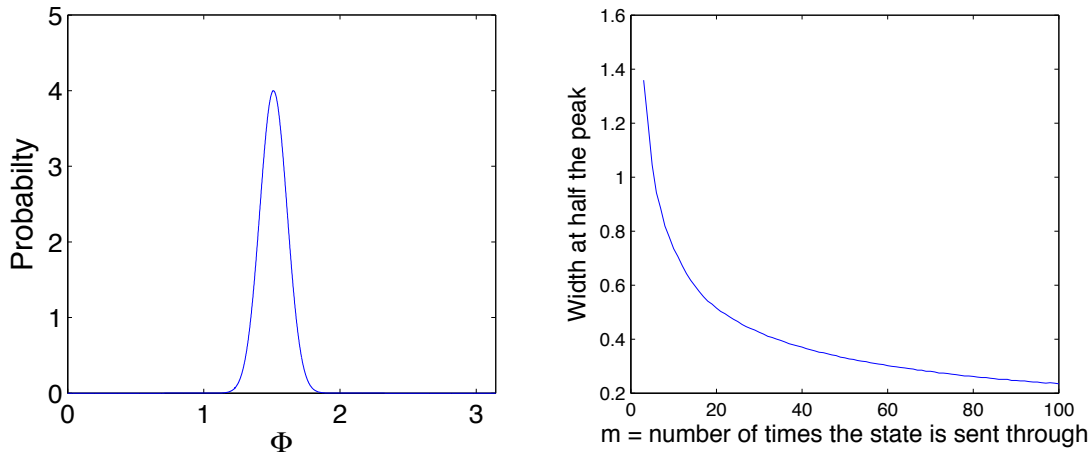

Figure 3.3: The left hand graph shows an experimenter's knowledge of a phase ϕ after 100 unentangled states are sent through an interferometer: the y axis of this plot is the probability density. This figure is obtained by simulating an experiment in which an experimenter repeatedly measures photons outputting from a Mach-Zehnder interferometer. Bayes theorem is then used, as described in the main text, to obtain this probability distribution. Here $\phi_0 = \pi/2$. The right hand graph shows how the width at half the probability density peak changes as the number of states sent through the interferometer increases. The shape of this slope is $\delta\phi \propto 1/\sqrt{m}$, the shot noise limit.

As the probability distribution sums to one, we can normalise this distribution to be left with $P(\phi|D1 = 1)$: the probability distribution for different phases ϕ *given* that $D1 = 1$ has been measured on the first run of their experiment. In our simulation we repeat these steps, obtaining more knowledge about the phase. With each new measurement we use Bayesian analysis (as was done in equation 2.6) to update our knowledge of the phase: i.e. after the first detection we multiply our initial knowledge of the phase $P_i(\phi)$ by $P(\phi|D1 = 1)$. We then renormalise, and repeat this process for each successive measurement of the phase shift. After a number of repeats, the experimenter is left with a probability distribution $P(\phi)$, which is the probability distribution for ϕ, given all previous measurements of $D1$.

We have simulated this experiment, with the results given by the left hand graph in Fig. 3.3, in which the state $|1,0\rangle$ was sent through the interferometer 100 times. It can be seen that the probability density has a peak around $\pi/2$: it is the width of this probability density peak that tells us the precision of the phase measurement, $\delta\phi$. In the right hand graph of Fig. 3.3 we plot the number of times the state is sent through the interferometer, N, against the width at half the probability density peak. The slope of this graph gives us the relation $\delta\phi \propto 1/\sqrt{N}$, which is again the SNL.

3.2 The NOON state: Using entanglement to beat the SNL

We now wish to send an entangled state through the interferometer to see whether we can improve on this measurement precision. We will start by looking at the so called NOON state (Lee *et al.*, 2002), which is a maximally entangled state of all the photons in the upper path, in a superposition with all the photons in the lower path:

$$|\Psi\rangle_{NOON} = \frac{1}{\sqrt{2}}\left[|N,0\rangle + i|0,N\rangle\right]. \tag{3.12}$$

In order to create the NOON state we replace the first beam splitter in the interferometer in Fig. 3.1 by an alternative unitary known as the 'quantum beam splitter' (QBS) (Dunningham & Kim, 2006; Gerry *et al.*, 2002). As shown in Dunningham & Kim (2006) a quantum beam splitter involves an ordinary interferometer, but with a nonlinearity in one arm, and has the following effect on state $|N,0\rangle$:

$$|N,0\rangle \xrightarrow{\text{QBS}} \frac{1}{\sqrt{2}}\left[|N,0\rangle + e^{i\zeta}|0,N\rangle\right]. \tag{3.13}$$

In order to simplify our analysis, we take $\zeta = \frac{\pi}{2}$, but in general the value of ζ depends on the specific method of implementing the QBS. The QBS acts on $|0,N\rangle$ as

$$|0,N\rangle \xrightarrow{\text{QBS}} \frac{1}{\sqrt{2}}\left[|0,N\rangle + i|N,0\rangle\right] \tag{3.14}$$

After creating the NOON state, we then apply the phase shift to one of the paths in the interferometer, as we did with the unentangled state. The effect of this phase shift is

$$\frac{1}{\sqrt{2}}\left[|N,0\rangle + i|0,N\rangle\right] \xrightarrow{\text{Phase}\,\phi} \frac{1}{\sqrt{2}}\left[e^{iN\phi}|N,0\rangle + i|0,N\rangle\right]. \tag{3.15}$$

We can then send this state through a second QBS, and measure the number of photons in at the detectors. We find that either *all* the photons are detected at $D1$ or *all* the photons are detected at $D2$, with the following probabilities (Dunningham & Kim, 2006):

$$\begin{aligned} P_{D1} &= \sin^2\left(N\phi/2\right) \\ P_{D2} &= \cos^2\left(N\phi/2\right). \end{aligned} \tag{3.16}$$

Notice the N-fold phase enhancement, which has the effect of making the observed interference fringes vary N times faster than for unentangled photons. If we send a NOON state of N photons through this scheme, then using a similar analysis as for the unentangled photons the precision of phase measurement can be seen to vary as $\delta\phi \propto 1/N$, the Heisenberg limit. We can also show this result by using the propagation of errors formula in equation 3.7 which again gives the Heisenberg limit:

$$\delta\phi = \frac{\delta\hat{n}_a}{|\frac{\partial\langle\hat{n}_a\rangle}{\partial\phi}|} = \frac{1}{N}. \tag{3.17}$$

Using the maximally entangled NOON state therefore gives us a $1/\sqrt{N}$ precision enhancement over the unentangled case. However, there a number of issues with using NOON states for phase measurements, as we will discuss next.

3.3 The problems with NOON states

The main problem with NOON states becomes apparent when we consider decoherence. The most applicable model of decoherence for optical interferometry is photon loss (Demkowicz-Dobrzanski *et al.*, 2014; Rubin & Kaushik, 2007), which we will describe in detail in the next chapter. For now, however, we will consider

decoherence as a crude measurement of our system by the environment. Measurements of a quantum system in a superposition state collapse the state into one of the superposition's components. Hence, qualitatively, the effect of decoherence on a NOON state is to collapse it as follows

$$\frac{1}{\sqrt{2}}\left[e^{in\phi}|N,0\rangle + i|0,N\rangle\right] \rightarrow e^{in\phi}|N,0\rangle \; or \; |0,N\rangle. \tag{3.18}$$

We therefore no longer have a superposition state: half the time we are left with $e^{in\phi}|N,0\rangle$, and the other half we have $|0,N\rangle$. Clearly in the second case we cannot determine the phase from $|0,N\rangle$. But we also can't determine the phase from $e^{in\phi}|N,0\rangle$, as it is a global phase and constitutes nothing that can be measured. The result is that if we lose just one photon from a NOON state we lose all the phase information it contained, rendering the state useless.

To try and combat this fragility a number of clever schemes have been devised with robustness to loss which still capture sub shot noise limit precision, albeit not quite at the Heisenberg limit. An example of one of these schemes is a NOON 'chopping' strategy (Dorner *et al.*, 2009), in which multiple smaller NOONs are sent through an interferometer instead of one big one - we will discuss this in chapter 5. Other examples include unbalanced NOON states (Demkowicz-Dobrzanski *et al.*, 2009), Holland and Burnett states (Holland & Burnett, 1993), and mixtures of unentangled and NOON states (Gkortsilas *et al.*, 2012). While these states can beat the shot noise limit when loss is included, they are still fragile, and with large amounts of loss they don't achieve quantum enhancement.

Another problem with NOON states is that they are very difficult to produce. The scheme described briefly above and in Dunningham & Kim (2006) uses a nonlinearity, which poses large experimental challenges. To the author's knowledge the largest optical NOON state that has been created is for $N = 5$ (Afek *et al.*, 2010), whereas for atoms NOON states with $N = 10$ have been made (Jones *et al.*, 2009). We therefore wish to seek quantum states that have the potential to be created using scalable technology for larger photon numbers, in order to gain the most from quantum-enhanced measurements. We now look to a state that shows significantly greater robustness to loss, and the potential to be made as a larger-photon-number entangled state.

3.4 Entangled coherent states

We now turn to a state that shows intrinsic robustness to photon losses: the entangled coherent state (ECS)(Gerry *et al.*, 2002; Sanders, 2012, 1992). We first introduce the coherent state (CS), which is defined as

$$|\alpha\rangle = e^{-\frac{|\alpha|^2}{2}} \sum_{n=0}^{\infty} \frac{\alpha^n}{\sqrt{n!}} |n\rangle = \hat{D}(\alpha)|0\rangle \tag{3.19}$$

where $\hat{D}(\alpha)$ is the displacement operator: $\hat{D} = e^{\alpha\hat{a}^\dagger - \alpha^*\hat{a}}$. A coherent state can therefore be seen as a displaced vacuum or, alternatively, a superposition of number states. In an ideal phase stabilised laser, a coherent state is produced (Demkowicz-Dobrzanski *et al.*, 2014; Glauber, 1963). We see a glimpse of the potential of a coherent state when we operate on it with the annihilation operator:

$$\hat{a}|\alpha\rangle = e^{-\frac{|\alpha|^2}{2}} \sum_{n=1}^{\infty} \frac{\alpha^n}{\sqrt{n!}} \sqrt{n}|n-1\rangle = \alpha|\alpha\rangle. \tag{3.20}$$

Coherent states are therefore eigenstates of the annihilation operator: removing a photon from a coherent state leaves the state unchanged (this is discussed in more detail in section 4.1). This fact gives us great hope, as a state which is robust to loss is exactly what we want for quantum metrology (Joo *et al.*, 2011). In order to achieve quantum enhanced measurement, we still need to create an *entangled* coherent state (ECS). One way to do this is using the QBS. If we take an initial state

$$|\psi_0\rangle = |\alpha, 0\rangle = e^{-\frac{|\alpha|^2}{2}} \sum_{n=0}^{\infty} \frac{\alpha^n}{\sqrt{n!}} |n, 0\rangle, \tag{3.21}$$

then the effect of the QBS is to produce the normalised ECS $|\psi_2\rangle$:

$$\begin{aligned} |\psi_0\rangle \xrightarrow{\text{QBS}} & \frac{e^{-\frac{|\alpha|^2}{2}}}{\sqrt{2}} \sum_{n=0}^{\infty} \frac{\alpha^n}{\sqrt{n!}} \left[|n, 0\rangle + i|0, n\rangle\right] \\ & = \frac{1}{\sqrt{2}} \left(|\alpha, 0\rangle + i|0, \alpha\rangle\right) = |\psi_1\rangle. \end{aligned} \tag{3.22}$$

We then perform a phase shift:

$$|\psi_1\rangle \xrightarrow{\text{phase }\phi} \frac{e^{-\frac{|\alpha|^2}{2}}}{\sqrt{2}} \sum_{n=0}^{\infty} \frac{\alpha^n}{\sqrt{n!}} \left[e^{in\phi}|n,0\rangle + i|0,n\rangle\right] \tag{3.23}$$
$$= \frac{1}{\sqrt{2}} \left[|\alpha e^{i\phi},0\rangle + i|0,\alpha\rangle\right] = |\psi_2\rangle.$$

Notice that the phase shift is now *inside* the ket. If we look at the crude decoherence model that we applied to the NOON state, then our state will collapse as follows:

$$\frac{1}{\sqrt{2}} \left[|\alpha e^{i\phi},0\rangle + i|0,\alpha\rangle\right] \rightarrow |\alpha e^{i\phi},0\rangle \; or \; |0,\alpha\rangle. \tag{3.24}$$

If we are left with $|0,\alpha\rangle$ then, just as for the NOON state, we cannot gain any phase information. However, if we are left with the state $|\alpha e^{i\phi},0\rangle$ then the phase ϕ is still, at least in principle, measurable. In the next chapter we will look at the relevant decoherence mechanism - photon loss - in more detail, and we will devise a scheme that can be used to recover the phase information, hence showing that ECSs are more robust than NOON states.

We will now continue with the loss free scenario of using an ECS to measure a phase. Taking the state after the phase shift, $|\psi_2\rangle$, we then send this through a second QBS:

$$|\psi_2\rangle \xrightarrow{\text{QBS}} \tag{3.25}$$
$$\frac{e^{-\frac{|\alpha|^2}{2}}}{\sqrt{2}} \sum_{n=0}^{\infty} \frac{\alpha^n}{\sqrt{n!}} \left(e^{in\phi} \frac{1}{\sqrt{2}} \left[|n,0\rangle + i|0,n\rangle\right] + i \frac{1}{\sqrt{2}} \left[|0,n\rangle + i|n,0\rangle\right] \right) = |\psi_3\rangle,$$

which simplifies to

$$|\psi_3\rangle = e^{-\frac{|\alpha|^2}{2}} \sum_{n=0}^{\infty} \frac{\alpha^n}{\sqrt{n!}} i e^{\frac{in\phi}{2}} \left(|n,0\rangle \sin\frac{n\phi}{2} + |0,n\rangle \cos\frac{n\phi}{2} \right). \tag{3.26}$$

From this we can calculate the probability of detecting different numbers of photons at the outputs. To do this we first take the inner product of $|\psi_3\rangle$ with $|n_1,n_2\rangle = |n_1\rangle_{D1}|n_2\rangle_{D2}$, i.e. the state with n_1 photons at detector $D1$ and n_2 photons at detector $D2$. This gives us

$$\langle n_1,n_2|\psi_3\rangle = i e^{-\frac{|\alpha|^2}{2}} \left[\frac{\alpha^{n_1}}{\sqrt{n_1!}} e^{\frac{in_1\phi}{2}} \sin\frac{n_1\phi}{2} \delta_{n_2,0} + \frac{\alpha^{n_2}}{\sqrt{n_2!}} e^{\frac{in_2\phi}{2}} \cos\frac{n_2\phi}{2} \delta_{n_1,0} \right]. \tag{3.27}$$

The Kronecker deltas here tell us that it is impossible to detect photons at **both** outputs. This is clearly true as any photon detection collapses the state into either $|n,0\rangle$ **or** $|0,n\rangle$. We can now calculate the probabilities of different numbers of photons being detected, given that the phase in the interferometer is ϕ_1:

$$P(n_1,n_2|\phi=\phi_1)=|\langle n_1,n_2|\psi_3\rangle|^2=\begin{cases} e^{-|\alpha|^2}\frac{|\alpha|^{2n_1}}{n_1!}\sin^2\frac{n_1\phi_1}{2} & \text{for } n_1\neq 0\,, n_2=0 \\ e^{-|\alpha|^2}\frac{|\alpha|^{2n_2}}{n_2!}\cos^2\frac{n_2\phi_1}{2} & \text{for } n_1=0\,, n_2\neq 0 \\ e^{-|\alpha|^2} & \text{for } n_1=n_2=0 \\ 0 & \text{for } n_1\neq 0\,, n_2\neq 0. \end{cases} \tag{3.28}$$

Using these probabilities we can use a similar Bayesian scheme as we did for the unentangled photons to determine the value of the phase ϕ, and the precision with which the phase can be measured, $\delta\phi$. Fig. 3.4 shows the results for this measurement scheme, given by the purple crossed line, compared to the NOON state given by the blue dashed line.

This result shows an interesting property of the ECS: it appears to beat the Heisenberg limit, despite the Heisenberg limit supposedly being the fundamental limit. In fact, the Heisenberg limit is defined for states with fixed numbers of photons, like the NOON state. The ECS, on the other hand, has a variable number of photons. Thus to compare the ECS and the NOON we look at the average number of photons in the ECS, and the precision limit for varying photon numbers is given by the Hofmann limit (Hofmann, 2009):

$$\delta\phi=1/\sqrt{\langle N^2\rangle}, \tag{3.29}$$

i.e. by considering the average of the squared photon numbers. Many works in the literature claim to beat the Heisenberg limit (Anisimov *et al.*, 2010; Sahota & James, 2013), but we believe this claim to be dubious as it arises from stating the Heisenberg limit incorrectly as $1/\bar{N}$ where $\bar{N}$ is the average number of photons. Despite this, for most of this thesis we are concerned with the absolute precision attainable by various states, and in this case states such as the ECS are able to gain better precision than the maximal fixed number state, the NOON state, and so this is a clear advantage of ECSs, at least for small photon numbers.

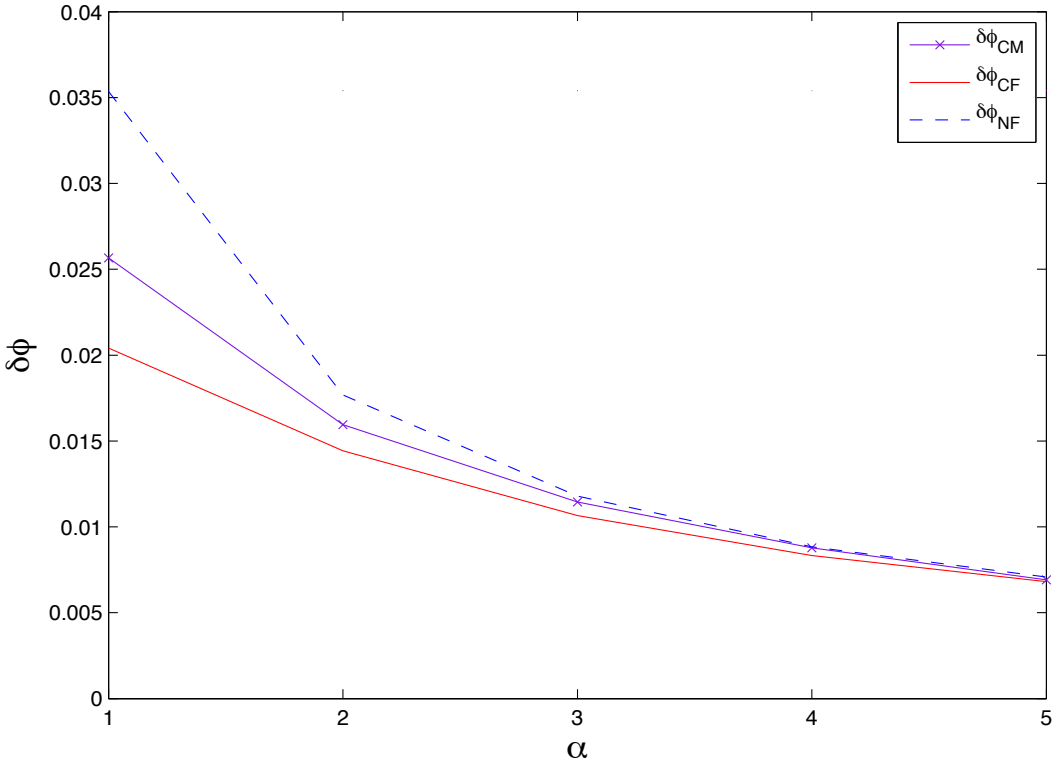

Figure 3.4: The phase precision of the ECS with no loss is shown here. We plot different sized ECSs against their precision. Here (and in later figures) $\delta\phi_{CM}$ is the ECS using the measurement scheme described in section 3.4, $\delta\phi_{CF}$ is the QFI for the ECS and $\delta\phi_{NF}$ is the (equivalent size) NOON state, or the Heisenberg limit. A stream of single particles (i.e. at the SNL) measure at precision 0.0354.

In Fig. 3.5 we have plotted a typical simulation for determining a phase ϕ with a NOON state, on the left, and an ECS, on the right. We see that the NOON state only gives the phase up to modulo π/N. This means that in order to determine the correct phase with a NOON state we need to have some idea of the phase to begin with. This is not the case with an ECS: the correct phase is given, and therefore we save some resources. This exhibits another advantage of the ECS over the NOON state, even before we have considered loss.

Up to this point we have only considered the precision with which each state can measure a phase given a specific measurement scheme: in all three cases (single photons, NOON states, ECSs) this measurement scheme involved counting

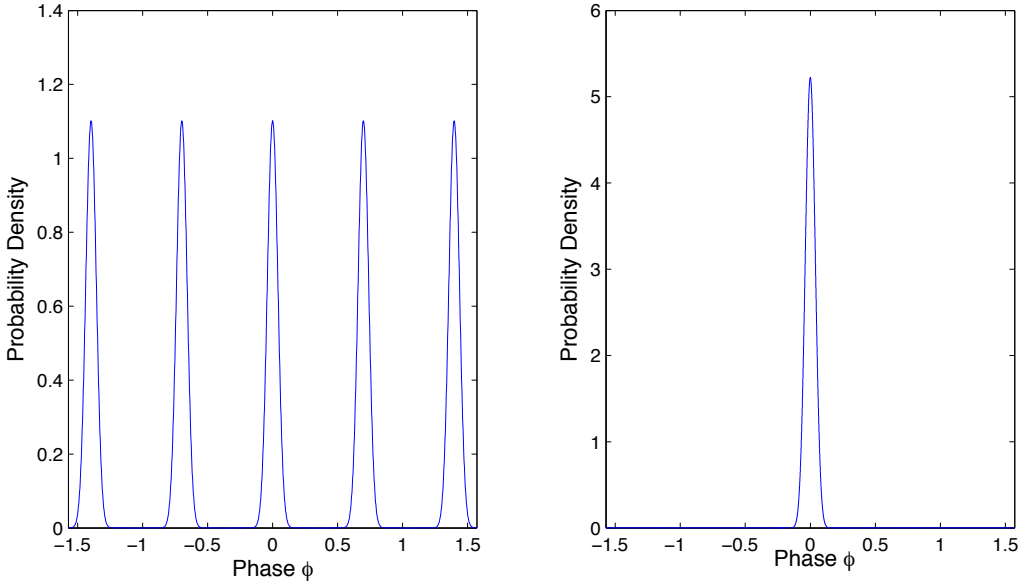

Figure 3.5: Comparing phase estimation results for NOON states on the left and ECS on the right. It can clearly be seen that the ECS gives the correct phase, whereas NOON states only give the phase to modulo π/N.

the number of photons at the output. But have we chosen the optimal measurement schemes in these examples, or is there some other measurement scheme that can gain a better precision given the same states? The quantum Fisher information (QFI) allows us to answer this question, as it provides a way of optimising over all possible measurements, to tell us the best possible precision with which a state can measure a phase. As we will see next, this means that the QFI gives us a very effective way of comparing different states' potential for determining a phase, regardless of the specific measurement scheme that is to be implemented.

3.5 Comparing different states with the quantum Fisher information

The quantum Cramér-Rao bound tells us the minimum possible uncertainty in estimating a parameter ϕ given a particular quantum state $\rho(\phi)$, and is given by

(Braunstein & Caves, 1994; Paris, 2009)

$$\delta\phi \geq \frac{1}{\sqrt{NF_Q}} \tag{3.30}$$

where F_Q is the quantum Fisher information (QFI) for $\rho(\phi)$. The QFI optimises over all possible measurements that can be made on the state $\rho(\phi)$, and, qualitatively, is a measure of the amount of information that a state contains about the parameter ϕ. The QFI is given by (Cooper *et al.*, 2010; Paris, 2009; Zhang *et al.*, 2013)

$$F_Q = \mathrm{Tr}\left(\rho A^2\right) \tag{3.31}$$

where A is defined by solving the symmetric logarithmic derivative:

$$\frac{\partial\rho}{\partial\phi} = \frac{1}{2}\left[A\rho + \rho A\right]. \tag{3.32}$$

This is not an easy equation to work with; we will derive an alternative form explicitly in terms of the state ρ and its eigenvalues and eigenvectors. We begin by diagonalising ρ to get the eigenvalues and eigenvectors: $\rho|\lambda_i\rangle = \lambda_i|\lambda_i\rangle$. We can then write

$$\begin{aligned}\left(\frac{\partial\rho}{\partial\phi}\right)_{ij} &= \langle\lambda_i|\frac{\partial\rho}{\partial\phi}|\lambda_j\rangle \\ &= \frac{1}{2}\left[\langle\lambda_i|A\rho|\lambda_j\rangle + \langle\lambda_i|\rho A|\lambda_j\rangle\right] \\ &= \frac{1}{2}\left[\lambda_j\left(A\right)_{ij} + \lambda_i\left(A\right)_{ij}\right].\end{aligned} \tag{3.33}$$

We then solve to find A:

$$\left(A\right)_{ij} = \frac{2\langle\lambda_i|\frac{\partial\rho}{\partial\phi}|\lambda_j\rangle}{\lambda_i + \lambda_j}. \tag{3.34}$$

We then use

$$F_Q = \mathrm{Tr}\left(\rho A^2\right) = \frac{1}{2}\left[\mathrm{Tr}\left(A^2\rho\right) + \mathrm{Tr}\left(A\rho A\right)\right] = \mathrm{Tr}\left(A\frac{\partial\rho}{\partial\phi}\right). \tag{3.35}$$

This allows us to calculate

$$F_Q = \sum_{i,j}\frac{2}{\lambda_i + \lambda_j}\left|\langle\lambda_i|\partial\rho(\phi)/\partial\phi|\lambda_j\rangle\right|^2. \tag{3.36}$$

When we come to look at loss in optical interferometry, it is this equation for the QFI that we will use, and it will prove to be very useful in comparing different states. However, note that in order to use this equation, the density matrix ρ that describes our system must be diagonalised to find the eigenvectors and eigenvalues. The difficulties and solutions concerning this task will be discussed in length in the coming chapters.

For now, we will stick to the much simpler loss free scenario, in which our state remains a pure state, so that $\rho^2 = \rho = |\Psi\rangle\langle\Psi|$. Then

$$\frac{\partial\rho}{\partial\phi} = \frac{\partial\rho^2}{\partial\phi} = \rho\frac{\partial\rho}{\partial\phi} + \frac{\partial\rho}{\partial\phi}\rho. \tag{3.37}$$

Comparing this with equation 3.32 we get: $A = 2\frac{\partial\rho}{\partial\phi}$ and $F_Q = 4\mathrm{Tr}\left[\rho\left(\frac{\partial\rho}{\partial\phi}\right)^2\right]$. We then find

$$F_Q = 4\left[\langle\Psi'|\Psi'\rangle - |\langle\Psi'|\Psi\rangle|^2\right] \tag{3.38}$$

where $|\Psi'\rangle = \frac{\partial}{\partial\phi}|\Psi\rangle$. Hence the QFI of pure states can be calculated with relative ease, and we will show how we can do this next. After we have found the QFI for a state, we can use the quantum Cramér-Rao bound (QCRB) to find the best attainable precision for parameter estimation, given our state ρ or $|\Psi\rangle$. The QCRB is

$$\delta\phi \geq \frac{1}{\sqrt{mF_Q}}, \tag{3.39}$$

where m is the number of classical repeats of our experiment.

3.6 Quantum Fisher information of the NOON state and the ECS

We begin by looking at the case of sending a NOON state through an interferometer, as described in section 3.2 above. The state after the phase shift is

$$|\Psi\rangle = \frac{1}{\sqrt{2}}(e^{iN\phi}|N,0\rangle + i|0,N\rangle). \tag{3.40}$$

In order to find the QFI in 3.38 we need to differentiate this state with respect to the phase:

$$|\Psi'\rangle = \frac{\partial|\Psi\rangle}{\partial\phi} = \frac{iN}{\sqrt{2}}e^{iN\phi}|N,0\rangle. \tag{3.41}$$

We then find

$$\langle\Psi'|\Psi'\rangle = N^2/2 \tag{3.42}$$

and

$$\langle\Psi|\Psi'\rangle = iN/2. \tag{3.43}$$

We can then calculate the QFI to be

$$F_Q = 4\left[\langle\Psi'|\Psi'\rangle - |\langle\Psi'|\Psi\rangle|^2\right] = N^2. \tag{3.44}$$

Using the QCRB, for a single experimental run, so that $m = 1$, we find

$$\delta\phi = \frac{1}{\sqrt{mF_Q}} = \frac{1}{N}, \tag{3.45}$$

which is the Heisenberg limit. It is now easy to analyse a stream of m single photons, as in section 3.1, which has the initial state

$$|\Psi\rangle = \frac{1}{\sqrt{2}}(e^{i\phi}|1,0\rangle + |0,1\rangle) \tag{3.46}$$

which leads to $F_Q = 1$, and therefore

$$\delta\phi = \frac{1}{\sqrt{mF_Q}} = \frac{1}{\sqrt{m}}, \tag{3.47}$$

which is the shot noise limit (SNL). The QFI formalism has therefore reproduced the Heisenberg limit and SNL. This implies an important result: earlier we found the Heisenberg limit and SNL by considering specific measurements, but now we are optimising over all possible measurements, which gives us the same results. Therefore, the number counting schemes above are *optimal* measurement schemes! This is often not the case in quantum metrology - we will see in this thesis that finding the optimal measurement can be a challenge - but for the NOON state, and the stream of single photons, no other measurement can improve upon the simple number counting Bayesian strategies.

We now look at the QFI for the entangled coherent state (ECS), for which the following identities are useful:

$$\sum_{n=0}^{\infty} \frac{n|\alpha|^{2n}}{n!} = |\alpha|^2 e^{|\alpha|^2}, \tag{3.48}$$

and

$$\sum_{n=0}^{\infty} \frac{n^2|\alpha|^{2n}}{n!} = (|\alpha|^4 + |\alpha|^2)e^{|\alpha|^2}. \tag{3.49}$$

We can then look at a general ECS, of which the ECS discussed in section 3.4 is a special case:

$$|\Psi\rangle = \mathcal{N}\left(|\alpha e^{i\phi}, 0\rangle + e^{i\theta}|0, \alpha\rangle\right) \tag{3.50}$$

Where $\mathcal{N} = (2(1 + e^{-|\alpha|^2}\cos\theta))^{-1/2}$. The Fisher information for this state is

$$F = 4|\alpha|^4(\mathcal{N}^2 - \mathcal{N}^4) + 4|\alpha|^2\mathcal{N}^2. \tag{3.51}$$

Using this we can study the performance of the ECS as compared to a NOON state, the results of which are shown in Fig. 3.4 for the ECS with $\theta = \pi/2$. The red line shows the QFI of the ECS, which is clearly significantly better than the NOON state for small α. We also see that our measurement scheme for the ECS, despite giving a better precision than NOON states, is not the optimal measurement scheme. As mentioned above, finding this optimal scheme is an ongoing challenge of our work!

3.7 How to count your resources

In this section we address a very important issue: how we count resources in quantum metrology. A lot of work has been done in recent years in establishing the ultimate precision bounds of quantum metrology (Demkowicz-Dobrzański *et al.*, 2012; Demkowicz-Dobrzanski *et al.*, 2014; Escher *et al.*, 2011; Kołodyński & Demkowicz-Dobrzański, 2013). These bounds have been derived by counting the *total number of particles used* as the relevant resource. For example, for the NOON state in section 3.2 above the total number of particles is the total number

inputting the interferometer. But is the total number of particles always the most relevant resource? This question is often neglected in the literature, but we feel it is a question of fundamental importance to the practical implementation of quantum metrology. We believe the answer is that how you count your resources depends on the specific needs of your experiment.

For example, when measuring fragile systems it is imperative that high precision is achieved from a limited number of probe particles passing *through the sample*. Examples of such fragile systems include spin ensembles (Wolfgramm *et al.*, 2013), biological systems (Carlton *et al.*, 2010; Taylor *et al.*, 2013), atoms (Eckert *et al.*, 2008; Tey *et al.*, 2008) and single molecules (Pototschnig *et al.*, 2011). In this regime it is of crucial importance to minimise the probe's interaction with the sample, otherwise the sample can be damaged, for example by scattering induced depolarisation in Wolfgramm *et al.* (2013), and direct damage to living cells, as is discussed in a recent review paper on quantum metrology in biology by Taylor & Bowen (2014) (and references therein). It is this fragile system regime, in which we count the number of particles through the phase as our resource, that we will concentrate on for the majority of this thesis.

However, this is not always the best way to count your resources. In gravitational wave (GW) interferometry, we are concerned with measuring phase shifts that are so small that very large lasers need to be used in the experiments. The immense power of these lasers (100s of W) is enough to disturb the mirrors in the interferometer by means of radiation pressure and mirror distortion due to heating (Punturo *et al.*, 2010; Purdy *et al.*, 2013). It is therefore crucial here that the *total number of particles* in the interferometer be kept to a minimum.

In the next chapter we will begin by looking at the work of Joo *et. al.* (Joo *et al.*, 2011) on using ECSs in quantum optical metrology. This work has been criticised in Demkowicz-Dobrzanski *et al.* (2014): they say that Joo *et. al.* go below the 'theoretical bounds' by not properly accounting for their resources. The central point to their arguement is that when using ECSs to make a phase measurement in a lossy system you need to introduce extra reference beams in your measurement scheme (we will show that this is indeed the case in the next chapter). They then comment that these extra reference beams are not accounted for and so the results of Joo *et. al.* are misleading. We will avoid a critique of this

sort by only considering the regime of fragile system sampling, and so counting the extra reference beams is not necessary.

Another important resource-related issue is how we can fairly compare different states, for example a NOON state and an ECS. In this work we will restrict the average number of particles through the phase shift to be R_ϕ. If we have a NOON state $(|N,0\rangle + i|0,N\rangle)/\sqrt{2}$ then each NOON state sends $\bar{n}_\phi = N/2$ particles through the phase shift. Therefore, we can repeat our experiment $m = R_\phi/\bar{n}_\phi$ times, which means the total number of particles sent through the phase is R_ϕ. For the majority of this thesis we will use this method to ensure that different states are compared fairly, and when other methods are used (for example when we consider spin systems) the resource counting procedure will be described. We often take $R_\phi = 400$ in our work: this number was chosen as it gives clear and efficient numerical results.

3.8 Chapter Conclusion

In this chapter we have laid out the basic concepts, and introduced a number of useful tools, in quantum metrology. We have used these tools to analyse a number of states in the decoherence free setting of optical interferometry. Next, we will begin to look at more realistic scenarios by introducing decoherence, in the form of photon losses, into our analysis.

Chapter 4

Entangled coherent state metrology with loss

Up to now we have been considering the idealised scenario of decoherence free optical interferometry. We will now begin to look at the more realistic case by introducing photon losses into our analysis. In the previous chapter we touched upon the idea that entangled coherent states (ECSs) may be more robust to losses than NOON states. Here we will address this idea more rigorously by analysing the effect of photon losses on these states. After looking at the loss mechanism itself, we will investigate whether an ECS can be used to measure a phase with sub-classical precision. To this regard we will introduce a novel measurement scheme that allows phase measurements close to the fundamental limit. We will then look at the QFI, which informs us of the best possible precision with which these states can measure a phase, before concluding the chapter with a simple method of pushing our precision measurements even further.

This chapter is based on the following papers: Knott & Dunningham (2014) and Knott *et al.* (2014b).

4.1 Can the annihilation operator represent loss?

We begin by looking at the annihilation operator: we would like to ask whether the annihilation operator can represent the loss of a photon to the environment. If the annihilation operator can represent loss, then this would give coherent states

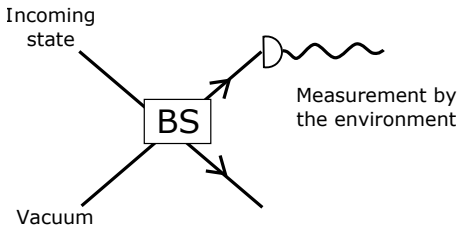

Figure 4.1: Fictional beam splitter to model loss.

a large advantage over the alternatives, because the effect of acting on a coherent state with the annihilation operator is

$$\hat{a}|\alpha\rangle = e^{-\frac{|\alpha|^2}{2}} \sum_{n=1}^{\infty} \frac{\alpha^n}{\sqrt{n!}} \sqrt{n}|n-1\rangle = \alpha|\alpha\rangle. \tag{4.1}$$

The coherent state is therefore left unchanged. But what does this actually mean? Can infinite numbers of photons be 'annihilated' and still leave the state unchanged?

An experiment by Zavatta *et al.* (2008) showed that annihilating a photon from a coherent state does indeed leave the state unchanged (Zavatta *et al.*, 2008). To do this a beam splitter followed by a photon measurement was used (Parigi *et al.*, 2007), as shown in Fig. 4.1. It is important here that the beam splitter has high transmissivity. To illustrate why this is important, we look at the beam splitter operation, defined as

$$\hat{U}_{BS} = e^{-\theta(\hat{a}^\dagger \hat{b} - \hat{b}^\dagger \hat{a})} \tag{4.2}$$

where $\eta = \cos^2\theta$ is the transmissivity of the beam splitter. For $\theta << 1$ we can use only the first order term in the Taylor expansion. If we then act this approximate beam splitter operation on an input state $|\psi\rangle$ we get

$$\hat{U}_{BS}|\psi, 0\rangle \approx \left(1 - \theta(\hat{a}^\dagger \hat{b} - \hat{b}^\dagger \hat{a})\right)|\psi, 0\rangle = |\psi, 0\rangle + \theta\hat{a}|\psi, 1\rangle \tag{4.3}$$

where $\hat{a}$ acts on the first mode, and $\hat{b}$ on the second. If we post-select the cases when we detect a photon in the second mode, we have applied the annihilation operator to the state. This illustrates that the annihilation operator is not a deterministic operator, but rather it is probabilistic.

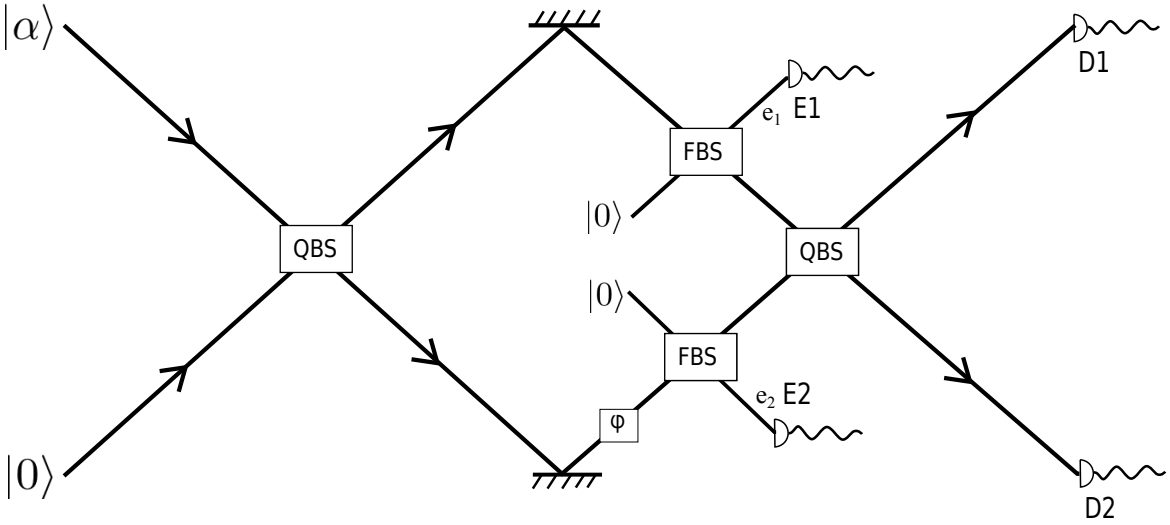

Figure 4.2: Here we see the addition of fictional beam splitters after the phase shift, which simulate loss.

We now show that the above scheme can't be used to remove arbitrary numbers of photons from a coherent state and leave it unchanged. If we consider two beam splitters, one after another, then the probability that we detect one photon from each beam splitter, and therefore the annihilation of two photons, will scale as θ^2. If we accept this two annihilation scenario, we must also look at the θ^2 terms in the beam splitter Taylor expansion, which contain terms that are not simply the annihilation operator. Therefore, removing two photons in this way would no longer leave the state unchanged! We can see now that when loss is small, we can use the annihilation operator to model loss. However, for larger losses, this formalism is not sufficient, and to analyse different states to be used for quantum metrology we need a formalism that can be used for arbitrary loss rates. Exactly how we do this will be discussed next.

4.2 Entangled coherent states with loss

We begin by looking at the scheme described in section 3.4, but with the inclusion of photon losses. To properly simulate the effects of loss we introduce 'fictional' beam splitters after the linear phase shift, which have probability of transmission

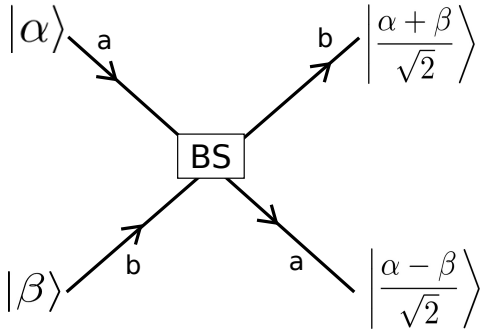

Figure 4.3: The effect of passing two coherent states through a beam splitter.

$\eta \equiv \cos^2\theta$, and therefore the proportion of photons that are lost is $\mu = 1 - \eta$ (Demkowicz-Dobrzanski *et al.*, 2009; Gkortsilas *et al.*, 2012; Joo *et al.*, 2011; Leonhardt & Paul, 1993). The whole scheme we are now considering is given in Fig. 4.2. After the phase shift, and including the vacuum states used to simulate loss, the ECS we are concerned with is given by

$$|\psi_0\rangle = \frac{1}{\sqrt{2}}\left[|\alpha e^{i\phi}, 0, 0, 0\rangle_{abcd} + i|0, 0, \alpha, 0\rangle_{abcd}\right], \tag{4.4}$$

where modes b and d are the added vacuum states before the 'fictional' beam splitters in Fig. 4.2. The next step requires the knowledge of how two coherent states (CSs) interact at a beam splitter. For the 50:50 BS we find

$$|\alpha, \beta\rangle_{a,b} \rightarrow \left|\frac{\alpha-\beta}{\sqrt{2}}, \frac{\alpha+\beta}{\sqrt{2}}\right\rangle_{a,b}, \tag{4.5}$$

which is demonstrated diagrammatically in Fig. 4.3. The effect of a variable BS, with transmission $\eta = \cos^2\theta$ and $\mu = 1 - \eta$, on the creation operators is:

$$\begin{aligned} a^\dagger &\rightarrow \sqrt{\eta}a^\dagger + \sqrt{\mu}b^\dagger \\ b^\dagger &\rightarrow \sqrt{\eta}b^\dagger - \sqrt{\mu}a^\dagger. \end{aligned} \tag{4.6}$$

From this we find that the effect of a variable BS on two CSs is

$$|\alpha, \beta\rangle_{a,b} \rightarrow |\alpha\sqrt{\eta} - \beta\sqrt{\mu}, \alpha\sqrt{\mu} + \beta\sqrt{\eta}\rangle_{a,b}. \tag{4.7}$$

Using this, we see that the effect of the 'fictional' beam splitters on $|\psi_0\rangle$ then leaves us in the state $|\Psi_1\rangle$, given by

$$|\Psi_1\rangle = \frac{1}{\sqrt{2}}\left[|\alpha e^{i\phi}\cos\theta, \alpha e^{i\phi}\sin\theta, 0, 0\rangle_{abcd} + i|0, 0, \alpha\cos\theta, \alpha\sin\theta\rangle_{abcd}\right] \tag{4.8}$$

where modes b and d are now the environmental modes, $e1$ and $e2$ respectively, which we will trace over to simulate a 'measurement' by the environment. To do this we take the density matrix $\rho_1 = |\psi_1\rangle\langle\psi_1|$, and trace over the environmental modes as follows:

$$\rho_2 = \sum_{e_1}\sum_{e_2}\langle e_1|\langle e_2|\rho_1|e_2\rangle|e_1\rangle. \tag{4.9}$$

Using $\sum_e \langle e|X\rangle\langle Y|e\rangle = \langle Y|X\rangle$, and the nonorthogonality of coherent states, $\langle\alpha|\beta\rangle = \exp\left(-\frac{1}{2}|\alpha|^2 + \alpha^*\beta - \frac{1}{2}|\beta|^2\right)$, it can be shown that ρ_2 is reduced to

$$\rho_2 = c_1\left(|\psi_2\rangle\langle\psi_2|\right) + \frac{1}{2}c_2\left(|\alpha e^{i\phi}\sqrt{\eta}, 0\rangle\langle\alpha e^{i\phi}\sqrt{\eta}, 0| + |0, \alpha\sqrt{\eta}\rangle\langle 0, \alpha\sqrt{\eta}|\right) \tag{4.10}$$

where $c_1 = e^{|\alpha|^2(\eta-1)}$, $c_2 = 1 - c_1$ and

$$|\psi_2\rangle = \frac{1}{\sqrt{2}}\left[|\alpha e^{i\phi}\sqrt{\eta}, 0\rangle + i|0, \alpha\sqrt{\eta}\rangle\right]. \tag{4.11}$$

We see here that the resulting state is a mixture of loss and no loss components. With probability c_1 we still have the pure ECS, albeit with a smaller amplitude, $\alpha\sqrt{\eta}$, which we can use to determine the phase ϕ. With probability $c_2/2$ we have the state $|0, \alpha\sqrt{\eta}\rangle$, which cannot give us any information about the phase shift. Finally, also with probability $c_2/2$, we have the state $|\alpha e^{i\phi}\sqrt{\eta}, 0\rangle$, and in this case the phase is present, and so in principle it can be measured.

Next, we pass ρ_2 through the final QBS, count the photon numbers at the detectors, and then implement the Bayesian procedure used in section 3.1 to determine the phase, ϕ, and the precision with which it can be measured, $\delta\phi$. The results are shown in Fig. 4.4. We see that whilst the ECS (purple crossed line) starts off with better precision than the NOON state (blue dashed line) and the SNL (black dashed dotted line), as the loss increases soon the ECS rapidly loses its precision. It is interesting to note that the ECS is more fragile (i.e. more affected by loss) than the NOON state in this scheme. The reason for

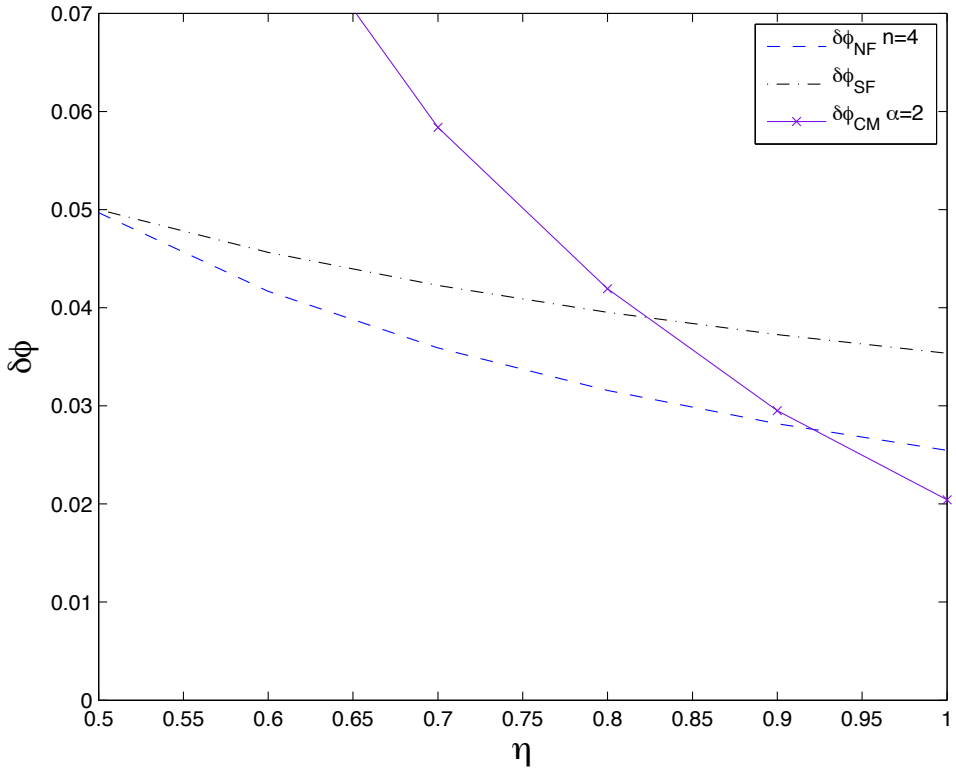

Figure 4.4: Here $\delta\phi_{CM}$ is the ECS using the simple measurement scheme in Fig. 4.2, $\delta\phi_{NF}$ is the NOON state (of equivalent size as each ECS) and $\delta\phi_{SF}$ is the SNL. We can see that ECSs degrade quickly with loss. Here $\alpha = \sqrt{2}$, and for larger α the ECS loses precision with loss even quicker.

this is that for NOON states we know during each run if there has been loss simply by counting the numbers of photons at the outputs. If no photons are lost, our Bayesian scheme utilises the pure NOON state to determine the phase to a high precision. However, for ECSs we can no longer do this, as we don't know the number of photons in an ECS to begin with, and therefore the number counting measurement gives us minimal information about the final state that we are detecting. The results in Fig. 4.4 are for a very small ECS of $\alpha = \sqrt{2}$. Larger ECSs are even more fragile with loss (see the green line in Fig. 4.11), and therefore we clearly need a more effective scheme to measure a phase using an ECS.

4.3 Improved scheme for measuring the ECS with loss

Despite the fact that an entangled coherent state can still retain some phase information after loss, we have seen that with a simple measurement scheme the phase information cannot be recovered, and we end up doing even worse than NOON states. We have devised a scheme, shown in Fig. 4.5, which can be used to recover this desired phase information. The key is to use extra 'reference' coherent states, α_1, above and below the main interferometer, which can be used to perform a homodyne measurement and recover the phase information from the collapsed state $|\alpha e^{i\phi}, 0\rangle$.

The state in this 'long arm' interferometer after the phase shift is

$$\begin{aligned} |\Psi_1\rangle &= \frac{1}{\sqrt{2}}\left(|\alpha_1, \alpha_0 e^{i\phi}, 0, \alpha_1\rangle + i|\alpha_1, 0, \alpha_0, \alpha_1\rangle\right) \\ &= |\Phi_1\rangle + |\Phi_2\rangle. \end{aligned} \tag{4.12}$$

After being acted on by the fictional beam splitters that simulate loss, this state is transformed from $|\Psi_1\rangle$ to $|\Psi_2\rangle$. We then trace over the environmental degrees of freedom to give $\rho = \sum_e \langle e|\Psi_2\rangle\langle\Psi_2|e\rangle$ where $|e\rangle$ represents all four environmental modes. This gives us

$$\rho = |\Phi_{1\eta}\rangle\langle\Phi_{1\eta}| + |\Phi_{2\eta}\rangle\langle\Phi_{2\eta}| + e^{-|\alpha_{0\mu}|^2}\left(|\Phi_{1\eta}\rangle\langle\Phi_{2\eta}| + |\Phi_{2\eta}\rangle\langle\Phi_{1\eta}|\right), \tag{4.13}$$

where $|\Phi_{1\eta}\rangle = \frac{1}{\sqrt{2}}|\alpha_{1\eta}, \alpha_{0\eta}e^{i\phi}, 0, \alpha_{1\eta}\rangle$, $|\Phi_{2\eta}\rangle = \frac{i}{\sqrt{2}}|\alpha_{1\eta}, 0, \alpha_{0\eta}, \alpha_{1\eta}\rangle$, $\alpha_{0\eta} = \alpha_0\sqrt{\eta}$, $\alpha_{1\eta} = \alpha_1\sqrt{\eta}$, $\alpha_{0\mu} = \alpha_0\sqrt{1-\eta}$ and η is the transmission rate through the interferometer. We then send ρ through the final beam splitters, which results in the state $\bar{\rho}$. The probability of detecting k photons at detector $D1$, l at $D2$, m at $D3$, and n at $D4$ is

$$P_{klmn} = \langle k, l, m, n|\bar{\rho}|k, l, m, n\rangle. \tag{4.14}$$

Using this we can again use the Bayesian scheme that was described in section 3.1 to determine the phase ϕ, and the precision, $\delta\phi$.

Optimising over ϕ and α_1, we obtain the results in Fig. 4.6 for $\alpha_0 = \sqrt{2}$. It can be seen that our state now outperforms the NOON and SP states for all values

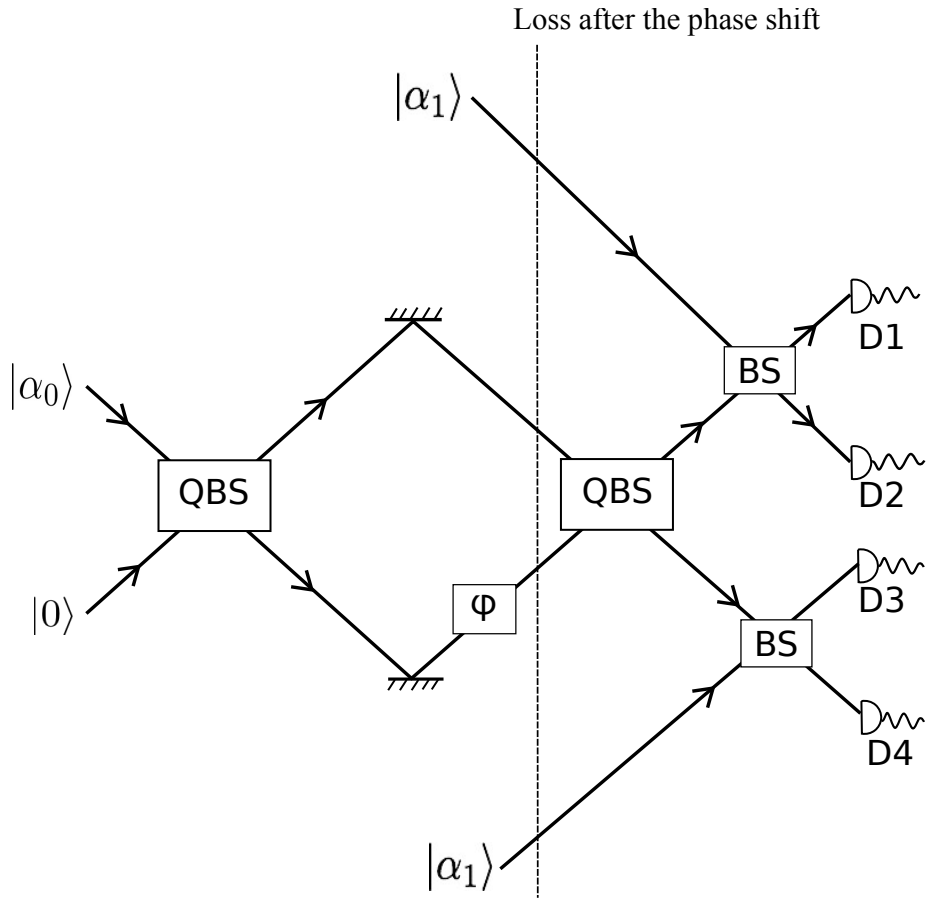

Figure 4.5: Quantum interferometer with extra arms to recover phase information with loss.

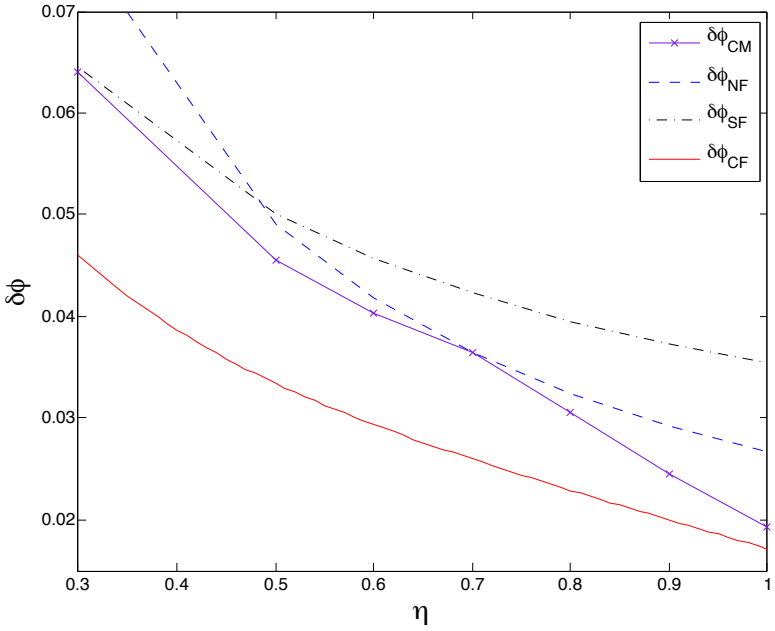

Figure 4.6: Here we see the precision obtained by an ECS in the scheme in Fig. 4.5 for $\alpha_0 = \sqrt{2}$. We measure at a higher precision than NOON and SP for all loss rates shown.

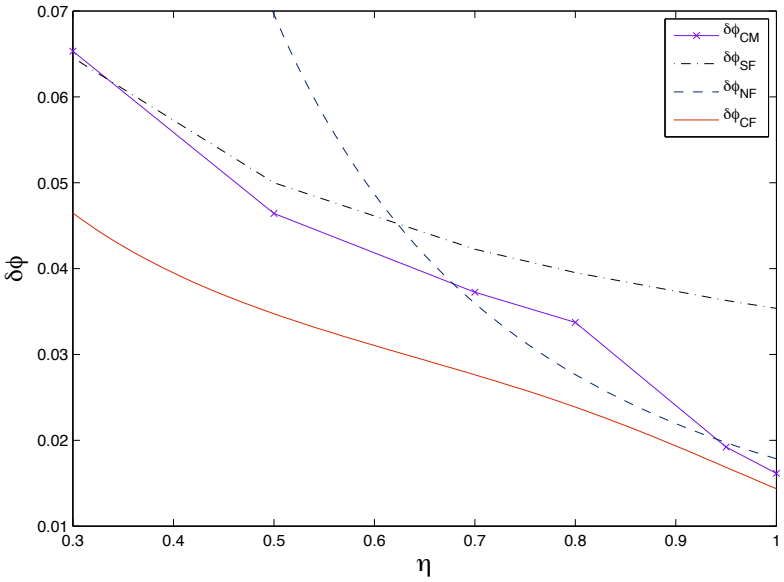

Figure 4.7: Here $\alpha_0 = 2$ for an ECS in Fig. 4.5. Our scheme improves over the NOON and SP states for most loss values.

of loss on the range shown. Figs. 4.7 and 4.8 show the results for $\alpha_0 = 2$ and $\alpha_0 = 5$, respectively, illustrating that for larger values of α_0 our scheme (purple crossed line) still obtains higher precision than the alternatives for the majority of loss rates.

The red lines in Figs. 4.6, 4.7 and 4.8 show the QFI for the ECS: how these are derived will be explained in section 4.5. Despite our positive results, there is a large practical downside to this scheme: it uses quantum beam splitters, which are difficult to make in practice. In the next section we will show how we can do without these and still obtain good results.

4.4 Scheme without a quantum beam splitter

Whilst the above scheme achieves sub shot noise precision even with loss, it is admittedly hard to implement. The main difficulty lies in the QBS: this involves a nonlinearity (Dunningham & Kim, 2006), which is no simple task to perform (as we saw in section 3.3). In order to make the scheme more experimentally accessible we would like to consider whether we can eliminate the QBSs all to-

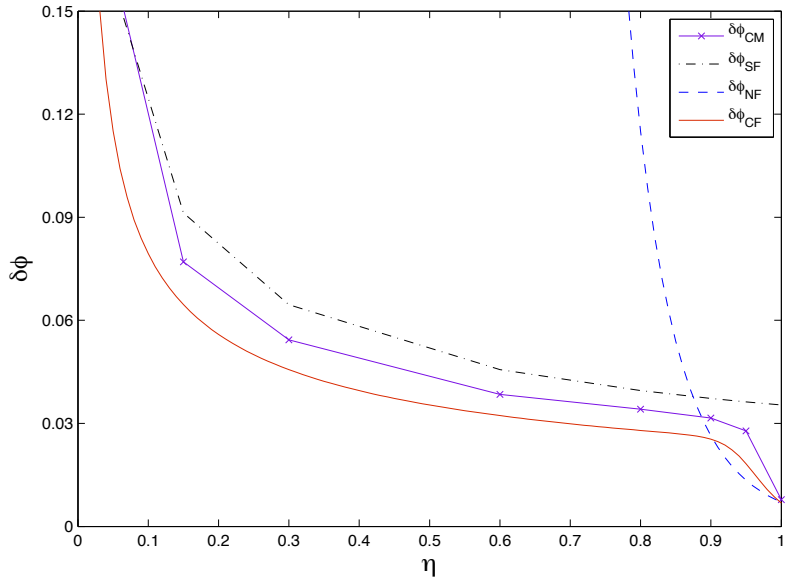

Figure 4.8: Here $\alpha_0 = 5$ for an ECS in Fig. 4.5. Again for most loss rates we perform better than NOON and SP states.

gether. The general interferometer we now consider is shown in Fig. 4.9. We take the first input state to be a cat state[1] $|\gamma_1\rangle = \mathcal{N}_1(|\alpha_0/\sqrt{2}\rangle + |-\alpha_0/\sqrt{2}\rangle)$, where $\mathcal{N}_1 = 1/\sqrt{2(1+e^{-|\alpha_0|^2})}$. Mixing $|\gamma_1\rangle$ with $|\alpha_i\rangle = |\alpha_0/\sqrt{2}\rangle$ at a 50:50 beam splitter, using equation (4.5), gives

$$|\alpha_i\rangle|\gamma_1\rangle = \mathcal{N}_1|\alpha_0/\sqrt{2}\rangle\left(|\alpha_0/\sqrt{2}\rangle + |-\alpha_0/\sqrt{2}\rangle\right) \longrightarrow \mathcal{N}_1(|\alpha_0, 0\rangle + |0, \alpha_0\rangle. \quad (4.15)$$

Hence we have created an ECS without using a QBS; but we still need to make the cat state. There are many examples of cat state generation techniques, such as that given in Brune *et al.* (1996). In this scheme a Rydberg atom in a cavity in the state $|g\rangle + |e\rangle$ is coupled to a coherent state via the Jaynes-Cummings Hamiltonian (Jaynes & Cummings, 1963). The atom-cavity system evolves as $|\alpha'\rangle(|g\rangle + |e\rangle) \rightarrow |\alpha'\rangle|g\rangle + |\alpha' e^{i\theta}\rangle|e\rangle$ and, after a transformation and measurement of the Rydberg atom and taking $\theta = \pi$, the resultant state of the field is a cat state. Alternative schemes are numerous (Bartley *et al.*, 2012; Gerrits *et al.*, 2010; Gerry & Knight, 1997; Leghtas *et al.*, 2013; Lund *et al.*, 2004), and cat

[1]This is called a cat state because it is a superposition of two distinct 'classical' coherent states.

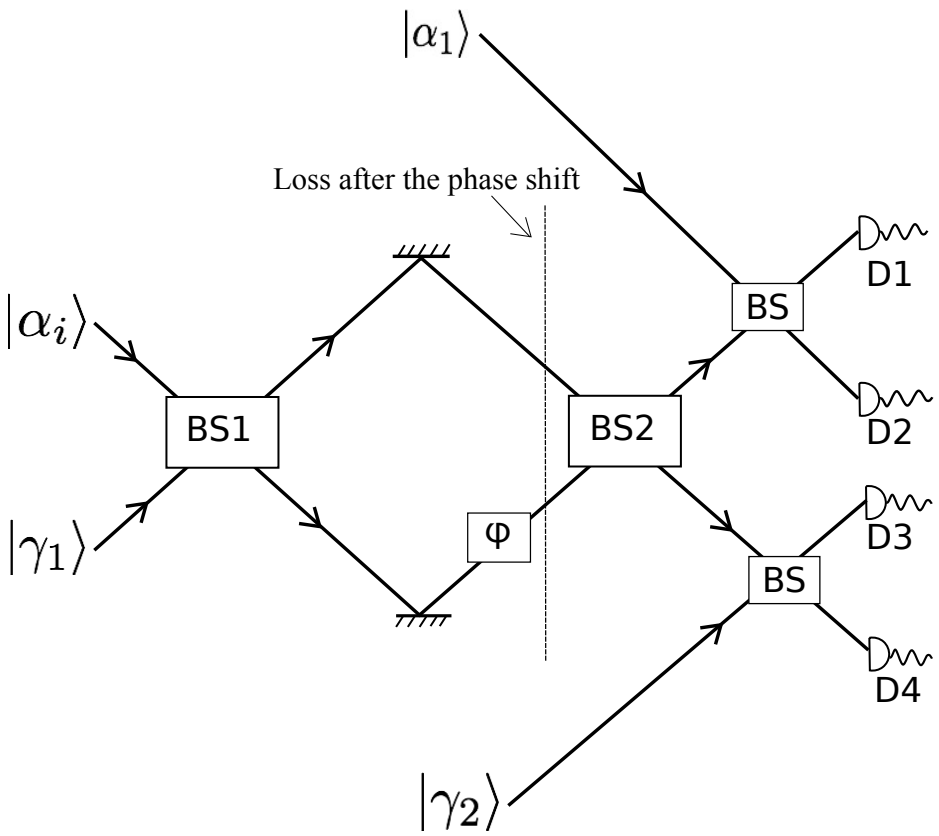

Figure 4.9: Quantum interferometer with extra arms, but without the QBSs, used to recover phase information with loss.

states have been created with $\alpha' = 1.76$ and fidelity 0.59 in the lab (Gerrits *et al.*, 2010). Schemes for creating cat states also require a non linearity of some sort, but unlike the QBS the cat state is created offline, whereas previously it was necessary to implement the QBS within the interferometer. In principle we could have an interferometer that waits for a cat state to be correctly created, and then inputs it into the interferometer. If there is a problem then there is no input, and therefore no state will be sent through the phase.

We still need to eliminate the QBS after the phase shift at BS2. If we send the ECS $\approx |\alpha, 0\rangle + |0, \alpha\rangle$ through a phase shift, and then through a beam splitter, just like in an ordinary Mach-Zehnder interferometer, then without loss we can still obtain sub shot noise limit precision. In fact the precision is almost identical to using a QBS. The probability of detecting m photons in the upper output is

approximately given by

$$P(m,n) \approx \begin{cases} \cos^2 \frac{\phi(m+n)}{2} & \text{for } n \text{ even} \\ \\ \sin^2 \frac{\phi(m+n)}{2} & \text{for } n \text{ odd.} \end{cases} \tag{4.16}$$

We therefore must know if the bottom output is even or odd in order to determine the phase. This is important because when we introduce loss we need upper and lower reference states in order to determine the phase. If we take $|\gamma_2\rangle = |\alpha_1\rangle$ in Fig. 4.9 then we no longer know whether we had even or odd numbers, and the phase information provided by the entangled state therefore washes out and we no longer get quantum enhancement (we can still measure the phase, but at the shot noise limit at best). We therefore take $|\gamma_2\rangle = \mathcal{N}_2(|\alpha_1\rangle + |-\alpha_1\rangle)$ where $\mathcal{N}_2 = 1/\sqrt{2(1+e^{-2|\alpha_1|^2})}$, which always contains an even number of photons, and therefore allows us to retain quantum enhancement. Using this scheme, which now contains two cat states but no QBSs, we are able to achieve very similar results to when we used a QBS.

After optimising over α_1 and ϕ for different loss rates we then obtain the results in Fig. 4.10 for $\alpha_0 = 1.1307$ (which has an average photon number of 1). It can be seen that our state now outperforms the NOON and unentangled states for all values of loss up to 53%, i.e. $\eta = 0.47$. The significant precision enhancement for small α_0 is evident here, as well as the robustness to loss. Fig. 4.11 then shows the results for the larger amplitude ECS of $\alpha_0 = 4$. We can see that for $\alpha_0 = 4$ our scheme (purple crossed line) still beats the NOON state (blue dashed line) and the unentangled state (black dashed dotted line) for the majority of η values.

We have seen that the ECS can be used to make precise phase measurements using the interferometer in Fig. 4.9. Furthermore, this scheme is robust to loss and can be experimentally implemented. The question remains as to how close our scheme comes to the fundamental limit that an ECS can obtain, and it is this question that we turn to in the next section.

4.5 QFI of the ECS

We would now like to determine the best possible precision with which this state can measure the phase shift ϕ. In order to do this, we will use the QFI and

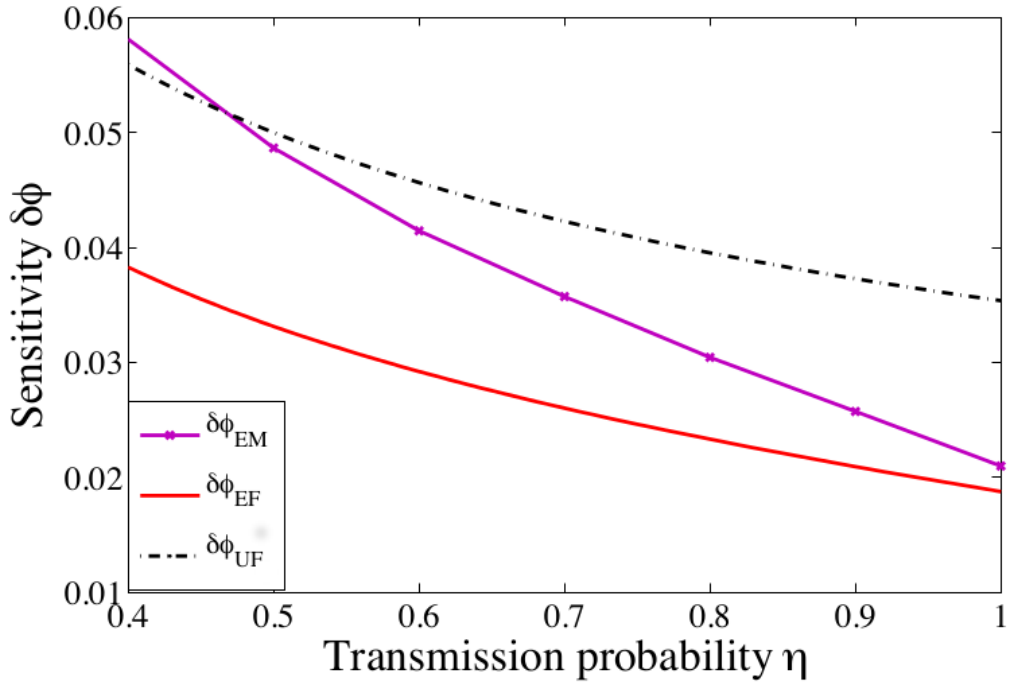

Figure 4.10: The measurable phase precision for ECSs with amplitudes $\alpha_0 = 1.1307$ (which has an average photon number of 1) using our measurement scheme is shown by the purple crossed line $\delta\phi_{EM}$. The red solid and black dotted-dashed lines give the QFI of the ECS $\delta\phi_{EF}$ and unentangled states $\delta\phi_{UF}$, respectively, all of equivalent size: $N = 2\mathcal{N}_1^2|\alpha_0|^2$ (therefore the NOON and unentangled states are equal here). Here, for small α_0, our scheme provides the best phase precision for the majority of loss rates.

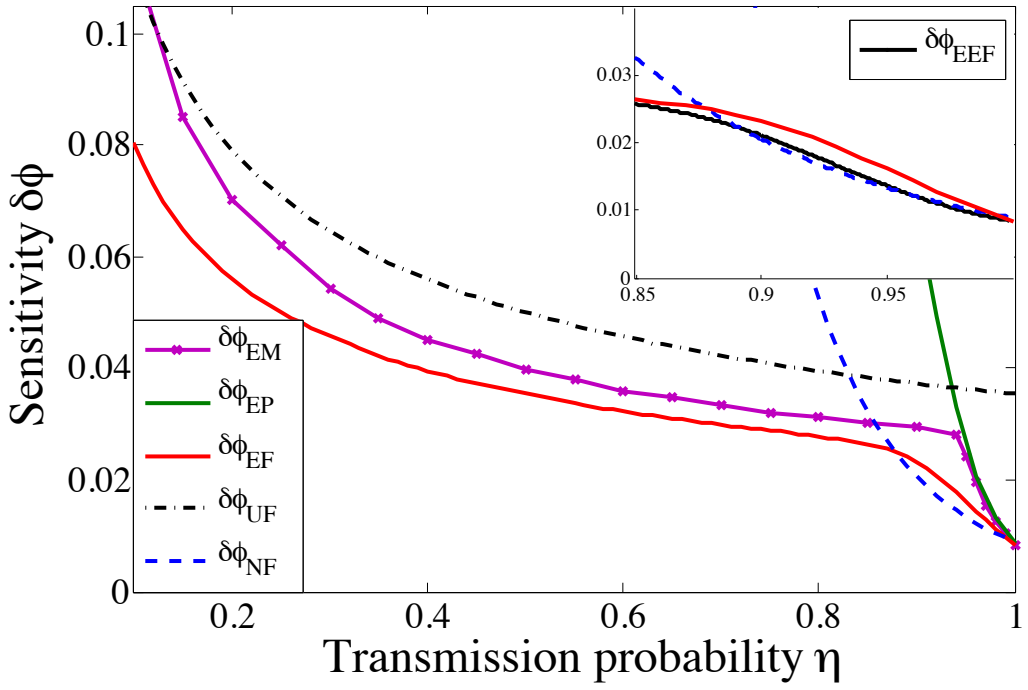

Figure 4.11: The measurable phase precision for ECSs with amplitude $\alpha_0 = 4$ using our measurement scheme is shown by the purple crossed line $\delta\phi_{EM}$. The legend is the same as in Fig. 4.10, with the addition of the dark green solid line, which shows the measurement of the ECS without the extra arms $\delta\phi_{EP}$, and the blue dashed line, which shows the NOON state $\delta\phi_{NF}$. Here we see that for large α_0 our scheme provides the best phase precision for the majority of loss rates, and we come close to saturating the QFI. The black solid line in the inset shows the QFI of the even ECS described in section 4.6, demonstrating how we can obtain a higher precision than the NOON states for most loss rates simply by modifying our input state.

QCRB, as described in the previous chapter. To find the QFI we will follow the work of Zhang *et al.* (2013), who derived a general formula for the QFI of a mixed state $\rho = \sum_i \lambda_i |\lambda_i\rangle\langle\lambda_i|$, where $\{|\lambda_i\rangle\}$ forms a complete orthonormal basis. The QFI is given by equation (3.36), which we re-state here for clarity:

$$F_Q = \sum_{i,j} \frac{2}{\lambda_i + \lambda_j} |\langle\lambda_i|\rho'|\lambda_j\rangle|^2 \tag{4.17}$$

where $\rho' = \partial\rho/\partial\phi$. As stated above, this formula for the QFI involves writing ρ in its eigenbasis $\{|\lambda_i\rangle\}$. Performing this step is often the stumbling point in analytically calculating the QFI of a mixed state. For small system sizes it is often possible to numerically diagonalise ρ, but this severely restricts the results to states which are often too small to be useful. Nevertheless, finding the QFI of a state numerically can reveal important features of a state, and this was done for the ECS by Joo *et al.* (2011).

However, for the ECS it is in fact possible to derive the QFI analytically, as was done by Zhang *et al.* (2013). They begin with equation (4.17), and then show that often only a small subset $\{|\lambda_i\rangle\}$ has nonzero weights, which allows the QFI to be written as:

$$F_Q = \sum_i \frac{(\lambda_i')^2}{\lambda_i} + \sum_i \lambda_i F_{Q,i} - \sum_{i\neq j} \frac{8\lambda_i\lambda_j}{\lambda_i + \lambda_j} |\langle\lambda_i'|\lambda_j\rangle|^2, \tag{4.18}$$

where $F_{Q,i} = 4[\langle\lambda_i'|\lambda_i'\rangle - |\langle\lambda_i'|\lambda_i\rangle|^2]$ (this is the QFI of a pure state $|\lambda_i\rangle$). We find that the first term, which is the classical Fisher information of the probability distribution $P(i|\phi) = \lambda_i(\phi)$, is zero.

We will now find the QFI for the ECS $|\Psi_1\rangle = \mathcal{N}(|\alpha e^{i\phi}, 0\rangle + |0, \alpha\rangle)$. We have seen that after loss this state becomes the mixed state

$$\rho = c_1 \left(|\psi_2\rangle\langle\psi_2|\right) + \mathcal{N}^2 c_2 \left(|\alpha_\eta e^{i\phi}, 0\rangle\langle\alpha_\eta e^{i\phi}, 0| + |0, \alpha_\eta\rangle\langle 0, \alpha_\eta|\right) \tag{4.19}$$

where $\alpha_\eta = \alpha\sqrt{\eta}$, $c_1 = e^{-\alpha_\mu^2} = e^{-|\alpha|^2\mu} = e^{|\alpha|^2(\eta-1)}$, $c_2 = 1 - c_1$ and

$$|\psi_2\rangle = \mathcal{N}\left[|\alpha_\eta e^{i\phi}, 0\rangle + i|0, \alpha_\eta\rangle\right]. \tag{4.20}$$

As the QFI calculation requires ρ in its basis we rewrite this as

$$\rho = \mathcal{N}^2 \left(|\alpha_\eta e^{i\phi}, 0\rangle\langle\alpha_\eta e^{i\phi}, 0| + |0, \alpha_\eta\rangle\langle 0, \alpha_\eta| + e^{-\alpha_\mu^2} \left[|0, \alpha_\eta\rangle\langle\alpha_\eta e^{i\phi}, 0| + |\alpha_\eta e^{i\phi}, 0\rangle\langle|0, \alpha_\eta\right] \right). \tag{4.21}$$

As ρ in now written only in terms of $|\alpha_\eta e^{i\phi}, 0\rangle$ and $|0, \alpha_\eta\rangle$, we can write the eigenvectors as:

$$|\lambda_\pm\rangle = N_\pm(|\alpha_\eta e^{i\phi}, 0\rangle \pm |0, \alpha_\eta\rangle) \tag{4.22}$$

where $N_\pm = 1/\sqrt{2(1 \pm e^{-\alpha_\mu^2})}$. We can then find the eigenvalues with the equation $\rho|\lambda_\pm\rangle = \lambda_\pm|\lambda_\pm\rangle$. This can be confirmed by showing that $\rho = \lambda_+|\lambda_+\rangle\langle\lambda_+| + \lambda_-|\lambda_-\rangle\langle\lambda_-|$, $\lambda_+ + \lambda_- = 1$ and $\langle\lambda_i|\lambda_j\rangle = \delta_{ij}$. We then find the eigenvalues to be

$$\lambda_\pm = \mathcal{N}^2(1 \pm e^{-\alpha_\eta^2})(1 \pm e^{-\alpha_\mu^2}). \tag{4.23}$$

The further terms we need are: $\langle\lambda_\pm|\lambda'_\pm\rangle = iN_\pm^2|\alpha_\eta|^2$, $\langle\lambda_\mp|\lambda'_\pm\rangle = iN_+N_-|\alpha_\eta|^2$ and $\langle\lambda'_\pm|\lambda'_\pm\rangle = N_\pm^2|\alpha_\eta|^2(1 + |\alpha_\eta|^2)$. These allow us to calculate

$$\begin{aligned}\sum_{i=\pm} \lambda_i F_{Q,i} = {} & 4\lambda_+ N_+^2|\alpha_\eta|^2(1 + |\alpha_\eta|^2 - N_+^2|\alpha_\eta|^2) \\ & + 4\lambda_- N_-^2|\alpha_\eta|^2(1 + |\alpha_\eta|^2 - N_-^2|\alpha_\eta|^2)\end{aligned} \tag{4.24}$$

and

$$\sum_{i=\pm, j=\mp} \frac{8\lambda_i\lambda_j}{\lambda_i + \lambda_j}|\langle\lambda'_i|\lambda_j\rangle|^2 = 16\lambda_+\lambda_- N_+^2 N_-^2|\alpha_\eta|^4. \tag{4.25}$$

From the QFI we can find the theoretical upper bound on attainable precision, the QCRB, given by: $\delta\phi = 1/\sqrt{mF_Q}$, with m the number of classical repeats of the experiment. Our results for the QCRB of the ECS are shown as the red curves on Figs. 4.6-4.8 and Figs. 4.10-4.11.

We can see from Figs. 4.10 and 4.11 that the measurement scheme presented in section 4.4 comes reasonably close to the theoretical lower bound. This means that more improvements to the scheme are in theory possible, but despite this we

can see that we do well enough to beat the NOON state and SNL for most loss rates. We come closer to saturating the bound for the larger state $\alpha_0 = 4$ in 4.11, but here there is a small region where the NOON state obtains a higher precision than the ECS. This agrees with the results of Zhang *et. al.* who showed that: "although the classical term of the ECS is robust against the photon losses, the Heisenberg term decays about twice as quick as that of the NOON state" (Zhang *et al.*, 2013). We will show in the next section that, with a slight modification of the input states, we can overcome this problem.

4.6 Even entangled coherent states

We now show how our scheme can be improved further to overcome the rapid initial loss of coherence which results in our state losing out to the NOON state in the small loss regime. If we change our upper input state $|\alpha_i\rangle$ in Fig. 4.9 to another cat state, $|\gamma_1\rangle = \mathcal{N}_1(|\alpha_0/\sqrt{2}\rangle + |-\alpha_0/\sqrt{2}\rangle)$, then after the first beam splitter we will have an ECS that only contains even numbers of photons, which we call an even entangled coherent state (EECS)

$$\begin{aligned} |\Psi\rangle_{EECS} &= \mathcal{N}_1^2\left(|\alpha_0, 0\rangle + |0, \alpha_0\rangle + |-\alpha_0, 0\rangle + |0, -\alpha_0\rangle\right) \\ &= \mathcal{N}_1^2\left(|e, 0\rangle + |0, e\rangle\right). \end{aligned} \tag{4.26}$$

Here we have written the (unnormalised) even cat state as $|e\rangle = |even\rangle = (|\alpha_0\rangle + |-\alpha_0\rangle)$. If this state is written in the number basis $|n\rangle$ then the odd photon number terms all cancel, hence the name 'even' cat state. This state may be advantageous as now we have some idea of whether there is loss or not on each run. If we detect an odd number of photons, then we know that there has been at least one photon lost. We only gain a small advantage, as we still don't know exactly how many photons are lost, and when we detect even numbers then we learn nothing. However, this small advantage in knowledge acquisition is enough to give a significant precision improvement for low loss.

The QFI for this even ECS is shown in the inset of Fig. 4.11: we now only marginally lose to the NOON state, in a very small region. The results for the EECS can be seen more clearly in Fig. 4.12 and Fig. 4.13. Here we see that for the

larger α values the EECS is advantageous, but for smaller α the ECS is preferable. These results show that we can now tailor our input states for different loss values to produce a scheme that achieves higher precision than NOON states and unentangled states for the vast majority of loss rates, including the experimentally relevant rates which can be up to a few times 10%, e.g. $\eta = 0.62$ in Demkowicz-Dobrzański *et al.* (2013).

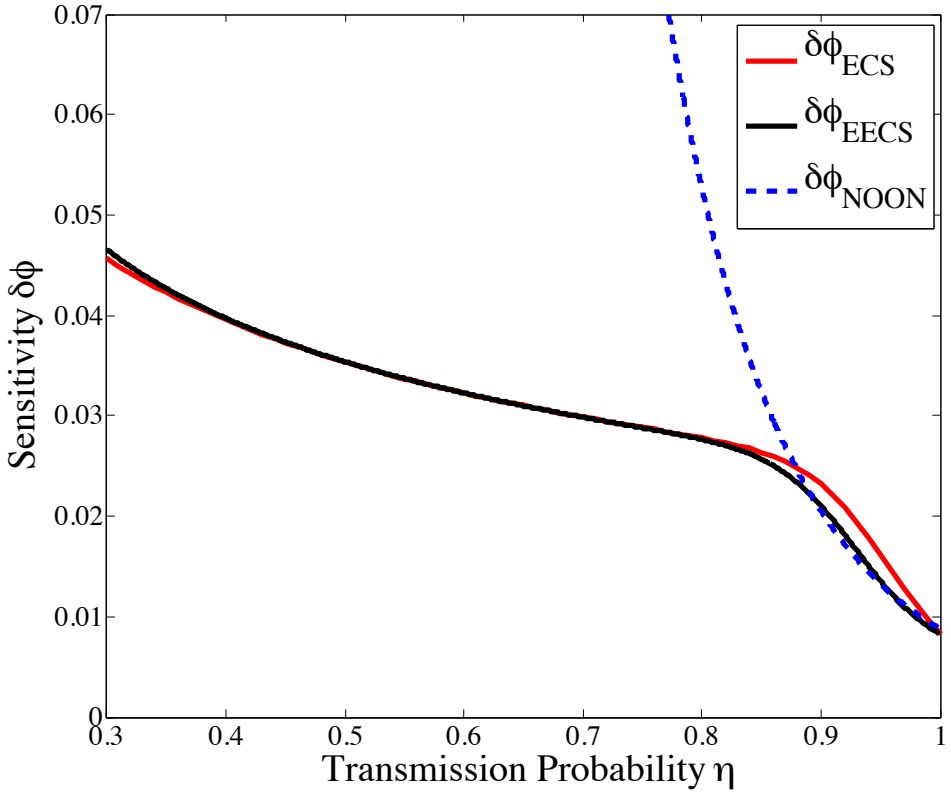

Figure 4.12: Here we see the EECS against the ECS and the NOON for $\alpha_0 = 4$. With the EECS we now come very close to the NOON state when previously we had been clearly beaten.

For brevity we will not show the full QFI calculation for the EECS here, but it is interesting to discuss the idea behind deriving the QFI analytically for the EECS. To calculate the QFI we first, as always, have to diagonalise the density matrix after loss in order to find the eigenvalues and eigenvectors. The density

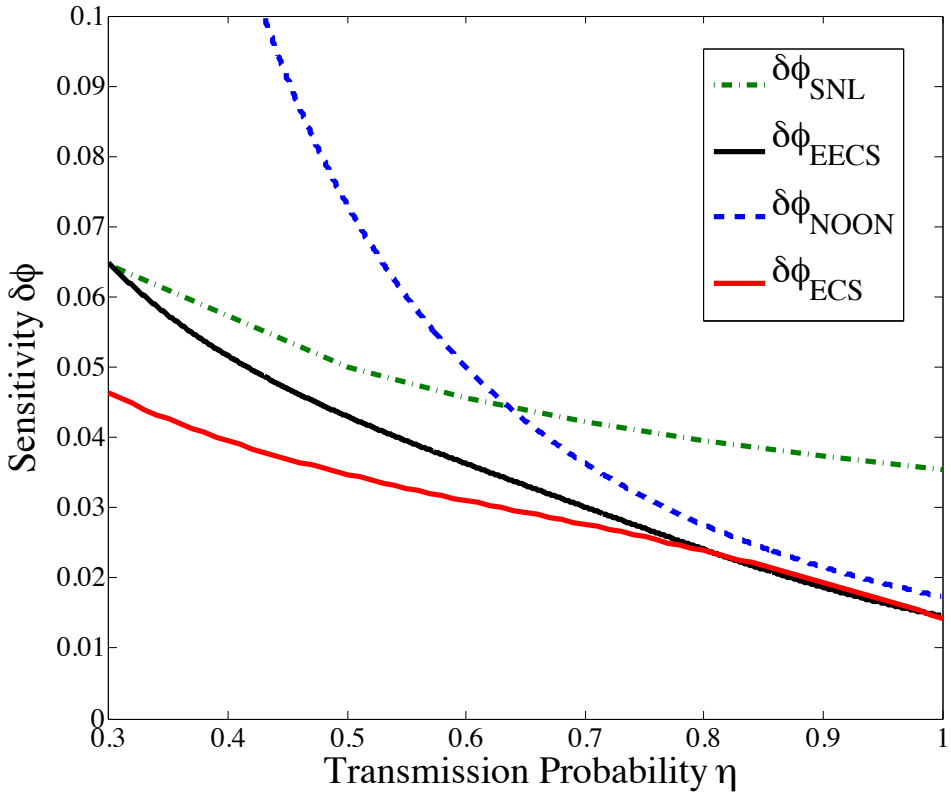

Figure 4.13: Here we see the EECS against the ECS, the NOON and the SNL for $\alpha_0 = 2$. We see that whilst the EECS is advantageous for larger α, here the ECS is actually the better choice for high precision.

matrix after loss is given by

$$\rho = \mathcal{N}_1^2 \left(|\alpha_\eta^\phi, 0\rangle\langle\alpha_\eta^\phi, 0| + |-\alpha_\eta^\phi, 0\rangle\langle-\alpha_\eta^\phi, 0| + |0, \alpha_\eta\rangle\langle 0, \alpha_\eta| + |0, -\alpha_\eta\rangle\langle 0, -\alpha_\eta| \right.$$
$$+e^{-2\alpha_\mu^2} \left[|\alpha_\eta^\phi, 0\rangle\langle-\alpha_\eta^\phi, 0| + |-\alpha_\eta^\phi, 0\rangle\langle\alpha_\eta^\phi, 0| + |0, \alpha_\eta\rangle\langle 0, -\alpha_\eta| + |0, -\alpha_\eta\rangle\langle 0, \alpha_\eta| \right]$$
$$\left. +e^{-\alpha_\mu^2} \left[(|\alpha_\eta^\phi, 0\rangle + |-\alpha_\eta^\phi, 0\rangle)(\langle 0, \alpha_\eta| + \langle 0, -\alpha_\eta|) + (|0, \alpha_\eta\rangle + |0, -\alpha_\eta\rangle)(\langle\alpha_\eta^\phi, 0| + \langle-\alpha_\eta^\phi, 0|) \right] \right).$$

where $|\alpha_\eta^\phi\rangle = |\alpha_0\sqrt{\eta}e^{i\phi}\rangle$. This density matrix looks difficult to diagonalise at first

sight, but we can use the following identities:

$$\begin{aligned}
&|\alpha\rangle\langle\alpha| + |-\alpha\rangle\langle-\alpha| = \frac{1}{2}|(|e\rangle\langle e| + |d\rangle\langle d|), \\
&|\alpha\rangle\langle-\alpha| + |-\alpha\rangle\langle\alpha| = \frac{1}{2}|(|e\rangle\langle e| - |d\rangle\langle d|), \\
&|e,0\rangle\langle e,0| + |0,e\rangle\langle 0,e| + (2\sigma-1)\left(|0,e\rangle\langle e,0| + |e,0\rangle\langle 0,e|\right) \\
&= \sigma|e,0+0,e\rangle\langle e,0+0,e| + (1-\sigma)|e,0-0,e\rangle\langle e,0-0,e|,
\end{aligned} \tag{4.27}$$

where σ is a constant. Here $|e,0+0,e\rangle = |e,0\rangle + |0,e\rangle$, and $|d\rangle = |odd\rangle = (|\alpha\rangle - |-\alpha\rangle)$ is the odd cat state (which only contains odd numbers of photons due to cancellation of the even terms). Using these identities we are able to diagonalise the density matrix as

$$\begin{aligned}
\rho = \frac{\mathcal{N}_1^2}{2}\Big[&(1+e^{-2\alpha_\mu^2})\left(\sigma|e,0+0,e\rangle\langle e,0+0,e| + (1-\sigma)|e,0-0,e\rangle\langle e,0-0,e|\right) \\
&+(1-e^{-2\alpha_\mu^2})\left(|d,0\rangle\langle d,0| + |0,d\rangle\langle 0,d|\right)\Big]
\end{aligned} \tag{4.28}$$

where we find σ from

$$2\sigma - 1 = \frac{2e^{-\alpha_\mu^2}}{1+e^{-2\alpha_\mu^2}}. \tag{4.29}$$

From this we can see that the eigenvectors are

$$\begin{aligned}
|\lambda_1\rangle &\propto |e,0+0,e\rangle \\
|\lambda_2\rangle &\propto |e,0-0,e\rangle \\
|\lambda_3\rangle &\propto |d,0\rangle \\
|\lambda_4\rangle &\propto |0,d\rangle.
\end{aligned} \tag{4.30}$$

The proportionality constants and the eigenvalues can then be found, which allows us to calculate the QFI as before, using equation 4.17, to give the results for the EECS in Fig. 4.12 and Fig. 4.13.

4.7 Chapter Conclusion

We have seen in this chapter that ECSs are robust states for optical quantum metrology. Next we will investigate if, by questioning the importance of multi-

mode entanglement in our schemes, we can make significant precision improvements over the ECS and the alternative states.

Chapter 5

Do we need multi-mode entanglement in optical quantum metrology?

5.1 Do we need multi-mode entanglement?

The precision gains offered by quantum metrology are often attributed to entanglement (Afek *et al.*, 2010; Cappellaro *et al.*, 2005; Giovannetti *et al.*, 2006; Lee *et al.*, 2002; Riedel *et al.*, 2010) and, specifically in the optical case, entanglement between two modes in an interferometer (Jin *et al.*, 2013; Kok *et al.*, 2002). So far in this thesis we have been looking at multi-mode entangled states, such as the ECSs and NOON states, and these states have been shown to give precision advantages over states possessing no entanglement. However, it has been shown that entanglement is not required between the probe and reference systems for Heisenberg limited measurements of a linear phase shift (Munro *et al.*, 2001; Ralph, 2002; Tilma *et al.*, 2010), and furthermore it has been argued that the important resource for enhancing precision is actually coherence in the eigenbasis of the phase shift Hamiltonian (Girolami *et al.*, 2013). In this chapter we go beyond this to demonstrate that, in some well known scenarios, single mode superposition states have a significantly better robustness to loss than their multi-mode entangled counterparts, which allows them to achieve greatly enhanced precision measurements. We introduce a new state, the unbalanced cat state, that can

outperform the alternatives and can be created and measured with present day or near future technology, to a precision close to its theoretical bound.

As discussed in section 3.7 we are concerned here with measuring fragile systems, in which case it is imperative that high precision is achieved from a limited number of probe photons passing *through the sample*. In this regime we show in this chapter that single mode superposition states show significant improvements over the multi-mode alternatives and furthermore beat the 'optimal state' [1] (Demkowicz-Dobrzanski *et al.*, 2014; Kołodyński & Demkowicz-Dobrzański, 2013) for most loss rates, illustrating the importance of our results.

This chapter is based on the paper: Knott *et al.* (2014a).

5.2 No loss: superposition states are sufficient

We begin by reviewing work that has already addressed the question of multi- vs single- mode quantum states in metrology. A different approach to measurement than that which we have described so far involves weak force detection, which is concerned with detecting a small phase fluctuation about zero in a single shot measurement. For this task Munro *et al.* (2001) utilised a superposition of coherent states (a cat state): $|\Psi\rangle = \mathcal{N}(|\alpha\rangle + |-\alpha\rangle)$, where $\mathcal{N} = 1/\sqrt{2+2e^{-2\alpha^2}}$. Munro *et al.* (2001) modeled the force to be measured with the displacement operator, and discussed states such as squeezed states, entangled states and cat states, which they concluded all operate at the Heisenberg limit when measuring a weak force.

Another paper that looked at weak force detection was Tilma *et al.* (2010). They looked at three different quantum states, all involving a coherent state and either entanglement or a superposition. They used distinguishability between the initial state and the state after a phase shift as an approximate measure for the state's effectiveness to measure a phase, as given by $d = \langle\Psi|e^{i\hat{n}\phi}|\Psi\rangle$. They argued that $d \approx 0$ between phase shifted and unphased states means that the input is orthogonal to the output, and therefore the Cramér-Rao relation is most easily

[1] The optimal state we use here is defined for fixed photon number states in which the resource is the total number of photons used (Kołodyński & Demkowicz-Dobrzański, 2013). In our system we count the resource as the number of photons passing through the sample.

satisfied. By setting $d \approx 0$ and using some approximations, they showed that the smallest phase detectable by a superposition of a vacuum and a coherent state is given by $\pi/2\bar{n}$, where $\bar{n}$ is the average number of photons in the state. Their work showed that for a linear phase multi-mode entanglement is not necessary, and for a nonlinear phase multi-mode entanglement can even cause problems.

Another paper (Ralph, 2002) looked at the cat state $|\Psi\rangle = \mathcal{N}(|0\rangle + |\alpha\rangle)$, where $\mathcal{N} = 1/\sqrt{2 + 2e^{-\alpha^2/2}}$, in a scheme similar to that which we have been using in this thesis, namely using interferometry to measure a phase shift. They showed that putting $\mathcal{N}(|0\rangle + |\alpha\rangle)$ into two paths of an interferometer, one of which undergoes a phase shift, can lead to Heisenberg-precision measurements. In this chapter we will extend this work to look at how robust the cat state is to loss and how precisely it can be measured with a practically accessible scheme.

We begin our investigation by looking at the generic quantum state in interferometry: the NOON state (Afek *et al.*, 2010; Israel *et al.*, 2014; Lee *et al.*, 2002), given by $|\Psi_{NOON}\rangle_{a,b} = \frac{1}{\sqrt{2}}(|N,0\rangle_{a,b} + |0,N\rangle_{a,b})$. This state is maximally entangled between the two interferometer modes a and b. Using Eqs. (3.39) and (3.38) we have already seen that the NOON state can measure a phase with a quantum-enhanced precision of $\delta\phi_{NOON} = 1/N$, the Heisenberg limit. However, it is straightforward to show that the Heisenberg limit is attainable without the multi-mode entanglement exhibited by the NOON state, simply by utilising an analogous single mode superposition state $|\Psi_{NO}\rangle = \frac{1}{\sqrt{2}}(|N\rangle + |0\rangle)$ (Tilma *et al.*, 2010), which we refer to as the NO state: we find $\delta\phi_{NO} = 1/N$.

We have already seen that a more robust state for quantum metrology is the ECS, given by $|\Psi_{ECS}\rangle = \mathcal{N}_e(|\alpha,0\rangle + |0,\alpha\rangle)$ (Gerry, 1997; Gerry & Grobe, 2007; Gerry & Mimih, 2010; Gerry *et al.*, 2002, 2009; Joo *et al.*, 2011, 2012; Sanders, 2012, 1992) where $\mathcal{N}_e = 1/\sqrt{2 + 2e^{-\alpha^2}}$ and α characterises the coherent state (we take α to be real throughout this chapter, without loss of generality). We find that the QFI for this state is

$$F_Q = 4\alpha^2\mathcal{N}_e^2(1 + \alpha^2 - \alpha^2\mathcal{N}_e^2), \tag{5.1}$$

which approximately scales as $F_Q \propto \alpha^4$. However, a very similar QFI can be obtained without the entanglement by utilising the single mode analogue of the ECS, which we now call a 'balanced cat state' (due to the equal weighting between

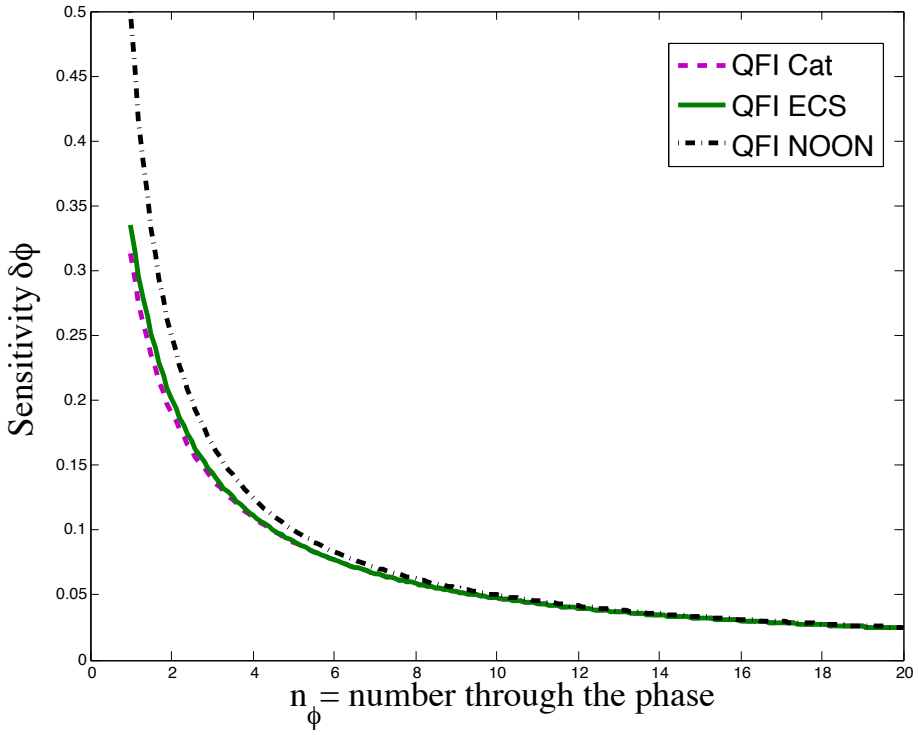

Figure 5.1: Here we plot the sensitivity $\delta\phi$, as given by the QFI and QCRB, against the average number of photons per state that pass through the phase shift, n_ϕ. Here there is no loss, and we see that for small photon numbers the ECS and cat states are better than the NOON and NO states (the NOON and NO have the same QFI). For very small numbers, the cat state is slightly better, but for the majority of n_ϕ values they have almost identical QFI. For larger numbers of photons all the states are more or less equivalent.

the two coherent states in the superposition), given by $|\Psi_{cat}\rangle = \mathcal{N}_c(|\alpha\rangle+|0\rangle)$ where $\mathcal{N}_c = 1/\sqrt{2+2e^{-\alpha^2/2}}$. Its QFI is also given by equation (5.1) but with $\mathcal{N}_e \to \mathcal{N}_c$. The results for the QCRBs of the different states, as given by equation (3.39), are shown in Fig. 5.1. We see that for small photon numbers the cat state is able to measure at the best precision, and for higher photon numbers all the states are almost identical.

From these QFI results it is clear that the cat state can be used for precisely determining a phase, but how exactly can the measurement be made? We will describe a simple scheme here, shown in Fig. 5.2 (ignore the beam splitter represent-

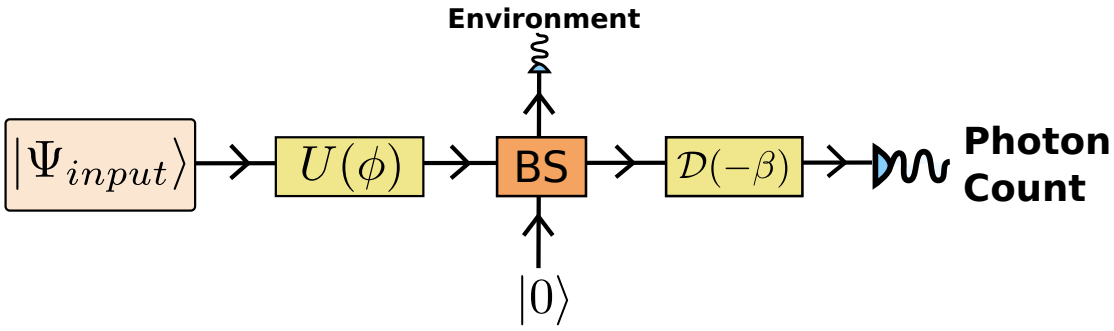

Figure 5.2: The input state $|\Psi_{input}\rangle$ first undergoes a phase shift $U(\phi) = e^{i\hat{a}^\dagger\hat{a}\phi}$. We model loss by the addition of a beam splitter with a vacuum port, and then trace over the environmental mode. To read out the phase we apply the displacement operator $\mathcal{D}(-\beta)$, with coherent state amplitude $-\beta$, and then count the number of photons in the state.

ing loss for now). Our initial state is an even cat state: $|\Psi_0\rangle = \mathcal{N}_c(|\alpha/2\rangle + |-\alpha/2\rangle)$. We describe how this even cat state can be made in section 4.4. We then act on the even cat state with the displacement operator, which in general acts on a coherent state by (Gerry & Knight, 2005)

$$D(\sigma)|\gamma\rangle = e^{-i\Im(\sigma^*\gamma)}|\gamma + \sigma\rangle \tag{5.2}$$

where σ and γ are two complex parameters. We displace as follows

$$|\Psi_1\rangle = D(\alpha/2)|\Psi_0\rangle = \mathcal{N}_c(|\alpha\rangle + |0\rangle). \tag{5.3}$$

We then apply a linear phase shift, giving $|\Psi_2\rangle = \mathcal{N}_c(|\alpha e^{i\phi}\rangle + |0\rangle)$. Next we displace the state back by $-\beta$ (where, for reasons we will see later, $\beta \gg \alpha$), to give

$$|\Psi_3\rangle = \mathcal{N}_c\left(e^{i\alpha\beta\sin\phi}|\alpha e^{i\phi} - \beta\rangle + |-\beta\rangle\right). \tag{5.4}$$

We then simply count the numbers of photons in this state. To do this we take $P(n) = |\langle n|\Psi_3\rangle|^2$ and use the usual Bayesian scheme to determine the phase. We can see that as ϕ changes our state oscillates between even and odd cat states, with different $P(n)$ probability distributions, and this is why the number measurement reveals information about the phase shift. We see the results for this

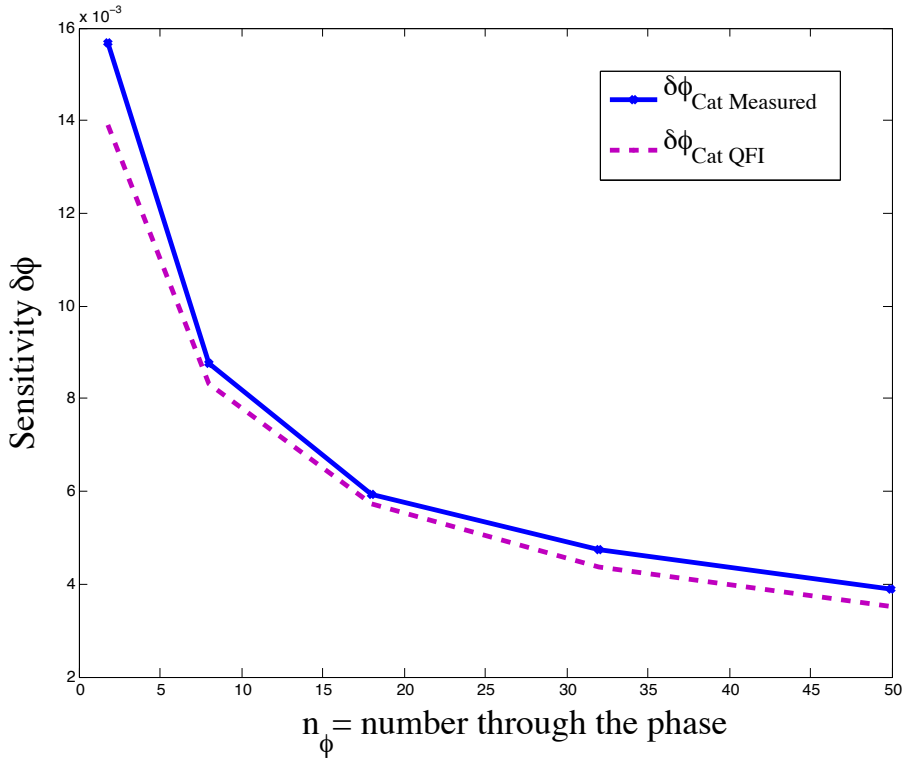

Figure 5.3: We can see that the displace and count measurement scheme is pretty much optimal.

measurement scheme, as compared to the bound given by the QFI and QCRB, in Fig. 5.3. We can see that this measurement scheme, without loss, is close to optimal.

5.3 Entanglement is detrimental with loss

We now show that in the presence of photon losses the single mode states give a significant improvement in phase sensitivity over their multi-mode analogues. As with the ECS calculations in the last chapter, we model loss by the addition of a beam splitter after the phase shift (Demkowicz-Dobrzanski *et al.*, 2009; Gkortsilas *et al.*, 2012; Joo *et al.*, 2011), as shown in Fig. 5.2, which has a probability of transmission η (and therefore a fraction $\mu = 1 - \eta$ of photons are lost). After tracing over the environment we have a mixed state ρ, and from this density

matrix the QFI can be determined. The density matrix for the cat state $|\Psi_1\rangle = \mathcal{N}_c(|\alpha\rangle + |0\rangle)$, after loss, is given by

$$\rho_{cat} = \mathcal{N}_c^2 \left[|\alpha_\eta e^{i\phi}\rangle\langle\alpha_\eta e^{i\phi}| + |0\rangle\langle 0| + e^{-\alpha_\mu^2/2} \left(|\alpha_\eta e^{i\phi}\rangle\langle 0| + |0\rangle\langle\alpha_\eta e^{i\phi}| \right) \right] \tag{5.5}$$

where $\alpha_\eta = \alpha\sqrt{\eta}$ and $\alpha_\mu = \alpha\sqrt{\mu}$. This has a very similar form to the ECS after loss, given in equation (4.21). Therefore using a similar method to Zhang *et al.* (2013), as described in section 4.5, we can represent and then diagonalise ρ_{cat} in the orthogonal cat state basis $|\Psi_\pm\rangle = \mathcal{N}_\pm(|\alpha_\eta e^{i\phi}\rangle \pm |0\rangle)$ to find the two nonzero eigenvalues and the corresponding eigenvectors. Using equation (3.36) and equation (3.39) we then analytically calculate the QFI and the QCRB.

We will now look at the QFI for the NO state $|\Psi_{NO}\rangle = \frac{1}{\sqrt{2}}(|N\rangle + |0\rangle)$, and show the full calculation, which highlights some of the general methods that can be used to find the eigenvectors and eigenvalues, and then find the QFI, of these states. The mixed state after loss for the NO state is given by

$$\rho_{NO} = \frac{1}{2}|0\rangle\langle 0| + \tag{5.6}$$
$$\frac{1}{2}\left(\sum_{k=0}^{N} \binom{N}{k} \sin^{2k}\theta \cos^{2(N-k)}\theta |N-k\rangle\langle N-k| + \cos^N\theta \left[|N\rangle\langle 0| e^{iN\phi} + |0\rangle\langle N| e^{-iN\phi} \right] \right)$$

where $\eta = \cos^2\theta$ is the probability of transmission. To find the QFI we need to find $\langle\lambda_m|\rho'_{NO}|\lambda_n\rangle$, for $m, n \in [0, ..., N]$. However, we find that $\langle\lambda_m|\rho'_{NO}|\lambda_n\rangle$ is equal to zero, except when $|\lambda_0\rangle = z(a|0\rangle + |N\rangle)$ and $|\lambda_N\rangle = z(|0\rangle - a^*|N\rangle)$. We then find

$$|\langle\lambda_0|\rho'_{NO}|\lambda_0\rangle|^2 = |\langle\lambda_N|\rho'_{NO}|\lambda_N\rangle|^2 = \frac{z^4 N^2 \cos^{2N}\theta}{4}\left(2|a|^2 - a^{*2}e^{-2iN\phi} - a^2 e^{2iN\phi}\right),$$
$$|\langle\lambda_0|\rho'_{NO}|\lambda_N\rangle|^2 = |\langle\lambda_N|\rho'_{NO}|\lambda_0\rangle|^2 = \frac{z^4 N^2 \cos^{2N}\theta}{4}\left(1 + |a|^4 + a^{*2}e^{-2iN\phi} + a^2 e^{2iN\phi}\right). \tag{5.7}$$

To find the values of a and z we write ρ_{NO} as

$$\rho_{NO} = c_{00}|0\rangle\langle 0| + c_{0N}|0\rangle\langle N| + c_{N0}|N\rangle\langle 0| + c_{NN}|N\rangle\langle N| + ... \tag{5.8}$$

We can then represent the coefficients of the $|0\rangle$ and $|N\rangle$ basis states as a 2x2 matrix:

$$\begin{bmatrix} c_{00} & c_{0N} \\ c_{N0} & c_{NN} \end{bmatrix} = 0.5 \begin{bmatrix} 1 + \sin^{2N}\theta & e^{-iN\phi}\cos^N\theta \\ e^{iN\phi}\cos^N\theta & \cos^{2N}\theta \end{bmatrix} \tag{5.9}$$

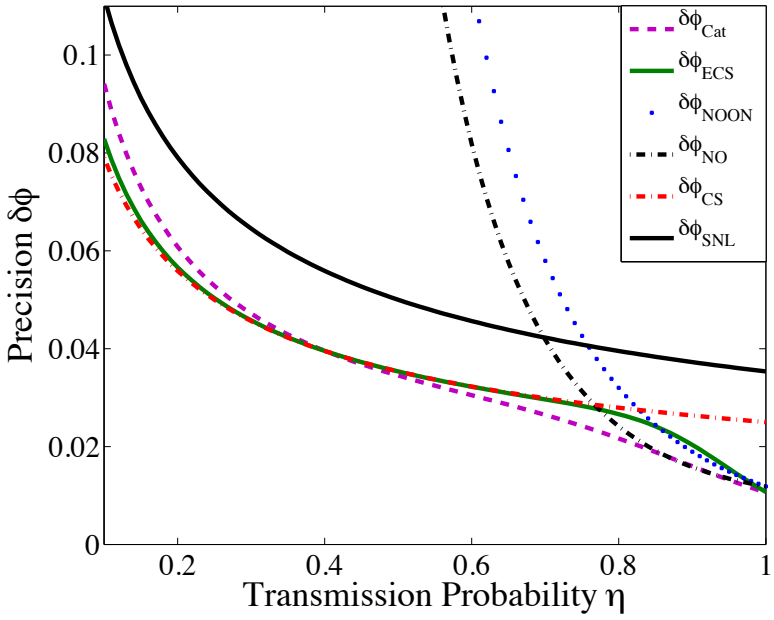

Figure 5.4: Multi-mode entanglement reduces phase precision. We show the QCRB, calculated (analytically) from the QFI, for the: cat state $\delta\phi_{\text{cat}}$; ECS $\delta\phi_{\text{ECS}}$; NOON state $\delta\phi_{\text{NOON}}$; NO state $\delta\phi_{\text{NO}}$; coherent state $\delta\phi_{\text{CS}}$ and the SNL $\delta\phi_{\text{SNL}}$. Here $\alpha = 3$, and for fair comparison the NOON and NO states have N such that the number of photons per state through the phase shift $\bar{n}_\phi$ is equal for each state. Therefore $\bar{n}_\phi(\text{NOON}) = \bar{n}_\phi(\text{NO}) = N/2$ is equal to $\bar{n}_\phi(\text{ECS}) = \bar{n}_\phi(\text{cat}) = \mathcal{N}^2\alpha^2$. We repeat each state m times so that the total number of photons sent through the phase shift is $R_\phi = m\bar{n}_\phi = 400$ (this is the same throughout our results).

Diagonalising this matrix, we find

$$\begin{aligned} a &= e^{-iN\phi} \\ z &= 1/\sqrt{\gamma^2+1} \\ \gamma &\in \mathbb{R}. \end{aligned} \tag{5.10}$$

This then allows us to calculate

$$\begin{aligned} |\langle\lambda_0|\rho'_{NO}|\lambda_0\rangle|^2 &= 0 \\ |\langle\lambda_0|\rho'_{NO}|\lambda_N\rangle|^2 &= 0.25N^2\cos^{2N}\theta. \end{aligned} \tag{5.11}$$

We can also find the eigenvalues from equation (5.9). Combining all this allows us to calculate, using equation (3.36), the QFI for the NO state

$$F_Q = N^2 \frac{2\cos^{2N}\theta}{1+\cos^{2N}\theta+\sin^{2N}\theta} = N^2 \frac{2\eta^N}{1+\eta^N+(1-\eta)^N}. \tag{5.12}$$

The QFI for the NOON state is significantly easier, as we find the eigenvectors to be

$$\begin{aligned} |\lambda_0\rangle &= \frac{1}{\sqrt{2}}(-e^{-iN\phi}|0,N\rangle + |N,0\rangle) \\ |\lambda_N\rangle &= \frac{1}{\sqrt{2}}(|0,N\rangle + e^{iN\phi}|N,0\rangle) \end{aligned} \tag{5.13}$$

and $\lambda_0 = 0$, $\lambda_N = \cos^{2N}\theta$. We therefore find $F_Q = N^2\eta^N$.

The results comparing the NOON state, NO state, ECS and cat state are shown in Fig. 5.4 for $\alpha = 3$ and in Fig. 5.5 for $\alpha = 2$. We see that with loss the NO state ($\delta\phi_{\text{NO}}$, black dashed-dotted line) can measure a phase to a higher precision than a NOON state ($\delta\phi_{\text{NOON}}$, blue dots). However, it is not clear how to create a NO state in a physically viable fashion [1]. We can also see from Fig. 5.4 that in the range of reasonable experimental transmission rates, $0.5 \leq \eta \leq 1$, (for example $\eta = 0.62$ in Demkowicz-Dobrzański *et al.* (2013)) the precision obtained by the cat state with $\alpha = 3$ ($\delta\phi_{\text{cat}}$, purple dashed line) is significantly better than the ECS ($\delta\phi_{\text{ECS}}$, green solid line). In this region the multi-mode entanglement in the ECS leads to a more fragile state and a worse precision. For higher loss rates the ECS performs better than the cat state, but we see in the next section that the single mode states can be modified to overcome this issue. The advantage gained by the cat state is even more evident in Fig. 5.5 for $\alpha = 2$, where we see that for the majority of loss rates the cat state performs best.

5.4 The unbalanced cat state

We now introduce a single mode state that generalises the cat state and displays an improvement in phase sensitivity over the ECS (and the other alternatives)

[1] We note that the NOON state has the same QFI as the NO state if there is only loss in the phase shift arm, highlighting the similarity between single mode metrology and a two mode scheme with loss only at the phase shift.

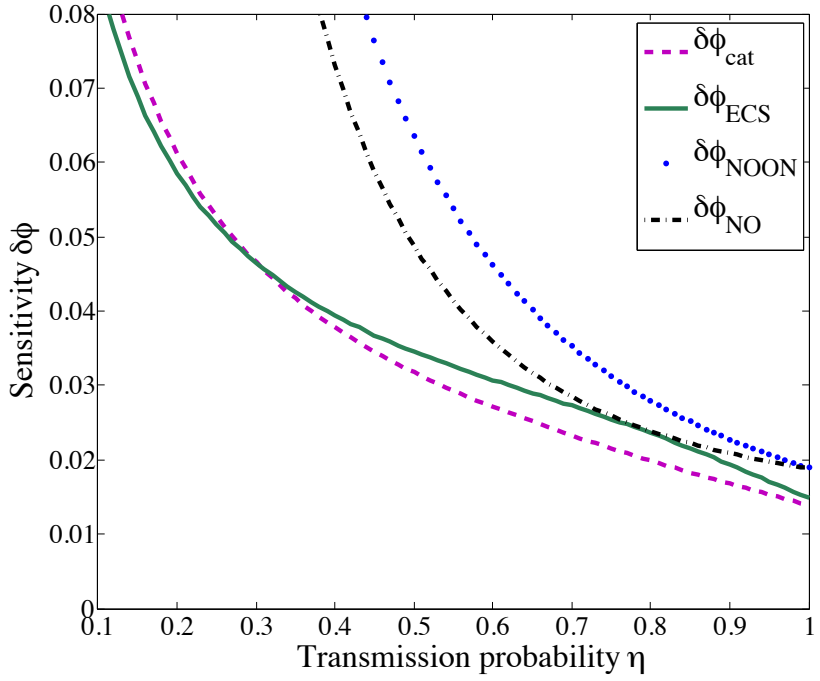

Figure 5.5: Here we see the results for $\alpha = 2$. It is clear that the cat state shows a significant robustness to loss as compared to the other states.

for all values of loss. We will refer to the state as the unbalanced cat state (UCS) and it is given by

$$|\Psi_{UCS}\rangle = \mathcal{N}_u(|\alpha(a)\rangle + a|0\rangle) \tag{5.14}$$

where $0 \leq a \leq 1$, $\mathcal{N}_u = 1/\sqrt{1 + a^2 + 2ae^{-\alpha(a)^2/2}}$, and $\alpha(a)$ is the solution to: $\alpha^2(a) = \bar{n}_\phi/\mathcal{N}_u^2(\alpha(a))$, where $\bar{n}_\phi$ is the number of photons passing through the phase shift per state. $\alpha(a)$ is defined in such a way as to keep the average number of photons through the phase shift independent of a, and it can be expressed in terms of the Lambert W-function. We note that taking $a = 1$ in equation (5.14) gives a balanced cat state of magnitude $\alpha_{bal} = \alpha(a = 1)$, and $a = 0$ gives a coherent state. One of the advantages of this state is that the 'quantumness' of the state can be altered by varying the parameter a. Loss collapses the quantum superposition, and so when there is high loss we can reduce a so that the state behaves more like a coherent state $|\alpha\rangle$, and with low loss we can set $a \sim 1$ so that we have an equal superposition state.

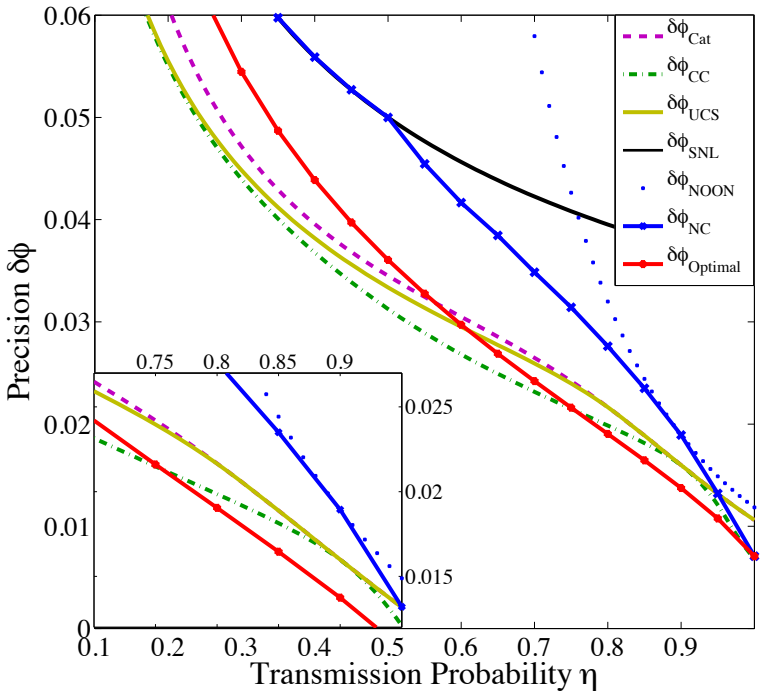

Figure 5.6: We see the large improvements gained by our single mode states. We show the (analytical) QCRB for the: cat state $\delta\phi_{\rm cat}$; UCS chopping $\delta\phi_{\rm CC}$; unbalanced cat state $\delta\phi_{\rm UCS}$; SNL $\delta\phi_{\rm SNL}$; NOON state $\delta\phi_{\rm NOON}$; NOON chopping strategy $\delta\phi_{\rm NC}$ and the optimal state in Kołodyński & Demkowicz-Dobrzański (2013) $\delta\phi_{\rm Optimal}$. Here $\alpha_{bal} = 3$, and for the chopped states we limit the cat state to $\alpha_{bal} \leq 5$ (and equivalently limit the NOON state and optimal state). We see that, at 50% loss, the UCS chopping strategy performs 40% better than the NOON chopping, and over 10% better than the 'optimal state'.

The reduced density matrix $\rho_{_{UCS}}$ for the UCS after the phase shift and loss is given by

$$\rho_{_{UCS}} = \tag{5.15}$$
$$\mathcal{N}_u^2 \left[|\alpha_\eta(a)e^{i\phi}\rangle\langle\alpha_\eta(a)e^{i\phi}| + a^2|0\rangle\langle 0| + ae^{-\alpha_\mu^2(a)/2}\left(|\alpha_\eta(a)e^{i\phi}\rangle\langle 0| + |0\rangle\langle\alpha_\eta(a)e^{i\phi}|\right)\right],$$

where $\alpha_\eta(a) = \alpha(a)\sqrt{\eta}$ and $\alpha_\mu(a) = \alpha(a)\sqrt{\mu}$. We find the QFI for this state with the same method as was used above for the balanced cat state. We see in Fig. 5.6 that the QCRB for the UCS ($\delta\phi_{\rm UCS}$, yellow solid line) improves upon the cat state ($\delta\phi_{\rm cat}$, purple dashed line). Although this improvement in the QCRB

is marginal, we will show that with a simple and practical measurement scheme the UCS, unlike the balanced cat state, can be utilised for phase measurements close to the QCRB. We note that both the cat and the UCS show large precision improvements over the SNL.

We can obtain a better precision still by using a 'chopping strategy', introduced in the case of NOON states in Dorner *et al.* (2009), in which different sized states (i.e. different $\bar{n}_\phi$) are used for different loss rates. We fix the total number of photons allowed through the phase shift, R_ϕ, and therefore the number of times m that a state is sent through the phase shift is inversely proportional to its average photon number $\bar{n}_\phi$. To illustrate why the chopping works, consider a NOON state, which has a QCRB given by

$$\delta\phi_{NOON} = \frac{1}{\sqrt{mF_q}} = \frac{1}{\sqrt{mN^2\eta^N}} \tag{5.16}$$

where η is the transmission probability, N is the number of photons in the NOON state, and m is the number of classical repeats. If we allow $R_\phi = 16$ photons to pass through the phase shift, then how can we best utilise these photons? Should we put all our eggs in one basket, or more specifically all 16 photons into one NOON state? Or is it better to divide the photons between different NOON states, for example we could take $N = 2$ and send this state through the phase $m = 8$ times. The QCRB for these two NOON states are shown in Fig. 5.7. For loss close to zero, it is always best to use all your photons in one NOON state (here we ignore the fact that large NOON states are difficult to make!). However, for larger loss rates a much better precision is obtained for the $N = 2$ NOON state repeated 8 times. This same principle works for all the quantum states we consider in this thesis: the larger states are always more fragile.

We now apply this chopping strategy to the UCS. The green dashed-dotted line ($\delta\phi_{\mathrm{CC}}$) in Fig. 5.6 shows a UCS optimised over $\bar{n}_\phi$ and the unbalancing parameter a for each loss rate. As described above, when there is no loss it is advantageous to put all your resources in the largest possible quantum state. However, it is not realistic to have arbitrarily large cat states (or any quantum state, for that matter), and so we limit the largest state here to having magnitude $\alpha_{bal} = 5$. We see that this chopping strategy applied to the unbalanced cat displays further

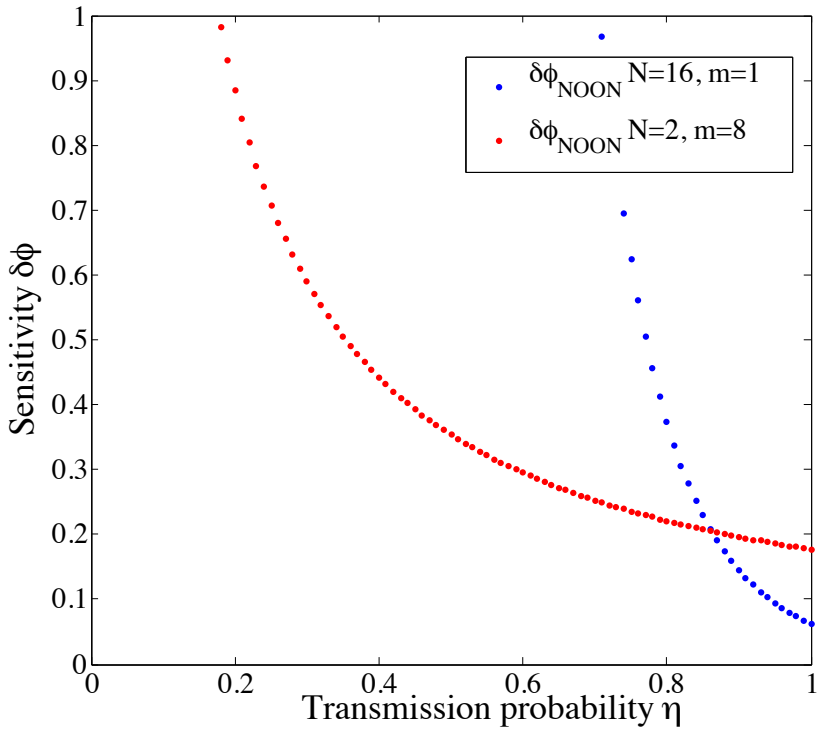

Figure 5.7: This figure compares the precision of 8 NOON states of size $N = 2$ with a single NOON state of size $N = 16$.

improvements over all the alternatives, including a large improvement over the NOON chopping strategy ($\delta\phi_{\mathrm{NC}}$) and the SNL ($\delta\phi_{\mathrm{SNL}}$).

A lot of work has been done in recent years in establishing the ultimate precision bounds of quantum metrology (Demkowicz-Dobrzański *et al.*, 2012; Demkowicz-Dobrzanski *et al.*, 2014; Escher *et al.*, 2011; Kołodyński & Demkowicz-Dobrzański, 2013). These bounds have been derived by counting the total number of photons used as the relevant resource. However, as we have discussed above, in probing delicate systems (Carlton *et al.*, 2010; Eckert *et al.*, 2008; Pototschnig *et al.*, 2011; Taylor *et al.*, 2013; Tey *et al.*, 2008; Wolfgramm *et al.*, 2013) it is the total number of photons *through the sample* that is important. To further emphasise the precision gains achieved by single mode states in this regime, we have included the 'optimal state' in Fig. 5.6 ($\delta\phi_{\mathrm{Optimal}}$, red line with dots) as given in Demkowicz-Dobrzanski *et al.* (2014); Kołodyński & Demkowicz-Dobrzański (2013).

By looking at the theoretical limits on the precision (given by the QCRB) for various single mode states, it is clear that these single mode superposition states have huge potential for making quantum-enhanced measurements. Despite this, it is not always clear how to make measurements that saturate this limit, and it is this issue that we turn to next.

5.5 A practical scheme for the UCS with loss

We will now describe a simple and practical scheme, shown in Fig. 5.2 and already introduced in section 5.2, for measuring a phase using a UCS, in the presence of loss, that comes close to the theoretical precision limit given by the QCRB. The initial resource required is a UCS. We have already seen in section 4.4 how a cat state of the form $\mathcal{N}_{c'}(|\alpha'\rangle + |-\alpha'\rangle)$ can be made. Some schemes create states of our desired form $|\Psi_{cat}\rangle = \mathcal{N}_c(|\alpha\rangle + |0\rangle)$ directly (Leghtas *et al.*, 2013), but if the output state is $\mathcal{N}_{c'}(|\alpha'\rangle + |-\alpha'\rangle)$ the application of a displacement operator (Paris, 1996) will create the state $|\Psi_{cat}\rangle$. The UCS can be created by simple adaptations of the methods for cat state preparation, for example preparing the Rydberg atom (described in section 4.4) in the unbalanced state $\mathcal{N}_R(|g\rangle + a|e\rangle)$ will give the output state $|\Psi_{UCS}\rangle$.

The first step in the phase detection scheme is the application of the linear phase shift to the UCS giving $|\Psi_{UCS}(\phi)\rangle = \mathcal{N}_c(|\alpha(a)e^{i\phi}\rangle + a|0\rangle)$. As discussed earlier, the loss is then modeled by a beam splitter, as shown in Fig. 5.2, with the resulting mixed state given by equation (5.15). We then apply the displacement operator $\mathcal{D}(-\beta) = e^{\beta^*\hat{a}-\beta\hat{a}^\dagger}$, which can be implemented in a simple manner by mixing the state with a large local oscillator at a highly transmittive beam splitter (Furusawa *et al.*, 1998; Paris, 1996). This gives

$$\begin{aligned}\rho &= \mathcal{D}(-\beta)\rho_{UCS}\mathcal{D}^\dagger(-\beta) \qquad (5.17)\\ &= \mathcal{N}_u^2\left[|\sigma\rangle\langle\sigma| + a^2|-\beta\rangle\langle-\beta| + ae^{-\alpha_\mu^2(a)/2}\left(e^{i\theta}|\sigma\rangle\langle-\beta| + e^{-i\theta}|-\beta\rangle\langle\sigma|\right)\right],\end{aligned}$$

where $\theta = \alpha_\eta(a)\beta\sin\phi$ and $\sigma = \alpha_\eta(a)e^{i\phi} - \beta$.

A photon-number resolving detector (PNRD) is then used to count the number of photons in the state ρ, and again a Bayesian scheme is used to infer the

phase ϕ and the precision with which it can be measured $\delta\phi$. PNRDs are an area of intense research (Eisaman *et al.*, 2011) and devices that are highly sensitive in the low photon regime, the area most relevant for this work, have been demonstrated (Calkins *et al.*, 2013; Divochiy *et al.*, 2008; Fukuda *et al.*, 2011). A more practical alternative to using number resolving detectors is to use a network of beam splitters to split the single output mode into a number of modes, and then use single photon detectors to perform pseudo-PNRD, as shown in Fig. 5.8. Single photon detectors have efficiencies as high as 93% in the infrared regime (Marsili *et al.*, 2013), and it is even possible for commercially available single photon detectors to obtain over 60% efficiency (Hadfield, 2009).

We obtain more precise measurements by taking $\beta > \alpha$, and we optimise over the phase ϕ. The phase precision for this measurement scheme ($\delta\phi_{\mathrm{UCSM}}$), found by simulation, is shown in Fig. 5.9 (crossed black line) where $\beta = 4\alpha_{bal}$. Our scheme shows significant improvements over: the SNL; the ECS with the measurement scheme in Knott *et al.* (2014b); and the NOON state (for most loss rates). We see that our scheme is much more robust than the NOON state which is quickly destroyed when the transmission rate drops below $\eta = 0.9$. Whilst the QCRB for the UCS shows only a small improvement over the (balanced) cat state, when we consider the measurement scheme the UCS is significantly better.

5.6 Why does the UCS come so close to the QCRB?

To understand why the UCS performs so well with this measurement scheme it is instructive to consider the case of a coherent state input, i.e $|\Psi_{input}\rangle = |\alpha\rangle$ in Fig 5.2. To find the phase precision for this input state and measurement scheme we use the propagation of errors formula

$$\delta\phi = \frac{\Delta\hat{X}}{|\frac{\partial\langle\hat{X}\rangle}{\partial\phi}|}, \tag{5.18}$$

where $\Delta\hat{X} = \sqrt{\langle\hat{X}^2\rangle - \langle\hat{X}\rangle^2}$, and we take the number counting measurement operator $\hat{X} = \hat{a}^\dagger\hat{a}$. We find that the QCRB, given by $\delta\phi_{\mathrm{CS}} = 1/\sqrt{2\alpha_\eta^2}$ with

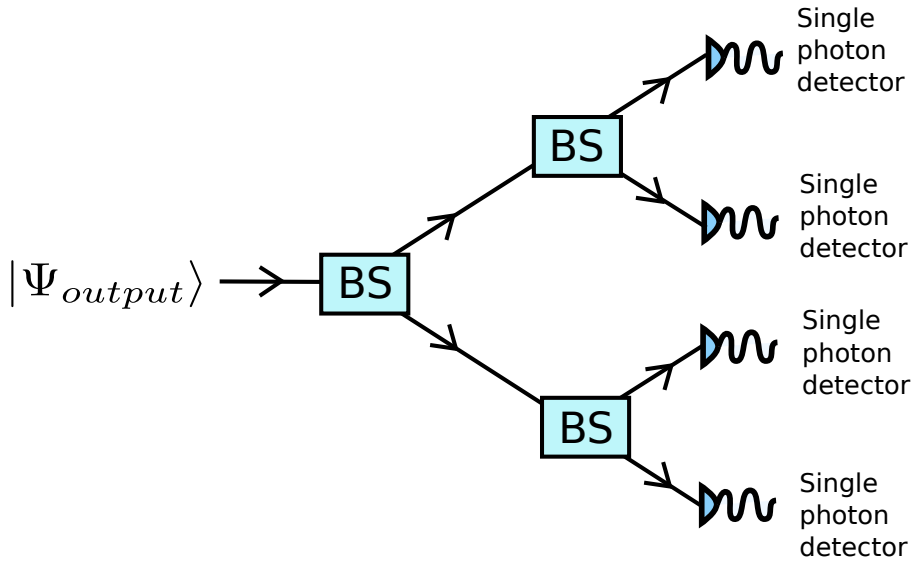

Figure 5.8: Single photon detectors are far more efficient than photon number resolving detectors (PNRDs). In order to count how many photons are in your state, a good alternative to PNRDs is to split your single mode output - which in this case contains the state $|\Psi_{output}\rangle$ - into multiple modes, using a network of beam splitters. We then use single photon detectors to count the overall number at the output, thus creating a pseudo-PNRD. In this example, to keep the diagram simple we split the single mode into only 4 modes, by using 50:50 beam splitters. However, we need the probability of detecting two photons at any output to be small, and so this set up will be useless if you are expecting more than two photons. Single mode detectors are commercially available, so it is not inconceivable to have a PNRD with over 32 modes.

transmissivity η, is saturated in the limit $\beta \to \infty$, where β is the displacement parameter. This is a $\sqrt{2}$ improvement over the generic scheme of a coherent state and a vacuum input fed into the arms of a standard Mach-Zehnder interferometer, which can measure at the SNL, $\delta\phi_{\mathrm{SNL}} = 1/\alpha_\eta$. This $\sqrt{2}$ improvement can also be attained when the displacement operator is replaced with a beam splitter mixing the phased coherent state with a coherent state $|\beta\rangle$, again for $\beta \to \infty$. We have found no explicit reference to this optimal measurement for a coherent state in the literature, but note that it bears a similarity to a homodyne measurement, in which a large reference beam is used to amplify a signal to enhance precision.

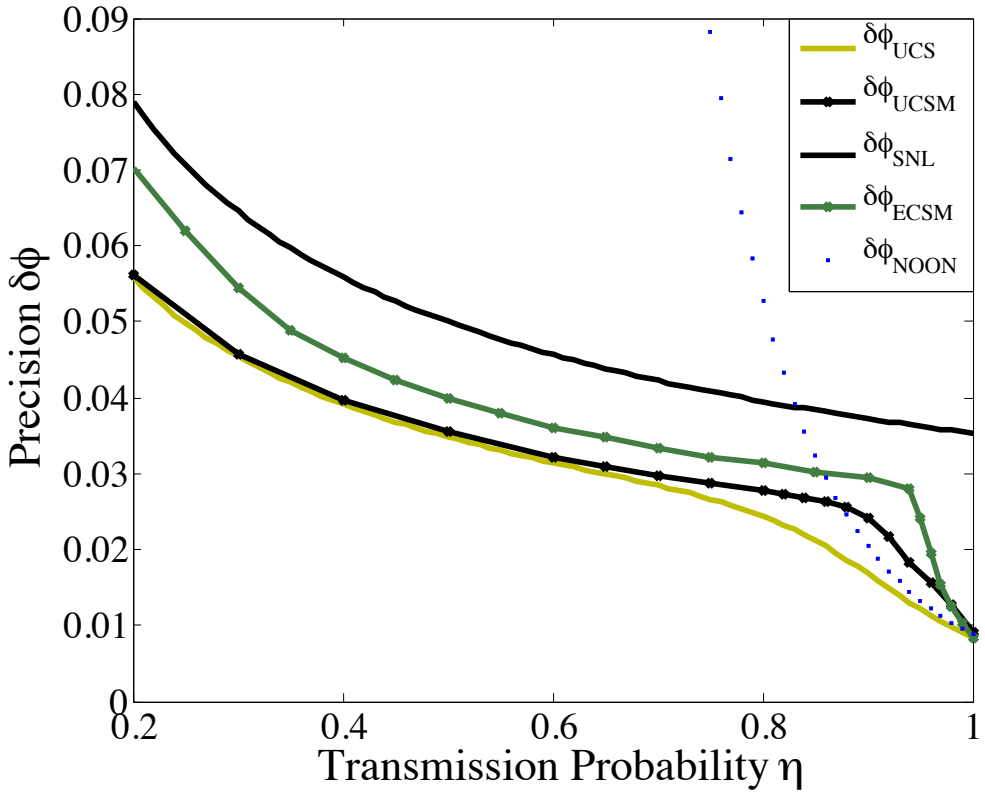

Figure 5.9: Our measurement scheme, $\delta\phi_{\mathrm{UCSM}}$, comes close the QCRB for the UCS, $\delta\phi_{\mathrm{UCS}}$, and shows large improvements over the ECS measurement scheme in section 4.4, $\delta\phi_{\mathrm{ECSM}}$. We see that our state surpasses the precision of the NOON state $\delta\phi_{\mathrm{NOON}}$ and the SNL $\delta\phi_{\mathrm{SNL}}$ for most loss rates. Here $\alpha_{bal} = 4$.

Since when $a = 0$ a UCS reduces to a coherent state, $\delta\phi_{\mathrm{CS}}$ is the upper bound on the phase precision that will be achieved with a UCS optimised over a. It is not clear how to get this close to saturating the bound for the balanced cat state, and so the UCS is significantly better when the measurement scheme is considered.

5.7 Do we need entanglement for quantum metrology?

In this chapter we have shown that 'single mode' superposition states show better robustness to loss than their multi-mode entangled counterparts. But do we truly

have a single mode state? And have we found a way of doing quantum metrology without entanglement? We begin by addressing the first of these questions.

It is simpler to first consider the case of a coherent state, $|\alpha\rangle$, in the scheme in Fig. 5.2. The state after the phase shift is given by $|\alpha e^{i\phi}\rangle$. Ignoring loss for now, the next step is to displace the state by $-\beta$. But the displacement operator is performed by mixing the state with a large local oscillator at a highly transmittive beam splitter (Furusawa *et al.*, 1998; Paris, 1996), and so a second mode is indeed needed. Furthermore, it is crucial that this second mode is phase-locked with the initial state entering the phase shift. An alternative way to measure the state $|\alpha e^{i\phi}\rangle$ is to mix it with a CS $|\beta\rangle$ at a 50:50 beam splitter, which again requires a second phase-locked mode.

Jarzyna & Demkowicz-Dobrzański (2012) discussed the use of external reference beams, such as the $|\beta\rangle$ in our scheme. They criticise work such as that by Joo *et al.* (2011), which we followed in section 4.2 to look at ECSs with loss. Jarzyna *et. al.* argue that the high precision attainable with an ECS with loss is only possible because of the use of external reference beams, and furthermore they say that Joo *et. al.* don't properly account for these extra beams and so their results are misleading. We have discussed in section 3.7 that in this thesis we choose to just count the number of photons *through the phase*, and in this regime the use of external reference beams is fine, and can just be seen as part of the final phase readout. Thus, our use of ECSs and single mode superposition states is justified.

To add some clarity to what we really mean by a 'single mode superposition state', we have re-drawn our scheme in Fig. 5.10, and have also included an illustration of the scheme in Fig. 5.11. We have included a variable beam splitter (VBS) before the photon counting, which accommodates the 50:50 beam splitter and the highly transmittive beam splitter used for the displacement operator. For generality we have also included number counting of both output modes, but generally we only need to count one mode, as in the scheme in Fig. 5.2. From Fig. 5.10 we can see that at the state preparation the initial state, over the two modes, is

$$|\Psi_{total,initial}\rangle = |\Psi_{input}\rangle \otimes |\Psi_{reference}\rangle = |\Psi_{input}, \Psi_{reference}\rangle. \tag{5.19}$$

For the case of the CS measuring the phase, this total initial state is

$$|\Psi_{total,initial}\rangle = |\Psi_{input}\rangle \otimes |\Psi_{reference}\rangle = |\alpha, \beta\rangle \tag{5.20}$$

whereas for the balanced cat state we have

$$|\Psi_{total,initial}\rangle = \mathcal{N}(|\alpha, \beta\rangle + |0, \beta\rangle) = \mathcal{N}(|\alpha\rangle + |0\rangle) \otimes |\beta\rangle. \tag{5.21}$$

There is therefore no entanglement between the probe state $|\Psi_{input}\rangle$ and the reference $|\Psi_{reference}\rangle$, which justifies our referring to the cat state as a single mode superposition state: there is no multi-mode entanglement. When we introduce loss, the loss acts separately on both arms, and the effect is that the reference beam is just reduced in size from $|\beta\rangle$ to $|\beta_\eta\rangle$. This just leaves us with a smaller reference beam, but as we are dealing with beams such that $\beta \gg \alpha$ this does not affect our scheme and we choose in the main text of this chapter to call the reference beam *after* loss $|\beta\rangle$. If the two modes were entangled then the loss would collapse the entangled state and we couldn't just separate the probe state from the reference beam.

This leads on to the second question: do we need entanglement for quantum metrology? We have shown that we don't need *multi-mode* entanglement, but do we still need intra-mode entanglement? This issue is discussed in detail by Demkowicz-Dobrzanski *et al.* (2014), who conclude that in states such as the cat and NO states entanglement exists *between the photons*, rather than between the modes - although this view is not universally agreed upon by researchers. Demkowicz-Dobrzanski *et al.* (2014) also argue that it is the intra-mode entanglement between photons that is the resource for quantum metrology, which could explain why NO and NOON states perform identically when there is no loss.

5.8 Optical quantum metrology

We have seen in the last few chapters that optical quantum metrology can surpass the classical limits to perform quantum-enhanced phase measurements. In particular we have shown that intrinsically robust continuous variable states, such as ECSs, can out-perform the fixed number NOON states when loss is considered.

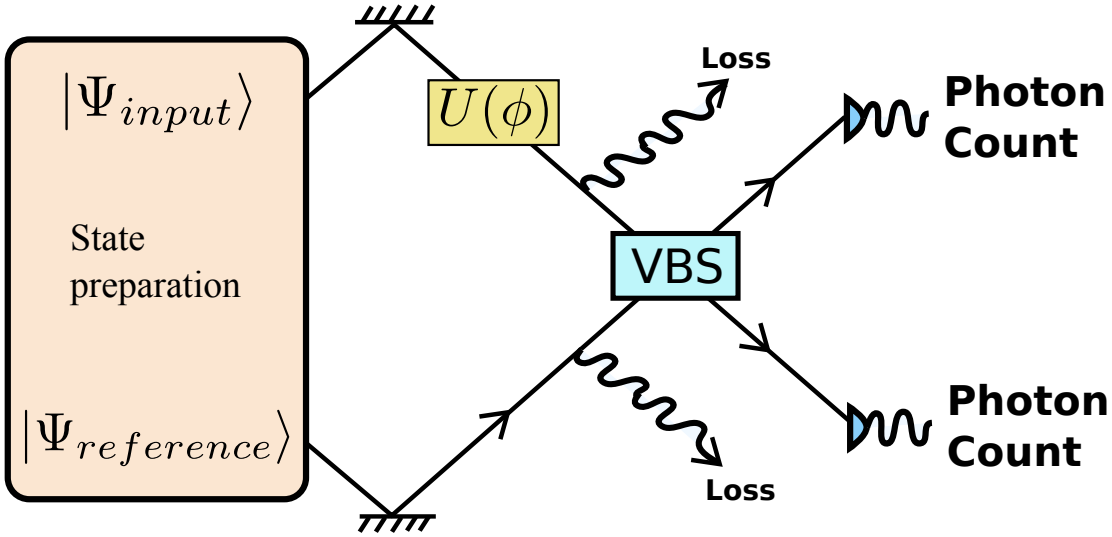

Figure 5.10: This figure shows the single mode scheme drawn in a different way, as to illustrate that a second mode is needed containing an in-phase reference beam. The state in the second mode isn't entangled with the probe state.

We then questioned whether multi-mode entanglement - a property present in ECSs and NOON states - is necessary for quantum metrology, and we concluded that when loss is present, single mode superposition states are more robust than their multi-mode counterparts and allow for more precise measurements. Next, we turn to a different regime, namely spin systems, and we will see that their fundamentally different decoherence mechanism can lead to a measurement precision that surpasses the SNL even in scaling.

Figure 5.11: This illustration by Joseph Hollis shows the 'single mode' scheme. Laser light (a coherent state) is split in two by a semi-reflective mirror (beam splitter). A fraction of the state then enters a 'cat maker', which can be any method of creating a cat state such as the method in the text of creating $|0\rangle + |\alpha\rangle$. The cat states then enter an animal cell and interacts with a lipid granule; this step can be replaced with any process that induces a phase shift. The phase-shifted cat states are then shown in blue; the change of phase is represented by the colour chance. The cat states then interact with the reference laser at another semi-reflected mirror. Finally the light detectors count the numbers of photons, and from this measurement the phase can be determined.

5. DO WE NEED MULTI-MODE ENTANGLEMENT IN OPTICAL QUANTUM METROLOGY?

Chapter 6

Spin cat states in quantum metrology

6.1 Beating the SNL in scaling

We have seen in this thesis that optical states prepared in superpositions or with multi-mode entanglement have shown great promise for quantum enhanced phase measurements, but invariably suffer from the crippling effects of decoherence that can often render the states useless when large states or medium/high losses are considered. In the optical systems we have studied thus far it is possible to beat the SNL in absolute terms, but when there is any loss it is impossible to beat the *scaling* of $1/\sqrt{N}$ (Demkowicz-Dobrzański *et al.*, 2012; Escher *et al.*, 2011). However, spin systems (Arecchi *et al.*, 1972; Radcliffe, 1971; Zhang *et al.*, 1990) have a distinctly different process of decoherence known as dephasing, which has shown to give greatly improved robustness to loss (Chin *et al.*, 2012; Matsuzaki *et al.*, 2011). In particular, Matsuzaki *et al.* (2011) showed that a system dominated by non-Markovian noise can give a scaling advantage of $N^{1/4}$ over classical states, but for a specific case, namely a GHZ state in a spin system (Greenberger *et al.*, 1989). They showed that when the exposure time is appropriately chosen to lie within the non-Markovian region, a GHZ state can beat the uncorrelated states, in scaling, even with decoherence. Chin *et al.* (2012) conjectured that in the general case a system dominated by non-Markovian noise can give a scaling advantage of $1/N^{1/4}$ over uncorrelated (classical) states, giving an overall precision

scaling as $1/N^{3/4}$.

Achieving this scaling advantage in practice may be somewhat more difficult, as large GHZ states are notoriously difficult to make. For example the largest GHZ states known to the author are 14 qubit-states created by Monz *et al.* (2011), and so GHZ states are not yet a reasonable candidate for practical sub-SNL metrology. To overcome this we present here a class of states which also give the $1/N^{1/4}$ enhanced scaling, whilst being realisable with current technology: the spin cat states, or superpositions of spin coherent states. We present various schemes for creating and measuring these spin cats, showing that in the near future spin systems could be used for robust quantum enhanced measurements.

This chapter will be structured as follows. We begin by introducing spin coherent states, and then present a scheme that creates a spin cat state, which we show can be used to measure a magnetic field. We then present the non-Markovian dephasing model, and show that when this is considered the spin cat states give a scaling advantage over the SNL. To finish, we explain methods of how the phase can be read out from the spin cat state. Thus we present a complete and experimentally realisable scheme for measuring a magnetic field in a system dominated by non-Markovian noise (the prevalent noise in, for example, NV centres).

This chapter is loosely based on the paper: Tanaka *et al.* (2014).

6.2 Spin coherent states and important definitions

We begin with some definitions that will be used throughout this chapter. We are considering spin states, and so we begin by stating the Pauli matrices:

$$\sigma_x = \begin{bmatrix} 0 & 1 \\ 1 & 0 \end{bmatrix}; \quad \sigma_y = \begin{bmatrix} 0 & -i \\ i & 0 \end{bmatrix}; \quad \sigma_z = \begin{bmatrix} 1 & 0 \\ 0 & -1 \end{bmatrix}. \tag{6.1}$$

We then define the excited and ground states of the spins in our system as the eigenstates of σ_z: $\sigma_z|e\rangle = |e\rangle$ and $\sigma_z|g\rangle = -|g\rangle$. We therefore take $|g\rangle$ as the ground state, as if we consider the Hamiltonian to be σ_z then the $|g\rangle$ state has a

lower energy. In vector form we have

$$|e\rangle = \begin{bmatrix} 1 \\ 0 \end{bmatrix}; \quad |g\rangle = \begin{bmatrix} 0 \\ 1 \end{bmatrix}. \tag{6.2}$$

We also need the raising and lowering operators, which are defined such that $\sigma_+|g\rangle = |e\rangle$ and $\sigma_-|e\rangle = |g\rangle$ and therefore

$$\sigma_+ := |e\rangle\langle g| = \begin{bmatrix} 0 & 1 \\ 0 & 0 \end{bmatrix}; \quad \sigma_- := |g\rangle\langle e| = \begin{bmatrix} 0 & 0 \\ 1 & 0 \end{bmatrix}. \tag{6.3}$$

We now consider a collection of N spins. Follow the convention we take the 'vacuum' state of a collection of N spins to be: $|\mathbf{0}\rangle := |g\rangle^{\otimes N}$. The collective operators acting on the N spins are then defined as: $\hat{S}_\mu := \sum_{j=1}^{N} \sigma_\mu^{(j)}$ where $\mu = x, y, z, +, -$, and here $\sigma_\mu^{(j)}$ only acts on the j^{th} spin, leaving the others unchanged.

Ensembles of spins, such as nitrogen-vacancy (NV) centres (Saito *et al.*, 2013), can be prepared such that all the spins are aligned: this is a spin coherent state (Arecchi *et al.*, 1972). For a system of N spin 1/2 particles, a spin coherent state can be defined as

$$|z\rangle = |z, N\rangle := \mathcal{N}_z(|g\rangle + z|e\rangle)^{\otimes N} \tag{6.4}$$

where the normalisation is $\mathcal{N}_z = (1 + |z|^2)^{-N/2}$. Here $z \in \mathbb{C}$ parameterises the state. Interestingly, in the limit of $N \to \infty$ the spin coherent states are mathematically equivalent to optical coherent states (Arecchi *et al.*, 1972; Dooley *et al.*, 2013; Radcliffe, 1971). We have seen that quantum states comprised of optical coherent states show huge promise for robust quantum metrology (Joo *et al.*, 2011; Knott *et al.*, 2014b; Munro *et al.*, 2001; Ralph, 2002), which gives further motivation for studying the equivalent spin systems, especially given the favourable loss mechanism of non-Markovian dephasing.

Another way to write the spin coherent state is

$$|z, N\rangle = \mathcal{N}_z \sum_{n=0}^{N} \frac{(z\hat{S}_+)^n}{n!}|\mathbf{0}\rangle. \tag{6.5}$$

It is not immediately clear why equations 6.4 and 6.5 are equal. To show this, we see that in $(\hat{S}_+)^n|\mathbf{0}\rangle$ each set of n excitations are repeated $n!$ times, whereas for $(|g\rangle + z|e\rangle)^{\otimes N}$ each spin is only excited once. Therefore

$$\begin{aligned}
&\mathcal{N}_z(|g\rangle + z|e\rangle)^{\otimes N} \\
&= \mathcal{N}_z(|g\rangle + z|e\rangle)(|g\rangle + z|e\rangle)(...) \\
&= \mathcal{N}_z(|p_0\rangle + z|p_1\rangle + z^2|p_2\rangle ...) \\
&= \mathcal{N}_z \sum_{n=0}^{N} z^n |p_{n,e}\rangle \\
&= \mathcal{N}_z \sum_{n=0}^{N} \frac{(z\hat{S}_+)^n}{n!}|\mathbf{0}\rangle
\end{aligned} \tag{6.6}$$

where $|p_n\rangle$ is the state of all permutations of n excited spins.

6.3 Measuring a phase with a spin cat state

We now need to create a superposition of spin coherent states: a spin cat state (Gerry, 1997). One method of creating a spin cat state is to couple a qubit in the $|+\rangle_q$ state to the spin coherent state $|iz, N\rangle$, and apply the appropriate Tavis-Cummings-like Hamiltonian (Dooley & Spiller, 2014; Dooley *et al.*, 2013; Guo & Zheng, 1996; Tavis & Cummings, 1968):

$$e^{i\chi\sigma_z\hat{N}}|+, iz\rangle_q \rightarrow |1\rangle_q|ize^{-i\chi}\rangle + |0\rangle_q|ize^{i\chi}\rangle \tag{6.7}$$

where $\hat{N}$ counts the number of excited spins in the spin coherent state and the subscript q labels the qubit. We take the time of evolution such that $\chi = \pi/2$, and then measure the qubit in the x basis, which unentangles it from the spins, leaving us with a spin cat state[1]:

$$|\Psi_0\rangle = \mathcal{N}_c(|z\rangle + |-z\rangle) \tag{6.8}$$

where

$$\mathcal{N}_c = \frac{1}{\sqrt{2 + 2\left(\frac{1-|z|^2}{1+|z|^2}\right)^N}}. \tag{6.9}$$

[1]Strictly speaking half the time we obtain the odd spin cat state: $|\Psi\rangle \propto |z\rangle - |-z\rangle$.

This method could be done, for example, with a single flux qubit coupled to an ensemble of NV centres (Saito *et al.*, 2013; Zhu *et al.*, 2011). Alternatively, spin cat states can be created by collapse and revival in Jaynes-Cummings and Tavis-Cummings models (Dooley *et al.*, 2013; Everitt *et al.*, 2012; Jarvis *et al.*, 2009, 2010). In both these examples, the restriction on the size of z (resulting from the Bosonic approximation) is $|z|^2 \ll N$ (Dooley *et al.*, 2013). Whilst in principle the state in equation 6.8 can be used to measure a phase, we will see later that the readout stage of the phase estimation is straight forward if we use the state: $|\Psi_1\rangle = \mathcal{N}_c(|\mathbf{0}\rangle + |z\rangle)$. To create this state, we need to apply the displacement operator for spins.

The displacement operator for spins is equivalent to a rotation on each qubit, defined as $R(\theta,\phi) := e^{i\frac{\theta}{2}\hat{S}\cdot\hat{n}}$, where we take the unit vector $\hat{n}$ to be in the xy plane so that $\hat{n} = (\sin\phi, -\cos\phi, 0)$. We write

$$R(\theta,\phi) := e^{i\frac{\theta}{2}(\sin(\phi)\hat{S}_x - \cos(\phi)\hat{S}_y)} = \left(e^{i\frac{\theta}{2}\hat{A}}\right)^{\otimes N} \tag{6.10}$$

where $\hat{A} = \sin(\phi)\sigma_x - \cos(\phi)\sigma_y$. We see that $\hat{A}$ squares to the identity ($\hat{A}^2 = \hat{\mathbb{I}}$) and using this we find

$$R(\theta,\phi) = \left(e^{i\frac{\theta}{2}\hat{A}}\right)^{\otimes N} = \left(\cos\frac{\theta}{2}\hat{\mathbb{I}} + i\sin\frac{\theta}{2}\hat{A}\right)^{\otimes N}. \tag{6.11}$$

An alternative way to define a spin coherent state is as: $|\theta,\phi\rangle := R(\theta,\phi)|\mathbf{0}\rangle$. Using this we see that a spin coherent state can be parameterised by the polar and azimuthal angles, θ and ϕ respectively, on the Bloch sphere:

$$|\theta,\phi\rangle = (\cos\frac{\theta}{2}|g\rangle - e^{-i\phi}\sin\frac{\theta}{2}|e\rangle)^{\otimes N}. \tag{6.12}$$

To show that this is equivalent to our definition in equation 6.4, we first set $z = -e^{-i\phi}\tan\frac{\theta}{2}$. We then see that

$$R(\theta,\phi) \equiv R(z) = \mathcal{N}_z\left(\mathbb{I} + z\sigma_+ - z^*\sigma_-\right)^{\otimes N}. \tag{6.13}$$

By taking $|z,N\rangle = R(z)|\mathbf{0}\rangle$ we then reproduce equation 6.4. In order to see how the rotation affects a spin cat state, we must first find how two rotations combine.

We see that

$$R(z_2)|z_1\rangle = \mathcal{N}_1\mathcal{N}_2(1-z_1z_2^*)^N[|g\rangle + \frac{z_1+z_2}{1-z_1z_2^*}|e\rangle]^{\otimes N} \tag{6.14}$$
$$= \left(\frac{1-z_1z_2^*}{|1-z_1z_2^*|}\right)^N |z_0\rangle$$

where the parameter here is

$$z_0 = \frac{z_1+z_2}{1-z_1z_2^*} \tag{6.15}$$

and the normalisations are $\mathcal{N}_a = (1+|z_a|^2)^{-N/2}$ for $a = 1$ *or* 2. Alternatively, to illustrate the similarity between the optical displacement in equation 5.2 and the spin rotation here, we can combine the rotations to give

$$R(z_2)|z_1\rangle = e^{i\eta N}|z_0\rangle \tag{6.16}$$

where

$$\eta = \tan^{-1}\left(\frac{\Re(1-z_1z_2^*)}{\Im(1-z_1z_2^*)}\right). \tag{6.17}$$

The rotation then acts on the spin cat state in equation 6.8 as follows:

$$R(z)|\Psi_0\rangle = \mathcal{N}_c(|\mathbf{0}\rangle + R(z)|z\rangle) \tag{6.18}$$
$$= \mathcal{N}_c(|\mathbf{0}\rangle + \left|\frac{2z}{1-|z|^2}\right\rangle)$$
$$= \mathcal{N}_c(|\mathbf{0}\rangle + |z'\rangle)$$

leaving us with the desired cat state. This scheme for creating a spin cat state has the restriction that $z \ll 1$. However, alternative methods exist which may shown improvement upon this, potentially allowing spin cat states with larger z to be made (Tanaka *et al.*, 2014).

Next we show that this state can be used to measure a magnetic field, which is represented by the operator $e^{i\hat{N}\omega t}$. With no decoherence, after interacting the state $|\Psi_1\rangle = \mathcal{N}_c(|\mathbf{0}\rangle + |z\rangle)$[1] with a magnetic field for time t, we have

$$|\Psi_2\rangle = \mathcal{N}_c(|\mathbf{0}\rangle + |ze^{i\omega t}\rangle). \tag{6.19}$$

[1]Here we relabel $z' \to z$.

It has been shown that without decoherence a spin cat state can measure a magnetic field with a precision approaching the Heisenberg limit (Dooley *et al.*, 2013): the precision scales with with the number of spins N as $\delta\omega \sim 1/N$. This is the fundamental limit for phase measurements, but it is impossible to obtain this limit in realistic systems, which inevitably suffer from decoherence. In systems with Markovian dephasing, such as optical systems with photon loss, the precision always reduces to the SNL at best, $\delta\omega \sim 1/\sqrt{N}$ (Demkowicz-Dobrzański *et al.*, 2012; Escher *et al.*, 2011). However, in the following sections we will see that a system with non-Markovian dephasing can actually beat the SNL in scaling, even when decoherence is included.

6.4 The master equation for dephasing

In the relevant systems of interest in this chapter, such NV centres in diamond, the dominant source of decoherence is non-Markovian frequency-dependent $1/f$ noise (Chirolli & Burkard, 2008; Kakuyanagi *et al.*, 2007; Kane, 1998; Tanaka *et al.*, 2014). Unlike Markovian noise, which is effectively random, non-Markovian dephasing is correlated in time. This can, for example, be the result of coupling between the electron and nuclear spins in NV centres. More specifically, if the correlation time of the environment is shorter than the time scale of the system Hamiltonian dynamics, we can consider the noise as Markovian, which provides a linear (or exponential) decay. On the other hand, if the correlation time of the noise is long, the decay is considered as non-Markovian, which shows a quadratic decay.

We begin by looking at a single spin: $|\Psi_{(1)}\rangle = \mathcal{N}_1(|g\rangle + z|e\rangle)$, where $\mathcal{N}_1 = 1/\sqrt{1+z^2}$ and here we take z to be real. It is easier here to work in matrix form, in which the single spin is given by

$$|\Psi_{(1)}\rangle = \mathcal{N}_1 \begin{pmatrix} z \\ 1 \end{pmatrix}. \tag{6.20}$$

Dephasing is governed by the master equation (Matsuzaki, 2010; Matsuzaki *et al.*, 2011)

$$\frac{\partial \rho_{(1)}(t)}{\partial t} = -\frac{\Gamma^2 t}{2}[\sigma_z, [\sigma_z, \rho_{(1)}(t)]]. \tag{6.21}$$

where Γ denotes the dephasing rate. For the single spin the solution to the master equation is

$$\rho_{(1)}(t) = \mathcal{N}_1 \begin{pmatrix} z^2 & ze^{-\Gamma^2 t^2} \\ ze^{-\Gamma^2 t^2} & 1 \end{pmatrix}. \tag{6.22}$$

The dephasing master equation can be generalised to N spins as follows (Matsuzaki, 2010; Matsuzaki *et al.*, 2011):

$$\frac{\partial \rho_{(N)}(t)}{\partial t} = -\frac{\Gamma^2 t}{2} \sum_{j=1}^{N} [\sigma_z^{(j)}, [\sigma_z^{(j)}, \rho_{(N)}(t)]]. \tag{6.23}$$

where $\sigma_z^{(j)}$ acts on the j^{th} spin, and leaves the others unaffected. An alternative form of this equation, which is easier to work with, is

$$\frac{\partial \rho_{(N)}(t)}{\partial t} = -\Gamma^2 t \sum_{j=1}^{N} (\rho_{(N)}(t) - \sigma_z^{(j)} \rho_{(N)}(t) \sigma_z^{(j)}). \tag{6.24}$$

We can then find the solution to this master equation for an N spin system prepared with all the spins aligned, i.e. a spin coherent state: $|z\rangle = |\Psi_{(1)}\rangle^{\otimes N} = \mathcal{N}_z(|g\rangle + z|e\rangle)^{\otimes N}$. Because the state is separable and the dephasing works separately on each pure state qubit, we get: $\tilde{\rho}(t) = \rho_{(1)}(t)^{\otimes N}$. We have included the tilde here for clarity later in the calculation, and dropped the (N) subscript.

We now look at the spin cat state: $\mathcal{N}_c(|\mathbf{0}\rangle + |z\rangle)$, which has initial density matrix

$$\rho_{cat}(t=0) = \mathcal{N}_c^2(|\mathbf{0}\rangle\langle\mathbf{0}| + |z\rangle\langle z| + |\mathbf{0}\rangle\langle z| + |z\rangle\langle\mathbf{0}|). \tag{6.25}$$

After dephasing, we can see that $|\mathbf{0}\rangle\langle\mathbf{0}|$ is unchanged, and $|z\rangle\langle z|$ is the spin coherent state which becomes $\tilde{\rho}(t)$. Therefore the only terms that we have to calculate are the cross terms. First, we find that $(\hat{S}_+)^j|\mathbf{0}\rangle\langle\mathbf{0}|$ becomes $e^{-j\Gamma^2 t^2}(\hat{S}_+)^j|\mathbf{0}\rangle\langle\mathbf{0}|$ with dephasing, because every $|g\rangle\langle e|$ combination picks up the factor $e^{-\Gamma^2 t^2}$. From this we find

$$\rho_{cat}(t) = \mathcal{N}_c^2 \left[|\mathbf{0}\rangle\langle\mathbf{0}| + \tilde{\rho}(t) + \mathcal{N}_z \sum_{j=0}^{N} \frac{z^j}{j!} e^{-j\Gamma^2 t^2} \left((\hat{S}_+)^j |\mathbf{0}\rangle\langle\mathbf{0}| + |\mathbf{0}\rangle\langle\mathbf{0}| (\hat{S}_-)^j \right) \right] \tag{6.26}$$

6.5 Sub-SNL precision even with decoherence

We will now see that for non-Markovian dephasing, the spin cat state is able to beat the SNL in scaling. The full master equation governing dephasing, in the presence of a magnetic field ω which we wish to measure, is given by Matsuzaki (2010); Matsuzaki *et al.* (2011)

$$\frac{\partial\rho}{\partial t} = -\frac{i\omega}{2}\sum_{j=1}^{N}[\sigma_z^{(j)},\rho] - \frac{\Gamma^2 t}{2}\sum_{j=1}^{N}[\sigma_z^{(j)},[\sigma_z^{(j)},\rho]]. \tag{6.27}$$

If the initial state is a spin coherent state $|z\rangle$, the master equation is solved by

$$\tilde{\rho} = \mathcal{N}_z^2\left[|g\rangle\langle g| + \tilde{z}^*|g\rangle\langle e| + \tilde{z}|e\rangle\langle g| + |z|^2|e\rangle\langle e|\right]^{\otimes N} \tag{6.28}$$

where $\tilde{z} = ze^{i\omega t-\Gamma^2 t^2}$. This is the same calculation above but now z can be complex, and we now include the effect of the magnetic field (which plays the equivalent role of the optical phase). For the spin cat state $\mathcal{N}_c(|\mathbf{0}\rangle + |z\rangle)$ we find (from equation (6.26))

$$\rho(t) = \mathcal{N}_c^2\left[|\mathbf{0}\rangle\langle\mathbf{0}| + \tilde{\rho} + \mathcal{N}_d\left(|\tilde{z}\rangle\langle\mathbf{0}| + |\mathbf{0}\rangle\langle\tilde{z}|\right)\right]. \tag{6.29}$$

where $\mathcal{N}_d = (1+|z|^2e^{-2\Gamma^2t^2})^{N/2}/(1+|z|^2)^{N/2}$.

We are now interested in how precisely this decohered state $\rho(t)$ can measure the magnetic field ω. To find the precision we use (Chin *et al.*, 2012; Huelga *et al.*, 1997)

$$\delta^2\omega = \frac{P(1-P)}{\mu|\partial P/\partial\omega|^2} \tag{6.30}$$

where $P = \langle\Phi_0|\rho(t)|\Phi_0\rangle$ is the probability of finding the spin cat state in the state $|\Phi_0\rangle = \frac{1}{\sqrt{2}}(|\mathbf{0}\rangle + i|z\rangle)$, and μ is the total number of experimental data points (Chin *et al.*, 2012). P can be seen as the result if we measure the state $\rho(t)$ in the measurement basis $|\Phi_0\rangle = \frac{1}{\sqrt{2}}(|\mathbf{0}\rangle + i|z\rangle)$, which is similar to the initial state, but with a phase difference i between the $|\mathbf{0}\rangle$ and $|z\rangle$.

Using this formula we find numerically that the spin cat state can measure ω with a precision scaling as $\delta\omega \sim 1/N^{0.75}$, as shown in Fig. 6.1. It has been shown that the best possible precision attainable with uncorrelated spins scales with the number of spins N as $1/\sqrt{N}$, the SNL (Chin *et al.*, 2012). The spin cat

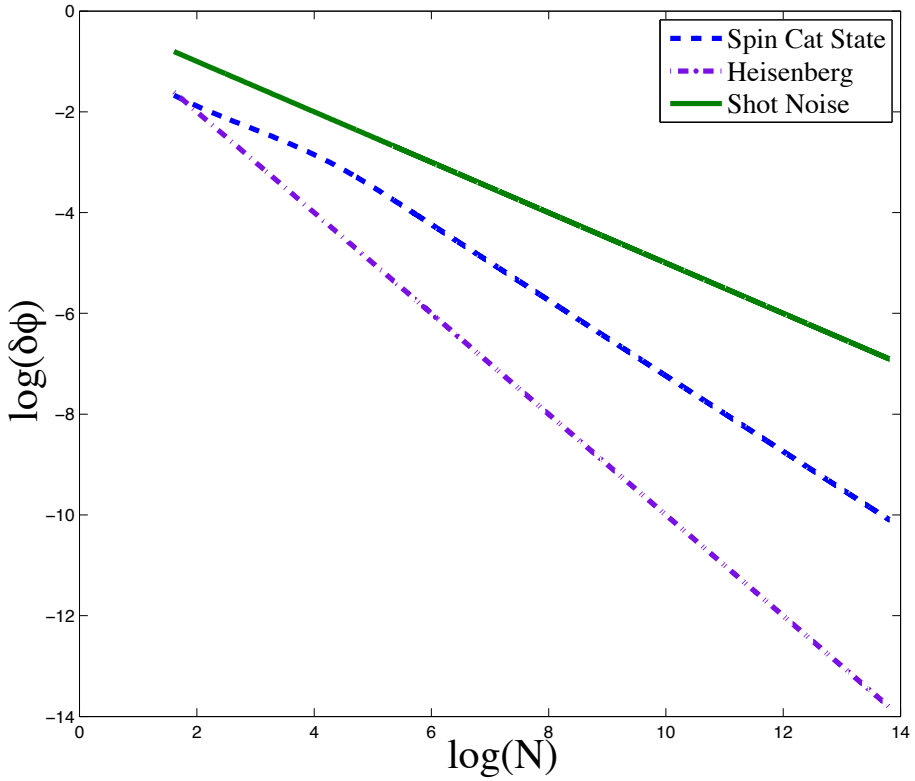

Figure 6.1: This log-log plot shows that a spin cat state undergoing non-Markovian dephasing can measure a magnetic field, represented by the phase $\delta\phi$, with a precision that scales as $\sim 1/N^{0.75}$. We see that this scaling surpasses the SNL by a factor of $N^{1/4}$, and is in turn outperformed by the Heisenberg limit, which has a scaling of $1/\sqrt{N}$.

state therefore beats the uncorrelated case by a factor of $N^{1/4}$, which agrees well with the result found for GHZ states (Matsuzaki *et al.*, 2011), and furthermore this saturates the hypothesised best attainable limit in Chin *et al.* (2012).

In order to find the attainable precision $\delta\omega$, we have to find the optimal time t in which to perform the experiment. The total time allowed to estimate the field ω is T, and so the number of data points we obtain in time T is $\mu = T/t$. For GHZ states, Matsuzaki *et. at.* showed that the optimal time to perform each ω estimation is $t \propto 1/\sqrt{N}$. We use this same optimal time here. This makes sense, as in the limit of $z \to \infty$ the cat state is equivalent to a GHZ state.

We have shown that the spin cat state can measure a phase (i.e. a magnetic field) with a precision that scales with $1/N^{0.75}$, but as in the optical case, we still have to find a way of actually reading out this phase, and it is this task that we will discuss next.

6.6 Reading out the phase

To describe the phase readout stage, for simplicity we will consider the pure state $|\Psi_2\rangle = \mathcal{N}_c(|\mathbf{0}\rangle + |ze^{i\omega t}\rangle)$. For the first step we rotate the state back by $-z/2$, which gives

$$\begin{aligned} |\Psi_3\rangle &= R(-z/2)|\Psi_2\rangle = \mathcal{N}_c(|-z/2\rangle + R(-z/2)|ze^{i\omega t}\rangle) \\ &= \mathcal{N}_c(|-z/2\rangle + e^{i\eta_\omega N}\left|\frac{ze^{i\omega t} - z/2}{1+|z|^2e^{i\omega t}/2}\right\rangle \end{aligned} \tag{6.31}$$

where $\eta_\omega = \eta_\omega(\omega)$ can be found using equation 6.17. If we take the approximations $\omega t \ll 1$, $z \ll 1$ and $N \gg 1$, we find that

$$|\Psi_3\rangle \approx |-z/2\rangle + e^{i\eta_\omega N}|z/2\rangle. \tag{6.32}$$

This state oscillates between an even and odd cat state with the phase $\eta_\omega N$, which depends on ω, and therefore measuring whether this state has even or odd numbers of excited spins can allow us to determine ω.

Indeed we saw in section 5.2 that with the optical cat state all we need to do is count the number of photons in the displaced-back cat state in order to determine the phase to a high precision. The analogous measurement for the spin system is to count the number of spins in the excited state, which can in theory be done with photons directly: if we shine resonant light onto the NV centres they will only emit a photon if they are excited. Admittedly this is hard to do in practice, but shows that in principle we can determine the phase using this method; future work will look at improving this scheme and running simulations, as we have done in the optical case, to determine the precision with which we can measure ω. An alternative scheme for reading out the phase can be found in Tanaka *et al.* (2014).

6.7 Chapter conclusion

We have presented a scheme by which we can create a spin cat state, apply a phase shift by means of a magnetic field, and then measure the phase. When the dominating noise is non-Markovian, we have shown that the spin cat state can measure at a precision that beats the SNL by a scaling of $1/N^{1/4}$, which equals the best known attainable precision when a GHZ state is used as quantum resource (Matsuzaki *et al.*, 2011). Using our scheme we expect that a spin cat state could perform sub-SNL measurements in a real experimental setting, even when realistic noise models are included.

Chapter 7

Conclusions and discussion

We began this thesis by describing a scheme in which the relative position localisation of particles is accompanied by quantum entanglement. This mechanism sheds light on the quantum to classical transition, as it proposes that the classical phenomena of localisation can be accompanied by entanglement, which is generally considered a purely quantum property. We then presented an experiment that can test this localisation mechanism, and furthermore the technology needed to perform the experiment is already available.

Next we introduced the main focus of this thesis: quantum metrology. After describing various optical schemes, which we will summarise below, we ended by looking at spin systems. When photon losses are included, optical quantum systems, whilst being able to out-perform the classical limits by a constant factor, cannot achieve a precision that *scales* better than the SNL $\propto 1/\sqrt{N}$. However, we saw that the decoherence mechanism prevalent in spin systems, namely non-Markovian dephasing, allows for precision measurements that beat the SNL by a scaling of $1/\sqrt{N^{1/4}}$. We showed in this thesis that this scaling advantage can be achieved with spin cat states. We then presented a scheme to create these states using present day technology, and we briefly introduced a method to extract the phase information. Future work into the spin systems could focus on this measurement scheme, and it would be beneficial to perform the same analysis we have done with the optical states: simulating a Bayesian scheme to determine the precision that could be obtained by a real experiment.

The bulk of this thesis, and the main focus of research for the author, is on optical quantum metrology. We have seen here that optical quantum states can beat the SNL and measure a phase shift with a precision at the Heisenberg limit. However, as with all quantum mechanical areas of research, decoherence can be a huge problem in performing quantum-enhanced measurements in realistic systems. We have seen that photon loss - the dominant source of decoherence in optical interferometry - is highly destructive to NOON states, which lose their precision advantage quickly as loss is increased. However, continuous variable states such as ECSs are intrinsically more robust to loss, and we saw that, as shown by the QFI, they can outperform both the NOON states and the SNL for the majority of loss rates.

Despite this, up to now it has not been at all clear how the full potential of ECSs as robust states for quantum metrology, as demonstrated by their QFI, can be exploited. Previous measurement schemes were unable to access the full phase information stored in the ECS after loss, and the suppression of the off diagonal coherence had the effect of making ECSs even worse than NOON states. However, we have presented here a more advanced measurement scheme that not only recovers the phase information with loss, but also comes close to saturating the QFI. Moreover we have shown that the input can be tailored so that we can always achieve a higher precision than NOON states. This allows us to achieve sub-classical precision measurements that outperform the alternative states for the majority of loss rates, including the rates thought to be realistic in an experiment. Furthermore, our scheme uses quantum resources that have already been created in the lab.

The potential of ECSs is clear from our results, but there are a number of alternative states that also can make sub-SNL measurements. These include the squeezed states as proposed by Caves (1981), the Holland and Burnett states in Holland & Burnett (1993), and the much more recent two-mode squeezed vacuum in Cable & Durkin (2010). Future work on ECSs should therefore include a thorough comparison of the ECSs with these states. The squeezed states used in GW detection (Aasi *et al.*, 2013) are of particular interest, as they are to date the only example of a routine use of quantum-enhanced optical metrology. ECSs

should be compared to these states to assess whether they can be used in this regime.

Whilst GW detection is the only place to use quantum-enhanced measurements routinely, there are many examples of proof-of-principle experiments or areas that would benefit from optical quantum metrology, such as spin ensembles (Wolfgramm *et al.*, 2013), biological systems (Carlton *et al.*, 2010; Taylor *et al.*, 2013), atoms (Eckert *et al.*, 2008; Tey *et al.*, 2008) and single molecules (Pototschnig *et al.*, 2011). We argued in section 3.7 that in all these examples the relevant resource to count is the number of photons passing *through the phase shift*. This idea has been neglected in much of the work on optical quantum metrology which takes the view that we should count the *total* numbers of photons used in a scheme. But we believe that, especially given the direction of quantum metrology towards technological applications, the way in which we count resources should be considered for each application. If we follow this then *all* the optical quantum metrology applications known to this author, with the exception of GW detection, are concerned with fragile systems in which only the number of photons through the phase is important. And we saw in chapter 5 that when we do count our resources in this way, some very interesting results can be obtained. In particular, we find that multi-mode entanglement is not only unnecessary for phase estimation at the Heisenberg limit, it is actually detrimental to precision measurements when loss in included.

This conclusion is significant because all of the examples of quantum metrology states mentioned above - ECSs, NOON states, squeezed states, Holland and Burnett states and the two-mode squeezed vacuum - use multimode entanglement to beat the classical limits. Therefore, when considering fragile system sampling, it is likely that single-mode alternatives to these states can be found that can show improved precision[1]. Following this principle we introduced a single mode quantum superposition state: the unbalanced cat state. This state shows significant improvements over the alternatives, and can be created and precisely measured with present day, or near future, technology. We show that by tuning the degree of superposition in our state, and additionally by 'chopping' our

[1]We note that this has recently been done with single mode squeezed states, confirming their great potential, in Sahota & Quesada (2015).

states into different sized chunks depending on loss rates, we can produce further improvements to our phase estimation scheme that allow us to surpass the best possible precision obtained by multi-mode-entangled states, as given by the 'optimal state' (Demkowicz-Dobrzanski *et al.*, 2014; Kołodyński & Demkowicz-Dobrzański, 2013). We expect that this work will open up a new approach to optical quantum metrology based on single mode states which will have huge potential for future precision measurement protocols.

References

Aad, G., Abajyan, T., Abbott, B., Abdallah, J., Abdel Khalek, S., Abdelalim, A., Abdinov, O., Aben, R., Abi, B., Abolins, M. *et al.* (2012). Observation of a new particle in the search for the standard model Higgs boson with the ATLAS detector at the LHC. *Phys. Lett. B*, **716**, 1–29. 19

Aasi, J., Abadie, J., Abbott, B., Abbott, R., Abbott, T., Abernathy, M., Adams, C., Adams, T., Addesso, P., Adhikari, R. *et al.* (2013). Enhanced sensitivity of the LIGO gravitational wave detector by using squeezed states of light. *Nature Photon.*, **7**, 613–619. 20, 23, 120

Abadie, J., Abbott, B., Abbott, R., Abbott, T., Abernathy, M., Accadia, T., Acernese, F., Adams, C., Adhikari, R., Affeldt, C. *et al.* (2012). Search for gravitational waves from low mass compact binary coalescence in LIGO's sixth science run and Virgo's science runs 2 and 3. *Phys. Rev. D*, **85**, 082002. 44

Afek, I., Ambar, O. & Silberberg, Y. (2010). High-NOON states by mixing quantum and classical light. *Science*, **328**, 879–881. 51, 85, 87

Anisimov, P.M., Raterman, G.M., Chiruvelli, A., Plick, W.N., Huver, S.D., Lee, H. & Dowling, J.P. (2010). Quantum metrology with two-mode squeezed vacuum: parity detection beats the Heisenberg limit. *Phys. Rev. Lett.*, **104**, 103602. 54

Arecchi, F., Courtens, E., Gilmore, R. & Thomas, H. (1972). Atomic coherent states in quantum optics. *Phys. Rev. A*, **6**, 2211. 107, 109

Barnett, S. (2009). *Quantum information*, vol. 16. Oxford University Press, USA. 22

Bartley, T.J., Donati, G., Spring, J.B., Jin, X.M., Barbieri, M., Datta, A., Smith, B.J. & Walmsley, I.A. (2012). Multiphoton state engineering by heralded interference between single photons and coherent states. *Phys. Rev. A*, **86**, 043820. 73

Bayes, M. & Price, M. (1763). An essay towards solving a problem in the doctrine of chances. by the late Rev. Mr. Bayes, FRS communicated by Mr. Price, in a letter to John Canton, AMFRS. *Philosophical Transactions (1683-1775)*, 370–418. 32

Bell, J. (1964). On the Einstein-Podolsky-Rosen paradox. *Physics*, **1**, 195–200. 22, 23

Braunstein, S. & Caves, C. (1994). Statistical distance and the geometry of quantum states. *Phys. Rev. Lett.*, **72**, 3439–3443. 57

Breuer, H. & Petruccione, F. (2002). *The theory of open quantum systems*. Oxford University Press, USA. 25

Brune, M., Hagley, E., Dreyer, J., Maitre, X., Maali, A., Wunderlich, C., Raimond, J. & Haroche, S. (1996). Observing the progressive decoherence of the "meter" in a quantum measurement. *Phys. Rev. Lett.*, **77**, 4887. 73

Bücker, R., Perrin, A., Manz, S., Betz, T., Koller, C., Plisson, T., Rottmann, J., Schumm, T. & Schmiedmayer, J. (2009). Single-particle-sensitive imaging of freely propagating ultracold atoms. *New J. Phys.*, **11**, 103039. 35, 39

Cable, H. & Durkin, G.A. (2010). Parameter estimation with entangled photons produced by parametric down-conversion. *Phys. Rev. Lett.*, **105**, 013603. 120

Calkins, B., Mennea, P.L., Lita, A.E., Metcalf, B.J., Kolthammer, W.S., Lamas-Linares, A., Spring, J.B., Humphreys, P.C., Mirin, R.P., Gates, J.C. *et al.* (2013). High quantum-efficiency photon-number-resolving detector for photonic on-chip information processing. *Opt. Express*, **21**, 22657–22670. 99

Cappellaro, P., Emerson, J., Boulant, N., Ramanathan, C., Lloyd, S. & Cory, D.G. (2005). Entanglement assisted metrology. *Phys. Rev. Lett.*, **94**, 020502. 85

Carlton, P.M., Boulanger, J., Kervrann, C., Sibarita, J.B., Salamero, J., Gordon-Messer, S., Bressan, D., Haber, J.E., Haase, S., Shao, L. *et al.* (2010). Fast live simultaneous multiwavelength four-dimensional optical microscopy. *Proc. Natl. Acad. Sci.*, **107**, 16016–16022. 23, 61, 97, 121

Caves, C.M. (1981). Quantum-mechanical noise in an interferometer. *Phys. Rev. D*, **23**, 1693. 120

Chatrchyan, S., Khachatryan, V., Sirunyan, A.M., Tumasyan, A., Adam, W., Aguilo, E., Bergauer, T., Dragicevic, M., Erö, J., Fabjan, C. *et al.* (2012). Observation of a new boson at a mass of 125 GeV with the CMS experiment at the LHC. *Phys. Lett. B*, **716**, 30–61. 19

Chin, A.W., Huelga, S.F. & Plenio, M.B. (2012). Quantum metrology in non-Markovian environments. *Phys. Rev. Lett.*, **109**, 233601. 107, 115, 116

Chirolli, L. & Burkard, G. (2008). Decoherence in solid-state qubits. *Adv. Phys.*, **57**, 225–285. 113

Cooper, J., Hallwood, D. & Dunningham, J. (2010). Entanglement-enhanced atomic gyroscope. *Phys. Rev. A*, **81**, 043624. 57

Demkowicz-Dobrzanski, R., Dorner, U., Smith, B., Lundeen, J., Wasilewski, W., Banaszek, K. & Walmsley, I. (2009). Quantum phase estimation with lossy interferometers. *Phys. Rev. A*, **80**, 013825. 51, 66, 90

Demkowicz-Dobrzański, R., Kołodyński, J. & Guţă, M. (2012). The elusive Heisenberg limit in quantum-enhanced metrology. *Nat. Commun.*, **3**, 1063. 60, 97, 107, 113

Demkowicz-Dobrzański, R., Banaszek, K. & Schnabel, R. (2013). Fundamental quantum interferometry bound for the squeezed-light-enhanced gravitational wave detector geo 600. *Phys. Rev. A*, **88**, 041802. 81, 93

Demkowicz-Dobrzanski, R., Jarzyna, M. & Kolodynski, J. (2014). Quantum limits in optical interferometry. *arXiv preprint arXiv:1405.7703*. 50, 52, 60, 61, 86, 97, 103, 122

Divochiy, A., Marsili, F., Bitauld, D., Gaggero, A., Leoni, R., Mattioli, F., Korneev, A., Seleznev, V., Kaurova, N., Minaeva, O., Gol'tsman, G., Lagoudakis, K.G., Benkhaoul, M., Lévy, F. & Fiore, A. (2008). Superconducting nanowire photon-number-resolving detector at telecommunication wavelengths. *Nature Photon.*, **2**, 302–306. 99

Dooley, S. & Spiller, T.P. (2014). Fractional revivals, multiple-Schrödinger-cat states, and quantum carpets in the interaction of a qubit with n qubits. *Phys. Rev. A*, **90**, 012320. 110

Dooley, S., McCrossan, F., Harland, D., Everitt, M.J. & Spiller, T.P. (2013). Collapse and revival and cat states with an n-spin system. *Phys. Rev. A*, **87**, 052323. 109, 110, 111, 113

Dorner, U., Demkowicz-Dobrzanski, R., Smith, B., Lundeen, J., Wasilewski, W., Banaszek, K. & Walmsley, I. (2009). Optimal quantum phase estimation. *Phys. Rev. Lett.*, **102**, 40403. 51, 96

Dunningham, J. & Kim, T. (2006). Using quantum interferometers to make measurements at the Heisenberg limit. *J. Mod. Opt.*, **53**, 557–571. 47, 49, 50, 51, 72

Dunningham, J., Rau, A. & Burnett, K. (2005). From pedigree cats to fluffy-bunnies. *Science*, **307**, 872–875. 26

Eckert, K., Romero-Isart, O., Rodriguez, M., Lewenstein, M., Polzik, E.S. & Sanpera, A. (2008). Quantum non-demolition detection of strongly correlated systems. *Nature Phys.*, **4**, 50–54. 23, 61, 97, 121

Einstein, A. (1905). The photoelectric effect. *Ann. Phys*, **17**, 132. 21

Einstein, A., Podolsky, B. & Rosen, N. (1935). Can quantum-mechanical description of physical reality be considered complete? *Phys. Rev.*, **47**, 777. 22, 23

Einstein, A. *et al.* (1905). On the electrodynamics of moving bodies. *Annalen der Physik*, **17**, 50. 19

Eisaman, M.D., Fan, J., Migdall, A. & Polyakov, S.V. (2011). Invited review article: Single-photon sources and detectors. *Rev. Sci. Instrum.*, **82**, –. 99

Englert, F. & Brout, R. (1964). Broken symmetry and the mass of gauge vector mesons. *Phys. Rev. Lett.*, **13**, 321–323. 19

Escher, B., de Matos Filho, R. & Davidovich, L. (2011). General framework for estimating the ultimate precision limit in noisy quantum-enhanced metrology. *Nature Phys.*, **7**, 406–411. 60, 97, 107, 113

Everitt, M.J., Munro, W. & Spiller, T. (2012). Overcoming decoherence in the collapse and revival of spin Schrödinger-cat states. *Phys. Rev. A*, **85**, 022113. 111

Feynman, R.P. (1967). *The character of physical law*, vol. 66. MIT press. 21

Fuhrmanek, A., Lance, A., Tuchendler, C., Grangier, P., Sortais, Y. & Browaeys, A. (2010). Imaging a single atom in a time-of-flight experiment. *New J. Phys.*, **12**, 053028. 35, 39

Fukuda, D., Fujii, G., Numata, T., Amemiya, K., Yoshizawa, A., Tsuchida, H., Fujino, H., Ishii, H., Itatani, T., Inoue, S. & Zama, T. (2011). Titanium-based transition-edge photon number resolving detector

with 98% detection efficiency with index-matched small-gap fiber coupling. *Opt. Express*, **19**, 870–875. 99

Furusawa, A., Sørensen, J.L., Braunstein, S.L., Fuchs, C.A., Kimble, H.J. & Polzik, E.S. (1998). Unconditional quantum teleportation. *Science*, **282**, 706–709. 98, 102

Gerrits, T., Glancy, S., Clement, T., Calkins, B., Lita, A., Miller, A., Migdall, A., Nam, S., Mirin, R. & Knill, E. (2010). Generation of optical coherent-state superpositions by number-resolved photon subtraction from the squeezed vacuum. *Phys. Rev. A*, **82**, 031802. 73, 74

Gerry, C. & Knight, P. (1997). Quantum superpositions and schrödinger cat states in quantum optics. *American Journal of Physics*, **65**, 964–974. 73

Gerry, C. & Knight, P. (2005). *Introductory quantum optics*. Cambridge university press. 89

Gerry, C.C. (1997). Generation of Schrödinger cats and entangled coherent states in the motion of a trapped ion by a dispersive interaction. *Phys. Rev. A*, **55**, 2478. 87, 110

Gerry, C.C. & Grobe, R. (2007). Nonlocal entanglement of coherent states, complementarity, and quantum erasure. *Phys. Rev. A*, **75**, 034303. 87

Gerry, C.C. & Mimih, J. (2010). Heisenberg-limited interferometry with pair coherent states and parity measurements. *Phys. Rev. A*, **82**, 013831. 87

Gerry, C.C., Benmoussa, A. & Campos, R.A. (2002). Nonlinear interferometer as a resource for maximally entangled photonic states: Application to interferometry. *Phys. Rev. A*, **66**, 013804. 49, 52, 87

Gerry, C.C., Mimih, J. & Benmoussa, A. (2009). Maximally entangled coherent states and strong violations of Bell-type inequalities. *Phys. Rev. A*, **80**, 022111. 87

Giovannetti, V., Lloyd, S. & Maccone, L. (2006). Quantum metrology. *Phys. Rev. Lett.*, **96**, 10401. 85

Girolami, D., Tufarelli, T. & Adesso, G. (2013). Characterizing nonclassical correlations via local quantum uncertainty. *Phys. Rev. Lett.*, **110**, 240402. 85

Gkortsilas, N., Cooper, J. & Dunningham, J. (2012). Measuring a completely unknown phase with sub-shot-noise precision in the presence of loss. *Phys. Rev. A*, **85**, 063827. 51, 66, 90

Glauber, R.J. (1963). Coherent and incoherent states of the radiation field. *Physical Review*, **131**, 2766. 52

Greenberger, D.M., Horne, M.A. & Zeilinger, A. (1989). Going beyond Bell's theorem. In *Bell's theorem, quantum theory and conceptions of the universe*, 69–72, Springer. 107

Guo, G.C. & Zheng, S.B. (1996). Generation of Schrödinger cat states via the Jaynes-Cummings model with large detuning. *Phys. Lett. A*, **223**, 332–336. 110

Hadfield, R.H. (2009). Single-photon detectors for optical quantum information applications. *Nature Photon.*, **3**, 696–705. 99

Hofmann, H.F. (2009). All path-symmetric pure states achieve their maximal phase sensitivity in conventional two-path interferometry. *Phys. Rev. A*, **79**, 033822. 54

Holland, M. & Burnett, K. (1993). Interferometric detection of optical phase shifts at the Heisenberg limit. *Phys. Rev. Lett.*, **71**, 1355. 51, 120

Huelga, S.F., Macchiavello, C., Pellizzari, T., Ekert, A.K., Plenio, M. & Cirac, J. (1997). Improvement of frequency standards with quantum entanglement. *Phys. Rev. Lett.*. 115

Israel, Y., Rosen, S. & Silberberg, Y. (2014). Supersensitive polarization microscopy using NOON states of light. *Phys. Rev. Lett.*, **112**, 103604. 87

Jarvis, C., Rodrigues, D., Györffy, B., Spiller, T., Short, A. & Annett, J. (2009). Dynamics of entanglement and 'attractor' states in the Tavis–Cummings model. *New J. Phys.*, **11**, 103047. 111

Jarvis, C., Rodrigues, D., Györffy, B., Spiller, T., Short, A. & Annett, J. (2010). Collapse and revival of "Schrödinger cat" states. *J. Opt. Soc. Am. B*, **27**, A164–A169. 111

Jarzyna, M. & Demkowicz-Dobrzański, R. (2012). Quantum interferometry with and without an external phase reference. *Phys. Rev. A*, **85**, 011801. 102

Jaynes, E.T. & Cummings, F.W. (1963). Comparison of quantum and semiclassical radiation theories with application to the beam maser. *Proc. IEEE*, **51**, 89–109. 73

Jin, X.M., Peng, C.Z., Deng, Y., Barbieri, M., Nunn, J. & Walmsley, I.A. (2013). Sequential path entanglement for quantum metrology. *Sci. Rep.*, **3**. 85

Jones, J.A., Karlen, S.D., Fitzsimons, J., Ardavan, A., Benjamin, S.C., Briggs, G.A.D. & Morton, J.J. (2009). Magnetic field sensing beyond the standard quantum limit using 10-spin NOON states. *Science*, **324**, 1166–1168. 51

Joo, J., Munro, W. & Spiller, T. (2011). Quantum metrology with entangled coherent states. *Phys. Rev. Lett.*, **107**, 83601. 52, 61, 66, 78, 87, 90, 102, 109

Joo, J., Park, K., Jeong, H., Munro, W.J., Nemoto, K. & Spiller, T.P. (2012). Quantum metrology for nonlinear phase shifts with entangled coherent states. *Phys. Rev. A*, **86**, 043828. 87

Kakuyanagi, K., Meno, T., Saito, S., Nakano, H., Semba, K., Takayanagi, H., Deppe, F. & Shnirman, A. (2007). Dephasing of a superconducting flux qubit. *Phys. Rev. Lett.*, **98**, 047004. 113

Kane, B.E. (1998). A silicon-based nuclear spin quantum computer. *Nature*, **393**, 133–137. 113

Knott, P., Sindt, J. & Dunningham, J. (2013). Detecting measurement-induced relative-position localization. *J. Phys. B*, **46**, 095501. 25, 26, 32, 38

Knott, P., Proctor, T., Nemoto, K., Dunningham, J. & Munro, W. (2014a). Effect of multimode entanglement on lossy optical quantum metrology. *Phys. Rev. A*, **90**, 033846. 86

Knott, P.A. & Dunningham, J.A. (2014). Precise phase measurements using an entangled coherent state. *arXiv preprint arXiv:1401.3969*. 63

Knott, P.A., Munro, W.J. & Dunningham, J.A. (2014b). Attaining sub-classical metrology in lossy systems with entangled coherent states. *Phys. Rev. A*, **89**, 053812. 63, 99, 109

Kok, P., Lee, H. & Dowling, J.P. (2002). Creation of large-photon-number path entanglement conditioned on photodetection. *Phys. Rev. A*, **65**, 052104. 85

Kołodyński, J. & Demkowicz-Dobrzański, R. (2013). Efficient tools for quantum metrology with uncorrelated noise. *New J. Phys.*, **15**, 073043. 16, 60, 86, 95, 97, 122

Laloë, F. (2012). *Do we really understand quantum mechanics?*. Cambridge University Press. 22

Lee, H., Kok, P. & Dowling, J.P. (2002). A quantum Rosetta Stone for interferometry. *J. Mod. Opt.*, **49**, 2325–2338. 49, 85, 87

Leghtas, Z., Kirchmair, G., Vlastakis, B., Devoret, M.H., Schoelkopf, R.J. & Mirrahimi, M. (2013). Deterministic protocol for mapping a qubit to coherent state superpositions in a cavity. *Phys. Rev. A*, **87**, 042315. 73, 98

Leonhardt, U. & Paul, H. (1993). Realistic optical homodyne measurements and quasiprobability distributions. *Physical Review A*, **48**, 4598. 66

Lund, A., Jeong, H., Ralph, T. & Kim, M. (2004). Conditional production of superpositions of coherent states with inefficient photon detection. *Phys. Rev. A*, **70**, 020101. 73

Marsili, F., Verma, V., Stern, J., Harrington, S., Lita, A., Gerrits, T., Vayshenker, I., Baek, B., Shaw, M., Mirin, R. *et al.* (2013). Detecting single infrared photons with 93% system efficiency. *Nature Photon.*, **7**, 210–214. 99

Matsuzaki, Y. (2010). *Robust measurement based quantum technology*. Ph.D. thesis, Oxford University. 113, 114, 115

Matsuzaki, Y., Benjamin, S.C. & Fitzsimons, J. (2011). Magnetic field sensing beyond the standard quantum limit under the effect of decoherence. *Phys. Rev. A*, **84**, 012103. 107, 113, 114, 115, 116, 118

Mazzola, L., Piilo, J. & Maniscalco, S. (2010). Sudden transition between classical and quantum decoherence. *Phys. Rev. Lett.*, **104**, 200401. 25

McGrayne, S.B. (2011). *The theory that would not die: how Bayes' rule cracked the enigma code, hunted down Russian submarines, & emerged triumphant from two centuries of controversy*. Yale University Press. 32

Michelson, A. & Morley, E. (1887). On the relative motion of earth and luminiferous ether. *American Journal of Science, Third Series*, **34**, 233–245. 13, 19, 20, 44, 45

Monz, T., Schindler, P., Barreiro, J.T., Chwalla, M., Nigg, D., Coish, W.A., Harlander, M., Hänsel, W., Hennrich, M. & Blatt, R. (2011). 14-qubit entanglement: Creation and coherence. *Phys. Rev. Lett.*, **106**, 130506. 108

Munro, W., Nemoto, K., Braunstein, S. & Milburn, G. (2001). Weak force detection with superposed coherent states. *Phys. Rev. A*, **66**, 023819. 85, 86, 109

Parigi, V., Zavatta, A., Kim, M. & Bellini, M. (2007). Probing quantum commutation rules by addition and subtraction of single photons to/from a light field. *Science*, **317**, 1890–1893. 64

Paris, M.G. (1996). Displacement operator by beam splitter. *Phys. Lett. A*, **217**, 78–80. 98, 102

Paris, M.G. (2009). Quantum estimation for quantum technology. *Int. J. Quantum Inf.*, **7**, 125–137. 57

Penzias, A.A. & Wilson, R.W. (1965). A measurement of excess antenna temperature at 4080 mc/s. *Astrophys. J.*, **142**, 419–421. 19

Pezze, L. & Smerzi, A. (2008). Mach-Zehnder interferometry at the Heisenberg limit with coherent and squeezed-vacuum light. *Phys. Rev. Lett.*, **100**, 073601. 32

Pototschnig, M., Chassagneux, Y., Hwang, J., Zumofen, G., Renn, A. & Sandoghdar, V. (2011). Controlling the phase of a light beam with a single molecule. *Phys. Rev. Lett.*, **107**, 063001. 23, 61, 97, 121

Punturo, M., Abernathy, M., Acernese, F., Allen, B., Andersson, N., Arun, K., Barone, F., Barr, B., Barsuglia, M., Beker, M. *et al.* (2010). The third generation of gravitational wave observatories and their science reach. *Class. Quantum Grav.*, **27**, 084007. 61

Purdy, T., Peterson, R. & Regal, C. (2013). Observation of radiation pressure shot noise on a macroscopic object. *Science*, **339**, 801–804. 61

Radcliffe, J. (1971). Some properties of coherent spin states. *J. Phys. A*, **4**, 313. 107, 109

Ralph, T. (2002). Coherent superposition states as quantum rulers. *Phys. Rev. A*, **65**, 42313. 85, 87, 109

Rau, A., Dunningham, J. & Burnett, K. (2003). Measurement-induced relative-position localization through entanglement. *Science*, **301**, 1081–1084. 25, 26, 29

Riedel, M.F., Böhi, P., Li, Y., Hänsch, T.W., Sinatra, A. & Treutlein, P. (2010). Atom-chip-based generation of entanglement for quantum metrology. *Nature*, **464**, 1170–1173. 85

Routledge, R. (2013). Bayes's theorem. *Encyclopedia Britannica*. 32

Rubin, M.A. & Kaushik, S. (2007). Loss-induced limits to phase measurement precision with maximally entangled states. *Phys. Rev. A*, **75**, 053805. 50

Sahota, J. & James, D.F. (2013). Quantum-enhanced phase estimation with an amplified Bell state. *Phys. Rev. A*, **88**, 063820. 54

Sahota, J. & Quesada, N. (2015). Quantum correlations in optical metrology: Heisenberg-limited phase estimation without mode entanglement. *Phys. Rev. A*, **91**, 013808. 121

Saito, S., Zhu, X., Amsüss, R., Matsuzaki, Y., Kakuyanagi, K., Shimo-Oka, T., Mizuochi, N., Nemoto, K., Munro, W.J. & Semba, K. (2013). Towards realizing a quantum memory for a superconducting qubit: Storage and retrieval of quantum states. *Phys. Rev. Lett.*, **111**, 107008. 109, 111

Sanders, B. (2012). Review of entangled coherent states. *J. Phys. A*, **45**, 244002. 52, 87

Sanders, B.C. (1992). Entangled coherent states. *Phys. Rev. A*, **45**, 6811. 52, 87

Schrödinger, E. (1980). Translation by J.D. Trimmer of "die gegenwärtige situation in der quantenmechanik" (1935). *P. Am. Philos. Soc.*, **124**, 323. 22

Tanaka, T., Knott, P., Matsuzaki, Y., Dooley, S., Yamaguchi, H., Munro, W.J. & Saito, S. (2014). Robust entanglement-based magnetic field sensor beyond the standard quantum limit. *arXiv preprint arXiv:1412.3887*. 108, 112, 113, 117

Tavis, M. & Cummings, F.W. (1968). Exact solution for an n–molecule-radiation–field Hamiltonian. *Phys. Rev.*, **170**, 379. 110

Taylor, M.A. & Bowen, W.P. (2014). Quantum metrology and its application in biology. *arXiv preprint arXiv:1409.0950*. 61

Taylor, M.A., Janousek, J., Daria, V., Knittel, J., Hage, B., Bachor, H.A. & Bowen, W.P. (2013). Biological measurement beyond the quantum limit. *Nature Photon.*, **7**, 229–233. 20, 23, 61, 97, 121

Tey, M.K., Chen, Z., Aljunid, S.A., Chng, B., Huber, F., Maslennikov, G. & Kurtsiefer, C. (2008). Strong interaction between light and a single trapped atom without the need for a cavity. *Nature Phys.*, **4**, 924–927. 23, 61, 97, 121

Tilma, T., Hamaji, S., Munro, W.J. & Nemoto, K. (2010). Entanglement is not a critical resource for quantum metrology. *Phys. Rev. A*, **81**, 022108. 85, 86, 87

Wiseman, H., Bartlett, S. & Vaccaro, J. (2004). Ferreting out the fluffy bunnies: Entanglement constrained by generalized super-selection rules. In *Laser Spectroscopy*, vol. 1, 307–314. 26

Wolfgramm, F. (2011). *Atomic Quantum Metrology with Narrowband Entangled and Squeezed States of Light*. Ph.D. thesis, Universitat Politècnica de Catalunya. 20

Wolfgramm, F., Vitelli, C., Beduini, F.A., Godbout, N. & Mitchell, M.W. (2013). Entanglement-enhanced probing of a delicate material system. *Nature Photon.*, **7**, 28–32. 23, 61, 97, 121

Zavatta, A., Parigi, V., Kim, M. & Bellini, M. (2008). Subtracting photons from arbitrary light fields: experimental test of coherent state invariance by single-photon annihilation. *New J. Phys.*, **10**, 123006. 64

Zhang, W.M., Gilmore, R. *et al.* (1990). Coherent states: theory and some applications. *Rev. Mod. Phys.*, **62**, 867. 107

Zhang, Y., Li, X., Yang, W. & Jin, G. (2013). Quantum fisher information of entangled coherent states in the presence of photon loss. *Phys. Rev. A*, **88**, 043832. 57, 78, 80, 91

Zhu, X., Saito, S., Kemp, A., Kakuyanagi, K., Karimoto, S.i., Nakano, H., Munro, W.J., Tokura, Y., Everitt, M.S., Nemoto, K. *et al.* (2011). Coherent coupling of a superconducting flux qubit to an electron spin ensemble in diamond. *Nature*, **478**, 221–224. 111

Zurek, W. (1991). Decoherence and the transition from quantum to classical. *Phys. Today*, 37. 25

Zurek, W. (2002). Decoherence and the transition from quantum to classical-revisited. *Los Alamos Science*, **27**, 86–109. 25